NAVAL POSTGRADUATE SCHOOL
Monterey, California

THESIS

COMPUTATIONAL ANALYSIS OF THE OFF-DESIGN PERFORMANCE OF A MACH 6 $\left[\left(\frac{L}{D}\right)I_{sp}\right]_{max}$ OPTIMIZED WAVERIDER

by

Ellen Coyne

September 1999

Co-Advisors: Conrad F. Newberry
Garth V. Hobson

Approved for public release; distribution is unlimited.

20000306 029

DTIC QUALITY INSPECTED 3

REPORT DOCUMENTATION PAGE

Form Approved
OMB No. 0704-0188

Public reporting burden for this collection of information is estimated to average 1 hour per response, including the time for reviewing instruction, searching existing data sources, gathering and maintaining the data needed, and completing and reviewing the collection of information. Send comments regarding this burden estimate or any other aspect of this collection of information, including suggestions for reducing this burden, to Washington headquarters Services, Directorate for Information Operations and Reports, 1215 Jefferson Davis Highway, Suite 1204, Arlington, VA 22202-4302, and to the Office of Management and Budget, Paperwork Reduction Project (0704-0188) Washington DC 20503.

1. AGENCY USE ONLY *(Leave blank)*	2. REPORT DATE **September 1999**	3. REPORT TYPE AND DATES COVERED **Master's Thesis**

4. TITLE AND SUBTITLE
Computational Analysis of the Off-Design Performance of a Mach 6 $\left[\left(\frac{L}{D}\right)I_{sp}\right]_{max}$ Optimized Waverider

5. FUNDING NUMBERS

6. AUTHOR(S)
Coyne, Ellen

7. PERFORMING ORGANIZATION NAME(S) AND ADDRESS(ES)
Naval Postgraduate School
Monterey, CA 93943-5000

8. PERFORMING ORGANIZATION REPORT NUMBER

9. SPONSORING / MONITORING AGENCY NAME(S) AND ADDRESS(ES)

10. SPONSORING/MONITORING AGENCY REPORT NUMBER

11. SUPPLEMENTARY NOTES
The views expressed in this thesis are those of the author and do not reflect the official policy or position of the department of defense or the u.s. government.

12a. DISTRIBUTION / AVAILABILITY STATEMENT
Approved for public release; distribution is unlimited.

12b. DISTRIBUTION CODE

ABSTRACT (Maximum 200 words)

13. In a continuation of ongoing Naval Postgraduate School efforts to study the performance characteristics of waverider-configured vehicles, a computational fluid dynamic (CFD) analysis of the Mach 6 $[L/D\ I_{sp}]_{max}$ optimized Price waverider was conducted. This analysis was performed to determine the theoretical force and moment data over a broad Mach number spectrum, and to compare theoretical and experimental results in the subsonic flight regime. The CFD determination of force and moment data represents a continuation of the ongoing analysis of the Price waverider configuration. Selected viscous and inviscid flow solutions for flight conditions in the range $0.3 \le M_\infty \le 6.0$, as well as a subsonic ($M_\infty = 0.3$) angle of attack sweep, were conducted using NASA CFD software (OVERFLOW1.8b). Examination of the computed converged flowfield solutions suggests that the surface pressure distributions and Mach number contours surrounding the body are valid. Low speed force and moment coefficient data are shown to exhibit reasonable agreement with the available subsonic wind tunnel data. Additionally, supersonic CFD results show the development of the expected shock layer, exhibiting an attached shock bed at the design Mach number ($M_\infty = 6.0$). Evaluation of the computed Mach number effects on lift and drag coefficients at subsonic, transonic and supersonic Mach numbers suggests that the Price waverider may exhibit some flight instabilities across the flight Mach number spectrum.

14. SUBJECT TERMS
Air vehicles, Hypersonic Flight, Computational Fluid Dynamics, Waverider Configurations

15. NUMBER OF PAGES
147

16. PRICE CODE

17. SECURITY CLASSIFICATION OF REPORT	18. SECURITY CLASSIFICATION OF THIS PAGE	19. SECURITY CLASSIFICATION OF ABSTRACT	20. LIMITATION OF ABSTRACT
Unclassified	**Unclassified**	**Unclassified**	UL

NSN 7540-01-280-5500

Standard Form 298 (Rev. 2-89)
Prescribed by ANSI Std 239-18

Approved for public release; distribution is unlimited

COMPUTATIONAL ANALYSIS OF THE OFF-DESIGN PERFORMANCE OF A MACH 6 $\left[\left(\frac{L}{D}\right)_{sp}\right]_{max}$ OPTIMIZED WAVERIDER

Ellen Coyne
Lieutenant Commander, United States Navy
B.S., United States Naval Academy, 1985

Submitted in partial fulfillment of the
requirements for the degree of

MASTER OF SCIENCE IN AERONAUTICAL ENGINEERING

from the

NAVAL POSTGRADUATE SCHOOL
September 1999

Author: _____
Ellen Coyne

Approved by: _____
Conrad F. Newberry, Co-Advisor

_____
Garth V. Hobson, Co-Advisor

_____
Gerald H. Lindsey, Chairman
Department of Aeronautics and Astronautics

ABSTRACT

In a continuation of ongoing Naval Postgraduate School efforts to study the performance characteristics of waverider-configured vehicles, a computational fluid dynamic (CFD) analysis of the Mach 6 $\left[\left(\frac{L}{D}\right)I_{sp}\right]_{max}$ optimized Price waverider was conducted. This analysis was performed to determine the theoretical force and moment data over a broad Mach number spectrum, and to compare theoretical and experimental results in the subsonic flight regime. The CFD determination of force and moment data represents a continuation of the ongoing analysis of the Price waverider configuration. Selected viscous and inviscid flow solutions for flight conditions in the range $0.3 \leq M_\infty \leq 6.0$, as well as a subsonic ($M_\infty = 0.3$) angle of attack sweep, were conducted using NASA CFD software (OVERFLOW1.8b). Examination of the computed converged flowfield solutions suggests that the surface pressure distributions and Mach number contours surrounding the body are valid. Low speed force and moment coefficient data are shown to exhibit reasonable agreement with the available subsonic wind tunnel data. Additionally, supersonic CFD results show the development of the expected shock layer, exhibiting an attached shock bed at the design Mach number ($M_\infty = 6.0$). Evaluation of the computed Mach number effects on lift and drag coefficients at subsonic, transonic and supersonic Mach numbers suggests that the Price waverider may exhibit some flight instabilities across the flight Mach number spectrum.

TABLE OF CONTENTS

I. INTRODUCTION 1

A. BACKGROUND 1
B. OBJECTIVE 2
C. PRICE WAVERIDER 3

II. DESCRIPTION OF CFD 5

A. GRIDGEN OVERVIEW 5
B. GRIDGEN3D OVERVIEW 5
C. GRIDED 6
D. OVERFLOW1.8B OVERVIEW 6
E. FAST 6

III. GRID GENERATION AND FILE INPUT 7

A. GRID GENERATION 7
B. SELECTED FLIGHT CONDITIONS 13
C. FLOW SOLUTION BATCH-FILE INPUT 15
1. Subsonic versus Supersonic Flowfields 15
2. Inviscid versus Viscous Flowfields 16
3. Engine Flow-Through Modeling 16

IV. RESULTS AND DISCUSSION 19

A. SUBSONIC RESULTS 19
1. Mach 0.3 Inviscid Results 19
2. Mach 0.3 Viscous Results 24
3. Subsonic Trends 28
B. SUPERSONIC RESULTS 28
1. Mach 6.0 Inviscid Results 29
2. Mach 6.0 Viscous Results 33
3. Supersonic Trends 35
C. ENGINE FLOW-THROUGH MODELING 36
D. REYNOLDS NUMBER EFFECTS 38
E. ALPHA SWEEP 45
F. CFD VALIDITY 49
G. CFD LIMITATIONS 50

V. CONCLUSIONS 51

A. GRID REFINEMENTS 52
B. OPPORTUNITIES FOR FURTHER TESTING 53

LIST OF REFERENCES 55

APPENDIX A. WAVERIDER SURFACE GRID POINTS 57

APPENDIX B. SAMPLE INPUT FILES 73

APPENDIX C. FLOW SOLUTIONS 83

INITIAL DISTRIBUTION LIST 131

LIST OF FIGURES

Figure 1. Waverider Grid Three-View and Oblique 9
Figure 2. Waverider Surface Grid Cusp 10
Figure 3. Three-Dimensional Computational Block 12
Figure 4. Number of Iterations vs. Mach Number 14
Figure 5. Engine Flow-Through Model Intake 17
Figure 6. Engine Flow-through Model Exhaust 17
Figure 7. Mach 0.3 (Inviscid) Residual Convergence History 20
Figure 8. Drag Coefficient vs. Number of Iterations for $M_\infty = 0.3$, Inviscid 21
Figure 9. Lift Coefficient vs. Number of Iterations for $M_\infty = 0.3$, Inviscid 22
Figure 10. Normalized Surface Pressure and Mach Number Contours, $M_\infty = 0.3$, Inviscid 23
Figure 11. Mach 0.3 (Viscous) Residual Convergence History 25
Figure 12. Drag Coefficient vs. Number of Iterations for $M_\infty = 0.3$, Viscous 26
Figure 13. Lift Coefficient vs. Number of Iterations for $M_\infty = 0.3$, Viscous 26
Figure 14. Normalized Surface Pressure and Mach Number Contours, $M_\infty = 0.3$, Viscous 27
Figure 15. Mach 6.0 (Inviscid) Residual Convergence History 30
Figure 16. Drag Coefficient vs. Number of Iterations for $M_\infty = 6.0$, Inviscid 31
Figure 17. Lift Coefficient vs. Number of Iterations for $M_\infty = 6.0$, Inviscid 31
Figure 18. Normalized Surface Pressure and Mach Number Contours, $M_\infty = 6.0$, Inviscid 32
Figure 19. Mach 6.0 (Viscous) Residual Convergence History 33
Figure 20. Drag Coefficient vs. Number of Iterations for $M_\infty = 6.0$, Viscous 34
Figure 21. Lift Coefficient vs. Number of Iterations for $M_\infty = 6.0$, Viscous 34
Figure 22. Normalized Surface Pressure and Mach Number Contours, $M_\infty = 6.0$, Viscous 35
Figure 23. Mach 6.0 (Inviscid) Engine Flow-Through Convergence History 37
Figure 24. Normalized Surface Pressure and Mach Number Contours, $M_\infty = 6.0$, Engine Flow-Through, Inviscid 38
Figure 25. Lift Coefficient vs. Mach Number 41
Figure 26. Drag Coefficient vs. Mach Number 42
Figure 27. Lift-to-Drag Ratio vs. Mach Number 43
Figure 28. Pitching Moment Coefficient vs. Mach Number 45
Figure 29. Lift Coefficient vs. Angle of Attack 46
Figure 30. Drag Coefficient vs. Angle of Attack 47
Figure 31. Lift-to-Drag Ratio vs. Angle of Attack 48
Figure 32. Normalized Surface Pressure and Mach Contours, Mach 0.3 at 10° AOA 49
Figure C-1. Mach 0.3 Inviscid Convergence History 83
Figure C-2. Mach 0.3 Viscous Convergence History 83
Figure C-3. Mach 0.4 Inviscid Convergence History 84
Figure C-4. Mach 0.4 Viscous Convergence History 84
Figure C-5. Mach 0.5 Inviscid Convergence History 85

Figure C-6. Mach 0.5 Viscous Convergence History 85
Figure C-7. Mach 0.6 Inviscid Convergence History 86
Figure C-8. Mach 0.6 Viscous Convergence History 86
Figure C-9. Mach 0.7 Inviscid Convergence History 87
Figure C-10. Mach 0.7 Viscous Convergence History 87
Figure C-11. Mach 0.8 Inviscid Convergence History 88
Figure C-12. Mach 0.8 Viscous Convergence History 88
Figure C-13. Mach 0.9 Inviscid Convergence History 89
Figure C-14. Mach 0.9 Viscous Convergence History 89
Figure C-15. Mach 1.2 Inviscid Convergence History 90
Figure C-16. Mach 1.2 Viscous Convergence History 90
Figure C-17. Mach 2.0 Inviscid Convergence History 91
Figure C-18. Mach 2.0 Viscous Convergence History 91
Figure C-19. Mach 4.0 Inviscid Convergence History 92
Figure C-20. Mach 4.0 Viscous Convergence History 92
Figure C-21. Mach 6.0 Inviscid Convergence History 93
Figure C-22. Mach 6.0 Viscous Convergence History 93
Figure C-23. Mach 6.0 Inviscid Engine Flow-Through Convergence History 94
Figure C-24. Force Coefficients vs. Iterations Mach 0.3 Inviscid 95
Figure C-25. Force Coefficients vs. Iterations Mach 0.3 Viscous 96
Figure C-26. Force Coefficients vs. Iterations Mach 0.4 Inviscid 97
Figure C-27. Force Coefficients vs. Iterations Mach 0.4 Viscous 98
Figure C-28. Force Coefficients vs. Iterations Mach 0.5 Inviscid 99
Figure C-29. Force Coefficients vs. Iterations Mach 0.5 Viscous 100
Figure C-30. Force Coefficients vs. Iterations Mach 0.6 Inviscid 101
Figure C-31. Force Coefficients vs. Iterations Mach 0.6 Viscous 102
Figure C-32. Force Coefficients vs. Iterations Mach 0.7 Inviscid 103
Figure C-33. Force Coefficients vs. Iterations Mach 0.7 Viscous 104
Figure C-34. Force Coefficients vs. Iterations Mach 0.8 Inviscid 105
Figure C-35. Force Coefficients vs. Iterations Mach 0.8 Viscous 106
Figure C-36. Force Coefficients vs. Iterations Mach 0.9 Inviscid 107
Figure C-37. Force Coefficients vs. Iterations Mach 0.9 Viscous 108
Figure C-38. Force Coefficients vs. Iterations Mach 1.2 Inviscid 109
Figure C-39. Force Coefficients vs. Iterations Mach 1.2 Viscous 110
Figure C-40. Force Coefficients vs. Iterations Mach 2.0 Inviscid 111
Figure C-41. Force Coefficients vs. Iterations mach 2.0 Viscous 112
Figure C-42. Force Coefficients vs. Iterations Mach 4.0 Inviscid 113
Figure C-43. Force Coefficients vs. Iterations Mach 4.0 Viscous 114
Figure C-44. Force Coefficients vs. Iterations Mach 6.0 Inviscid 115
Figure C-45. Force Coefficients vs. Iterations Mach 6.0 Viscous 116
Figure C-46. Force Coefficients vs. Iterations Mach 6.0 Engine Flow-Through 117
Figure C-47. Mach 0.3 Inviscid Normalized Surface Pressure and Mach Contours 118
Figure C-48. Mach 0.3 Viscous Normalized Surface Pressure and Mach Contours 118
Figure C-49. Mach 0.4 Inviscid Normalized Surface Pressure and Mach Contours 119
Figure C-50. Mach 0.4 Viscous Normalized Surface Pressure and Mach Contours 119

Figure C-51. Mach 0.5 Inviscid Normalized Surface Pressure and Mach Contours..... 120
Figure C-52. Mach 0.5 Viscous Normalized Surface Pressure and Mach Contours..... 120
Figure C-53. Mach 0.6 Inviscid Normalized Surface Pressure and Mach Contours..... 121
Figure C-54. Mach 0.6 Viscous Normalized Surface Pressure and Mach Contours..... 121
Figure C-55. Mach 0.7 Inviscid Normalized Surface Pressure and Mach Contours..... 122
Figure C-56. Mach 0.7 Viscous Normalized Surface Pressure and Mach Contours..... 122
Figure C-57. Mach 0.8 Inviscid Normalized Surface Pressure and Mach Contours..... 123
Figure C-58. Mach 0.8 Viscous Normalized Surface Pressure and Mach Contours..... 123
Figure C-59. Mach 0.9 Inviscid Normalized Surface Pressure and Mach Contours..... 124
Figure C-60. Mach 0.9 Viscous Normalized Surface Pressure and Mach Contours..... 124
Figure C-61. Mach 1.2 Inviscid Normalized Pressure and Mach Contours..... 125
Figure C-62. Mach 1.2 Viscous Normalized Surface Pressure and Mach Contours..... 125
Figure C-63. Mach 2.0 Inviscid Normalized Surface Pressure and Mach Contours..... 126
Figure C-64. Mach 2.0 Viscous Normalized Surface Pressure and Mach Contours..... 126
Figure C-65. Mach 4.0 Inviscid Normalized Surface Pressure and Mach Contours..... 127
Figure C-66. Mach 4.0 Viscous Normalized Surface Pressure and Mach Contours..... 127
Figure C-67. Mach 6.0 Inviscid Normalized Surface Pressure and Mach Contours..... 128
Figure C-69. Mach 6.0 Engine Flow-Through Normalized Surface Pressure and Mach Contours..... 129

LIST OF TABLES

Table 1. Summary of Flight Conditions Analyzed 13
Table 2. Summary of Inviscid Solution Force Coefficients 39
Table 3. Summary of Viscous Solution Force Coefficients 39

I. INTRODUCTION

A. BACKGROUND

In 1959, Nonweiler hypothesized that the pressure generated behind a planar shock wave might be sufficient to provide the vehicle lift. His proposal of a caret-shaped vehicle was the first of a class of vehicles designed for supersonic flight. The principle of lift generated by the pressure rise through a shock wave lead to the term "waverider". The decades that followed Nonweiler's hypothesis have brought a series of improvements and refinements. The latest group of proposed vehicles is a selection of conical flow waveriders, designed to capture and ride upon conical shaped shocks. A number of studies on the optimization of waverider-configured vehicles are ongoing [Refs. 1 and 2].

The Naval Postgraduate School (NPS) is pursuing in an ongoing conceptual development of hypersonic, carrier-based waverider–configured aircraft. Since 1992 both individual thesis students and design team efforts have contributed to the body of knowledge in this emerging field of aerodynamics [Ref. 3]. Included within this study is the development and investigation of a proposed carrier-based interceptor aircraft, and among the proposed designs is the Price waverider.

Using the NASA Ames Research Center (ARC) Waverider Code, David Price developed a conceptual configuration for a hypersonic, carrier-based, deck-launched, waverider strike aircraft, optimized for Mach=6, $\left[\left(\frac{L}{D}\right)I_{sp}\right]_{max}$, flight [Ref. 4]. The waverider code is a subset of the Hypersonic Aircraft Vehicle Optimization Code (HAVOC), created by the Systems Analysis Branch at NASA ARC. Optimization of the product of L/D and the specific impulse produced an integrated engine and air vehicle. This method is in concert with one of the fundamental design aspects of hypersonic vehicles. The first and most important aspect is to create and capture a conical shock. A second important aspect, however, capitalizes on shock compression, forward of the engine intake. This shock pre-compresses the engine inlet air. Aft body shaping is used

to expand the exhaust in an external nozzle. Thus engine air compression and expansion takes place external to the engine modules themselves allowing for a reduction in weight, complexity and cooling requirements. In this sense the engine and aircraft configuration must be an integrated effort, both being interdependent in all aspects of flow analysis – hence the need to optimize this type of vehicle using both aerodynamic parameters (L/D) and engine parameters (I_{sp}).

Follow-on work to Price's initial development are ongoing. Based on this configuration, 15-inch and 8-inch root chord aluminum models were produced by NASA Ames for NPS research to facilitate the further characterization of the performance of the Price waverider. Using the smaller aluminum model, Lowell M. Johnson performed a series of flow visualization tests of the Price waverider in the NPS water tunnel [Ref. 5]. Subsonic wind tunnel testing of the Price waverider has been performed by Mark E. Cedrun [Ref. 6] and Michael Huff [Ref. 7], using the larger of the aluminum models. Tests to date indicate that flight is feasible for waverider-configured aircraft. The Price waverider database, while including water and wind tunnel data, lacks a Computational Fluid Dynamic (CFD) component. Additionally, no supersonic or hypersonic data were available for the Price waverider prior to this CFD analysis.

The primary thrust of this thesis was the development of the appropriate surface grid for the Price waverider and the calculation of aerodynamic characteristics in subsonic and supersonic flight. The subsonic CFD flow solutions were aimed at complimenting existing wind tunnel and water tunnel data. CFD results are compared with the force and moment data obtained in recent wind tunnel tests for a range of Reynolds numbers and angles of attack. The range of subsonic, transonic and supersonic solutions represents a continuation of the ongoing research effort supporting the complete performance analysis of the Price waverider.

B. OBJECTIVE

The objectives of this thesis are to determine the theoretical force and moment data over a broad Mach number spectrum, and to compare theoretical and experimental results in the subsonic flight regime. The results, across the whole flight spectrum of

Mach numbers, are to serve as a basis for continued examination and feasibility analysis of the Price waverider.

C. PRICE WAVERIDER

The Price waverider was optimized for Mach 6.0 flight using inviscid, conical shock, optimization methods contained in the Ames Research Center Waverider Code. The parabolic leading edge droops from the nose to the trailing edge. While the upper surface remains entirely in line with the freestream, the lower surface slopes to create a wedged-body over which the shocks are formed. Along the centerline, a pair of ramps precedes the engine inlet. Off the centerline the lower surface creates a 5.2 degree semi-vertex angle. Along the aft-body the lower surface is faired upward to meet the trailing edge. Waveriders derived from strictly conical flow will have a flat base at the trailing edge, creating enormous base drag, thus the lower surface must be faired to narrow the trailing edge to decrease the base drag or pressure drag of the vehicle [Ref. 8]. The fairing of the aft body under-surface up to the trailing edge creates a negative camber in the body. This negative camber is more pronounced on the centerline, where the engine cowling ramps back up to the trailing edge.

THIS PAGE INTENTIONALLY LEFT BLANK

II. DESCRIPTION OF CFD

Computational Fluid Dynamic methods were developed as a means of solving the complex system of partial differential equations that describe a given flowfield. The use of computers to solve discretized equations enables the solution to be found for those partial differential equations for which no exact solution exists. Since 1975, numerous advancements have been made to refine the application of several finite element methods for computing flowfields; improving algorithms to improve computational efficiency and further defining and extending the regimes in which CFD methods can be applied with confidence [Ref. 3].

The application of CFD techniques to a known geometry is a multi-step process. Several software applications are used for grid generation and refinement, and flow solution and analysis. NPS has a suite of computer software that enables grid generation and manipulation, flow solving and graphic presentation of the solution.

A. GRIDGEN OVERVIEW

GRIDGEN Version 9 is a Computer Science Corporation developed software tool, which was originally sponsored for development by the U. S. Air Force. It is an interactive code used to create 2-, or 3-dimensional grids. The domains can be represented graphically within GRIDGEN or exported as data files for additional operations, such as providing the computational space for flow solutions. GRIDGEN requires the import of surface points from a previous design effort or the creation of surfaces manually within the bounds of the program [Ref. 9].

B. GRIDGEN3D OVERVIEW

GRIDGEN3D is a batch code used in conjunction with GRIDGEN Version 9. This code is used to refine the grid volume by adjusting grid points internal to the block of points. In using of GRIDGEN3D, caution should be applied to ensure that the body

points are fixed to prevent the blending of body features by designating body surface as fixed boundaries.

C. GRIDED

GRIDED is an interactive, menu-driven file FORTRAN-based software application used to manipulate the grid. GRIDED allows the addition and removal of grid points or planes, the selection of indices and the performance of coordinate transforms.

D. OVERFLOW1.8B OVERVIEW

OVERFLOW1.8b is a flow solution code developed by NASA Ames Research Center and is a combination of the older F3D and Chimera codes. It uses an implicit, finite-differencing scheme to solve the Reynolds-Averaged Navier-Stokes equations in strong conservative form [Ref. 10]. The input file from the user enables the selection of:

- Flight regime or flow conditions, such as Mach number, angle of attack, yaw angle, ratio of specific heats, viscosity and freestream temperature.
- Turbulence model selection (Options include Baldwin-Lomax, Baldwin-Barth, k-ϖ and k-ε models)
- Computational controls such as time step, differencing scheme, artificial viscosity selection and smoothing parameters.
- Boundary conditions (options include viscous or inviscid walls, inflow or outflow, or flow-through cuts).

OVERFLOW1.8b solutions are run on the Cray Y-MP J94 computer, owned and operated by the Naval Postgraduate School.

E. FAST

Flow Analysis Software Toolkit (FAST) was used to compute and graphically represent the grid and its corresponding flow solution. The images of the waverider body and the Mach number and pressure profiles contained within Chapter IV are products of FAST. [Ref. 11]

III. GRID GENERATION AND FILE INPUT

Development of an appropriate grid and the correspondingly appropriate boundary conditions and flowfield constraints was essential to the production of realistic solutions for the waverider flowfield. Additionally, a number of options exist within OVERFLOW1.8b, the flow solver, for refining the techniques used to optimize the computational efficiency or to enhance certain flow characteristics.

A. GRID GENERATION

Grid generation was accomplished using the previously described code, GRIDGEN. Using grid points, provided by NASA Ames (originally generated by David Price), the surface geometry of the Price Waverider was defined by importing the series of upper-surface and lower-surface fuselage station grid points into GRIDGEN. The surface domains were then built up by manually inserting the coordinates in GRIDGEN to create sequential fuselage station connectors. Once both the upper and lower surface of the waverider was completely defined by the series of linked fuselage station domains, these domains were consolidated into a single-domain covering the upper and lower surfaces. Following the initial creation of the waverider's surface grid, a number of anomalies were observed in GRIDGEN in the basic geometry of the grid, so minor adjustments to the database provided by NASA were made.

Those changes included a coordinate transformation, elimination of co-incident or nearly co-incident fuselage stations and minor body modifications to match model geometry. The fuselage station coordinates that were provided by NASA Ames created a body whose axis lay in the z-direction. Since OVERFLOW1.8b specified M_∞ in the x-direction, a coordinate transformation was performed to a right-handed coordinate system with the axis of the body lying on the x-axis. After an examination to ensure there was no loss of geometric features on the waverider surface, fuselage stations at x = 0.03014, 0.03024, 0.03034, 0.33192, 0.63181 and 0.65947, were eliminated due to their positions, nearly coincident to adjacent stations. Additionally, the grid point defining the outermost point of the fuselage station at x = 0.93164 appeared to be missing, creating a sawtooth in

the leading edge. A new end point was created for this fuselage station to bring the points at that station out to create a smooth leading edge, rather than the sawtooth observed in GRIDGEN. The new point was created by interpolating between the outer points of adjacent fuselage stations. Lastly, the engine exhaust in the wind tunnel model was a ramped exhaust, whereas the points provided by NASA Ames modeled the exhaust as a flat plate. To match the geometry of the wind tunnel model and to match a more realistic full-scale configuration, the fuselage station at $x = 0.93816$ was eliminated in its entirety. The resulting engine exhaust ramp geometry then mimicked the model. The surface grid points, with the required adjustments, are provided in Appendix A.

The spanwise grid dimension (grid dimensions refer to the number of points in the grid in a given direction) of the waverider surface was set at 20 grid points each for the upper and lower surfaces. After some experimentation, 20 grid points in the span was seen as the minimum number of points required to model the surface geometry clearly. Additional points would increase the size of the grid and the grid density, slowing computations. Clustering points at the outer edge of the body's upper surface was done to provide sufficient grid point density near the sharp leading edge. The body's lower surface required grid point clustering at both the leading edge and at the engine cowling in order to ensure adequate modeling of the body geometry. The chordwise dimension of the grid was 32 points from nose to tail, after the removal of the fuselage stations noted above. Additional gridlines were added to provide higher grid density at the trailing edge of the engine cowling and at the trailing edge of the vehicle.

After numerous attempts to eliminate negative cell volumes at the trailing edge, a cusp was added at the trailing edge to ease grid geometry. This addition extended the blunt trailing edge a distance of 1.5 percent of the root chord length. This cusp is the only modification made that changed the computational grid shape from the model shape. Creation of a sharply-cusped trailing edge was believed to be more representative of final vehicle shape, as this addition helped to alleviate the high base-pressure drag forces caused by the bluntness of the Price waverider trailing edge. The final dimension of the grid was 45 points from nose to tail. Overall length of the vehicle, as prescribed by the

grid points provided by NASA Ames, was equal to 1.0, prior the addition of the cusped trailing edge. Dimensions, when quoted as a fraction of the body length, are a fraction of the original body length or root chord, vice a fraction of the computational model length or root chord.

The resulting surface grid is shown in Figures 1 and 2. The inset of Figure 1 shows the addition of the trailing edge cusp, increasing the total model length by 1.5 percent.

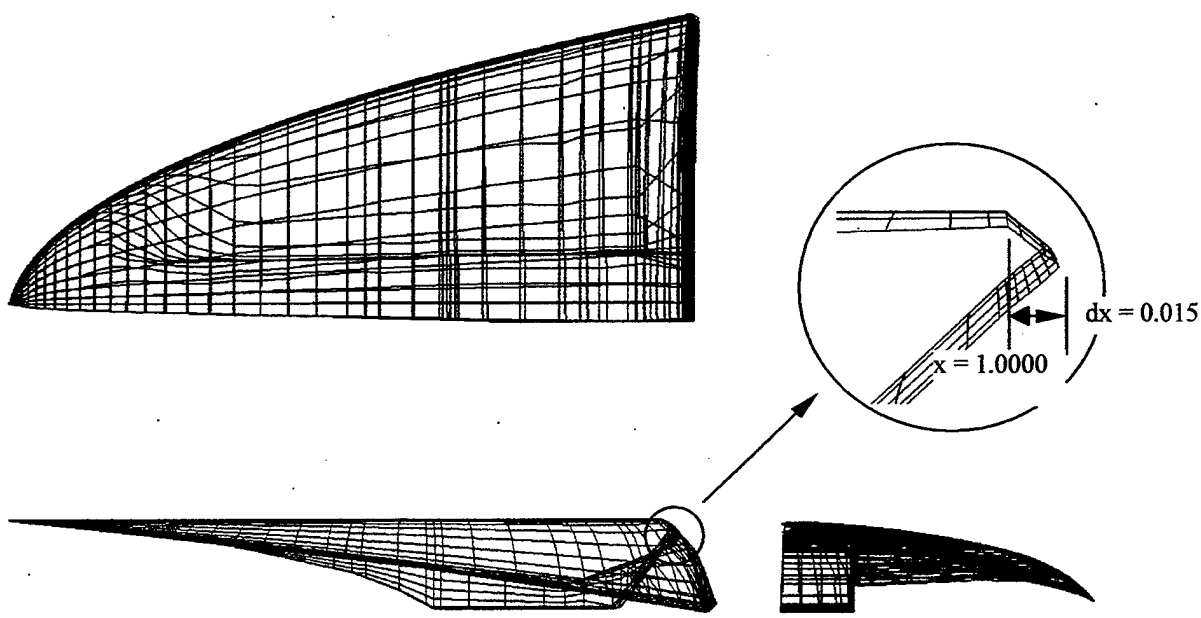

Figure 1. Waverider Grid Three-View and Oblique

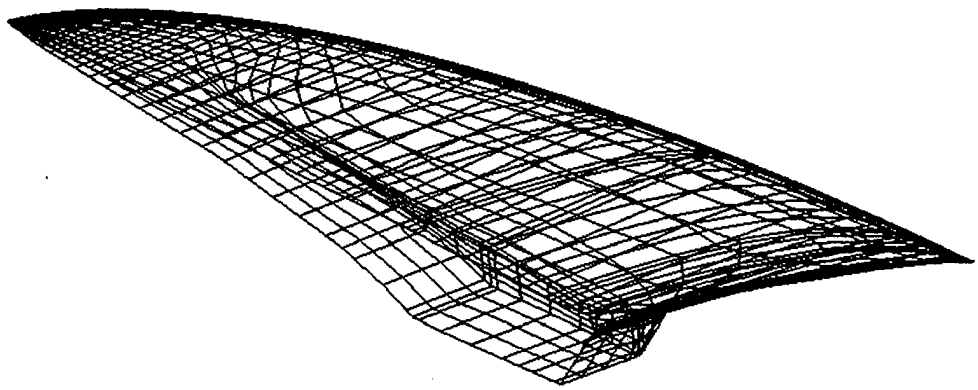

Figure 2. Waverider Surface Grid Cusp

In addition to the complex geometry of the lower surface and the sharp curvature of the trailing edge cusp, the droop of the leading edge of the wing contributed to the difficulty in creating a single three-dimensional block that was suitable for use by OVERFLOW1.8b. The vehicle configuration required a multi-step approach to creating a suitable 3-dimensional computational block surrounding the waverider half-body. First, it was necessary to split the vehicle's upper and lower surfaces and map out the surrounding airspace in two separate blocks to prevent gridlines from crossing from the lower surface to the upper surface. Then the two blocks had to be merged to create the entire computational space. This was done by creating the surrounding surfaces including domains with the following number of grid points:

Sting:	20x50
Wake Cut:	20x50
Cut Plane:	45x50
Outer Upper Shell:	20x45
Outer Lower Shell:	20x45
Upper Back Plane:	45x50
Lower Back Plane:	45x50

Of those domains, the sting, the wake, and the plane that was created to divide the upper and lower surface grids were included, identically, in both the upper and lower blocks to be joined as identical elements. It should be noted that, in this application, the

sting is the representation of the line forward of the waverider nose, created as an entity of the computational space. It does not refer to the sting used in wind tunnel tests to mount the vehicle in the tunnel test section. From these domains, along with the upper and lower surfaces of the body, the six-domain upper and lower 3D volumetric grids, known as blocks, were created. Inspection of each of the blocks using GRIDGEN3D, was used to determine the presence of negative cell volumes. Negative cell volumes resulted when the grid lines within the grid volume had tangled and the indices of the grid lines in certain areas were no longer sequential. The implication of this is that Δx or Δy used by the finite differencing scheme in OVERFLOW1.8b will be a negative number, which is unacceptable to the code.

The GRIDGEN3D elliptic solver, with a LaPlacian foreground control function, was used to resolve the negative cell volumes in both the upper and lower blocks. The LaPlacian function tended to drive the cells within the 3D block to equal volume cells throughout the total computational volume, thus those cells with negative volumes were driven to match the average cell volume, which was positive. While equal volume was unlikely to be achieved in a 3D grid containing a sharp body, applying this control eliminated the crossing of gridlines. It was possible to allow the elliptic solver to run for too many iterations. If this was done the number of negative cell volumes tended to increase. Periodically the elliptic solver was stopped, and the grid was examined to ensure the number of cells with negative volume were continuing to decrease. Regardless of the care taken not to over manipulate the grid, the elliptic solver tended to increase the distance between the body and its adjacent grid points at all points except the plane of symmetry, where grid points were held as fixed entities.

FAST images of the upper and lower 3D blocks, following the elimination of the negative cell volumes, were examined to identify coordinate discrepancies. It was necessary to reverse the direction of the J-planes (the surfaces radiating from the body to the outer shell in lengthwise planes) and K-planes (surface planes stepping out from the body surface to the outer shell) of the upper block. This was accomplished using the GRIDED option to reverse plane indices. Following coordination of the plane indices of

the upper and lower blocks, the two blocks were joined, again using GRIDED. Additionally, one J-plane was added to the upper and lower back planes of the block to provide the planes of symmetry that facilitated the use of a central-differencing scheme in the computational phase of this analysis. This single block was then saved and examined, once again, for negative cell volumes using GRIDGEN3D.

The figure below provides a perspective view of the 3-D computational block. At the center of this block is the surface of the waverider, seen as the black body. Final dimensions of the computational block were 41x45x50 grid points, for a total of 94,250 points.

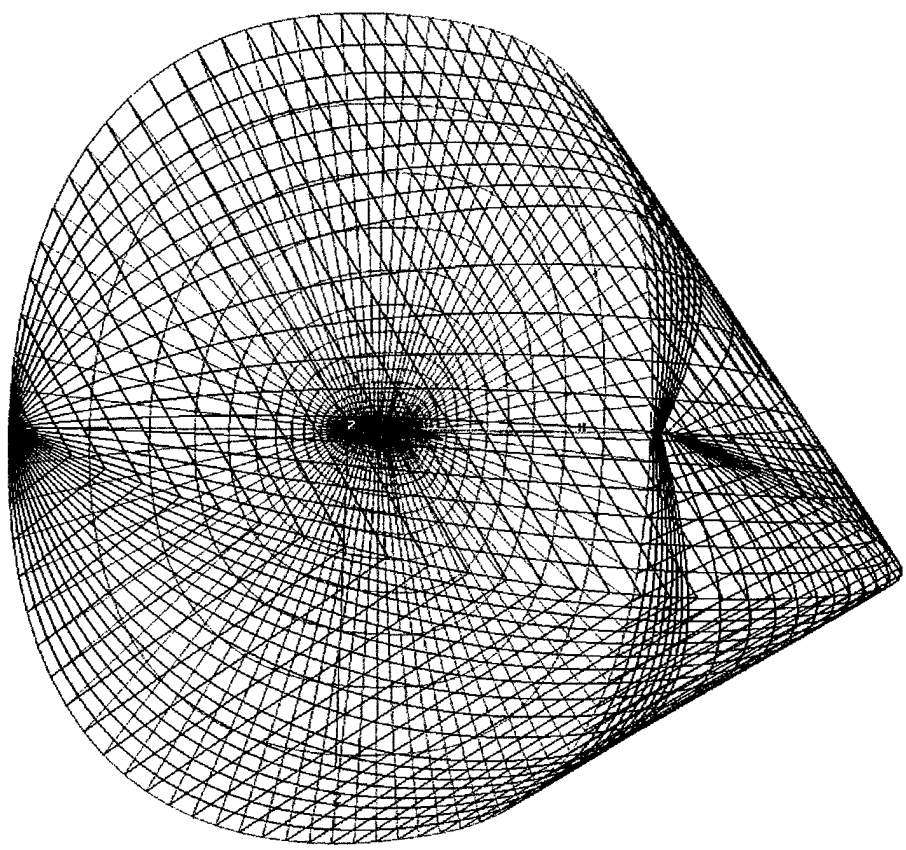

Figure 3. Three-Dimensional Computational Block

Coordinate directions used by OVERFLOW1.8b were specified to have the J-direction increasing along the length of the body from nose to tail. The K-direction was specified as positive around the body, from the upper centerline, out to the wing tip, and back into the centerline of the lower surface. The L-direction is positive in the direction radiating out from the body to the shell of the 3D grid.

B. SELECTED FLIGHT CONDITIONS

To support the study of Reynolds number effects for both viscous and inviscid flow conditions, a range ($0.3 \leq M_\infty \leq 6.0$) of computations were conducted. A summary of the flight conditions for which analysis was performed is provided in Table 1.

Mach Number Range		**Angle of Attack Sweep**	**Engine Flow-Through**
0° AOA		$M_\infty = 0.3$	0° AOA
Inviscid	Viscous	Viscous	Inviscid
0.3	0.3	(degrees AOA)	$M_\infty = 6.0$
0.4	0.4		
0.5	0.5	-10	
0.6	0.6	-8	
0.7	0.7	-4	
0.8	0.8	-2	
0.9	0.9	0	
1.2	1.2	6	
2.0	2.0	2	
4.0	4.0	8	
6.0	6.0	10	

Table 1. Summary of Flight Conditions Analyzed

Both viscous and inviscid flow solutions for the Price waverider were run for M_∞ = 0.3, 0.4, 0.5, 0.6, 0.7, 0.8, 0.9, 1.2, 2.0, 4.0, and 6.0. Alpha sweeps were conducted at $M_\infty = 0.3$. Additionally, the $M_\infty = 6.0$ input file was modified to include boundary conditions simulating engine intake and exhaust features to examine the effect of engine flow-through at design conditions. OVERFLOW1.8b is optimized for $M_\infty = 5.0$ flow

solutions. While the code performed well over a broad range of Mach numbers, the time required to compute low speed solutions and the decreasing stability of the code at Mach numbers greater than $M_\infty = 5.0$ began to limit its application.

Figure 4 shows the number of iterations required to achieve convergence in the flow solutions at each Mach number. At the lower Mach number, and indeed even at $M_\infty = 0.3$, the computational time required to fully converge a solution is over 130,000 iterations. This equated to over 50 hours of computational time, using all four processors of the Cray supercomputer. The Mach 0.5 solution required nearly 160,000 iterations due to the smaller time step that was required to keep the solution stable. The reason for the instability seen at $M_\infty = 0.5$ was not clear. At $M_\infty = 6.0$, the time step required to prevent the solution from becoming unstable was very small and the computational solution was particularly intolerant of even moderately aggressive attempts to speed up the convergence.

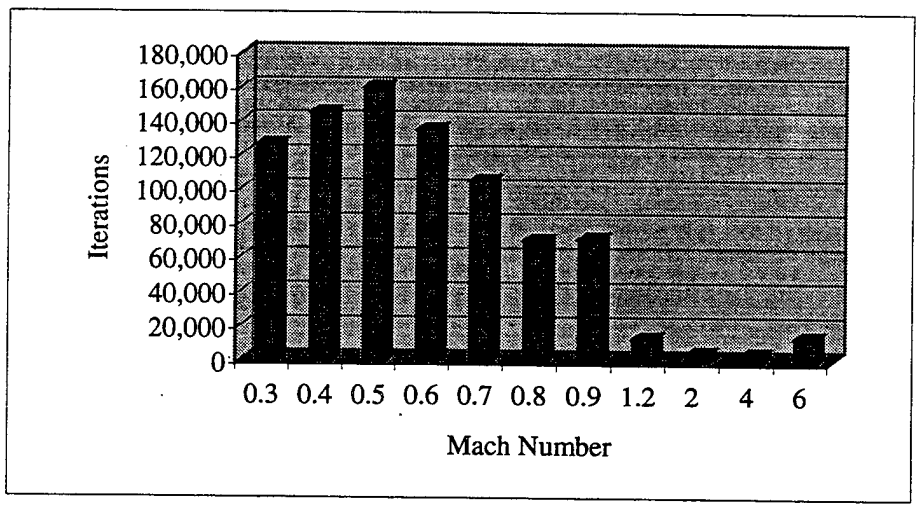

Figure 4. Number of Iterations vs. Mach Number

C. FLOW SOLUTION BATCH-FILE INPUT

OVERFLOW1.8b is a batch-run FORTRAN-based flow solver, which required the creation of input files to start each flow solution. Input files for each flight regime were created, using Reference 8, to reflect the flow conditions, desired turbulence model, computational controls and boundary conditions. Each of the batch input files was set up to apply a central-differencing scheme on a single grid computational space. Mach number and Reynolds number inputs reflected the desired freestream Mach number and the Reynolds number computed for the 15-inch model at sea-level conditions. Boundary conditions at the upper and lower back planes of the 3D grid were defined as planes of symmetry in the Y-direction. The wake cut was intended to be invisible to the flow and was defined as a fold-over cut flow-through plane. The outer shell was defined as a supersonic and/or subsonic inflow/outflow surface.

Throughout the course of computations the input files were updated to reflect more aggressive time steps, allowable after a solution began to converge. The time steps were adjusted without regard to real-time. Sample input batch-files are provided in Appendix B.

A summary of the general approaches used is given below.

1. Subsonic versus Supersonic Flowfields

In general, the allowable time steps for the finite difference calculations were a function of the freestream Mach number and maturity (i. e., how far the solution had converged) of the solution. Once the solution began to converge time steps could be increased, usually by factors of two until convergence. Allowable time steps were greatly reduced at $M_\infty = 6.0$ because of the velocity of the flow. The time step here had to be reduced by an order of magnitude, to dt = 0.001, to meet stability requirements. Tannehill, Anderson and Pletcher provide an excellent discussion of stability requirements and Courant-Friedrich-Levy (CFL) numbers [Ref. 12] .

Transonic and supersonic flow solutions required the use of second-order smoothing in all three directions to accommodate discontinuities in the flowfield across

shocks. Shock discontinuities became present in the flowfield at freestream Mach numbers of $M_\infty = 0.7$ and higher. Prior to that Mach number, no special considerations in the input files were required.

2. Inviscid versus Viscous Flowfields

The input files for Euler (inviscid) solutions required fewer arguments as the flow description defined no viscosity effects in any direction nor was any turbulence model specified. Conversely the input batch-files for the viscous cases specified viscosity effects in the J- (around the waverider body) and L-directions (from the waverider body to the outer shell). Viscosity in the K direction (along the length of the waverider body) was neglected in order to reduce the computational time. Neglecting these streamwise viscous terms resulted in the solution of a parabolized form of the Navier-Stokes equations, which was computationally more efficient. The Baldwin-Lomax turbulence model was selected for use in all viscous cases.

3. Engine Flow-Through Modeling

Input batch-files for the engine flow-through for required additional boundary conditions that described the intake area as a region of extrapolated outflow (i. e., the flow approaching the intake was allowed to exit the computational domain through that region, shown in Figure 5). This figure shows the flow approaching the engine inlet from the right and penetrating the area of the inlet, seen as arrows inside the engine duct.

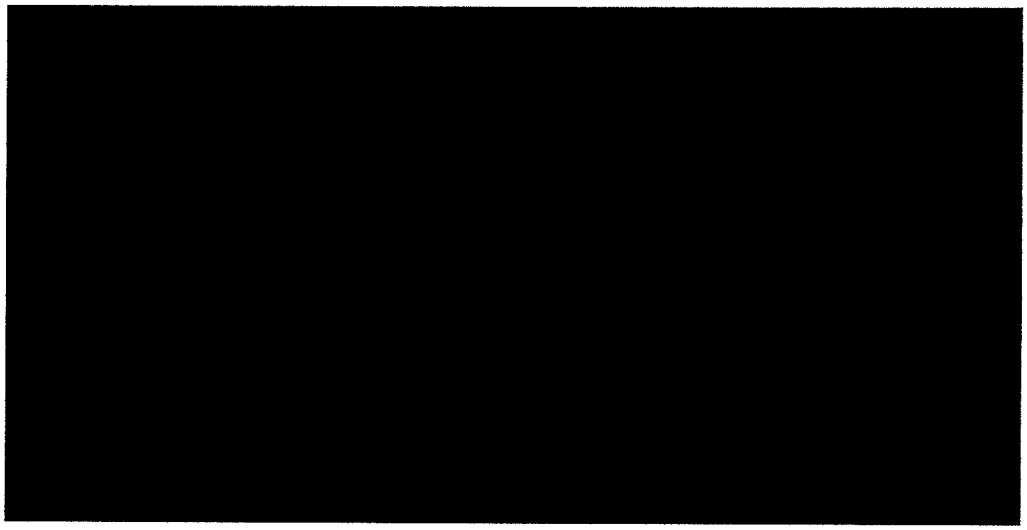

Figure 5. Engine Flow-Through Model Intake

The engine exhaust are was defined as nozzle inflow (i. e., the mass flow, extrapolated from p_0 and T_0, was injected into the computational domain at the exhaust plane). Engine exhaust flow was defined as freestream flow, shown in Figure 6. Here we see both the results of the external flow solution as green arrows and the superimposed engine flow-through exhaust, seen as the arrows in the freestream direction.

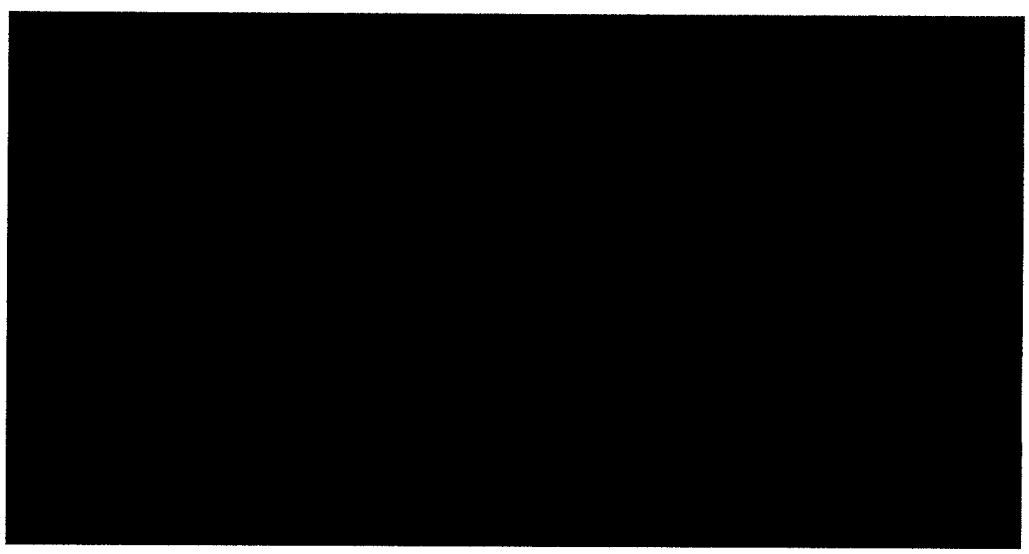

Figure 6. Engine Flow-through Model Exhaust

THIS PAGE INTENTIONALLY LEFT BLANK

IV. RESULTS AND DISCUSSION

A. SUBSONIC RESULTS

Integral to the validation of computational solutions is the attainment of "steady-state" or convergence. As the boundary conditions propagate through the computational space, values at a given point are compared to the values of the previous iteration until the residual difference becomes negligible. In this study, a drop in residual values of three orders of magnitude was considered a converged solution. A sample convergence history is provided in Figure 7.

To validate each of the flow solutions reported in this study, each flight condition solution was examined for convergence of the solution's residuals, convergence of the lift and drag coefficients to a steady state, and representative surface pressure distribution and Mach number distribution within the flowfield surrounding the vehicle.

1. Mach 0.3 Inviscid Results

The significant computational time required to conduct low subsonic computational analysis limited low-subsonic solutions to a minimum Mach number of $M_\infty = 0.3$. Wind tunnel tests provided data up to a maximum Mach number of $M_\infty = 0.15$. While the computational analysis provided here is not entirely coincidental with existing wind tunnel data, the solution obtained demonstrated fair representation of the low speed flow characteristics of the Price waverider.

Examining the $M_\infty = 0.3$ inviscid solution, shown in Figure 7, shows that the convergence history achieved just over three orders of magnitude convergence in 126,200 iterations. The short period oscillations were the result of periodic vortex formation and subsequent shedding at the trailing edge of the vehicle. Also present in the convergence history was a long period oscillation occurring approximately once every thousand iterations. This was speculated to be the result of acoustic waves reverberating within the computational space. While no direct evidence within the solution of the flowfield

supported that conclusion, their presence in the subsonic solutions only supported the conclusions that an acoustic phenomena of some type had occurred.

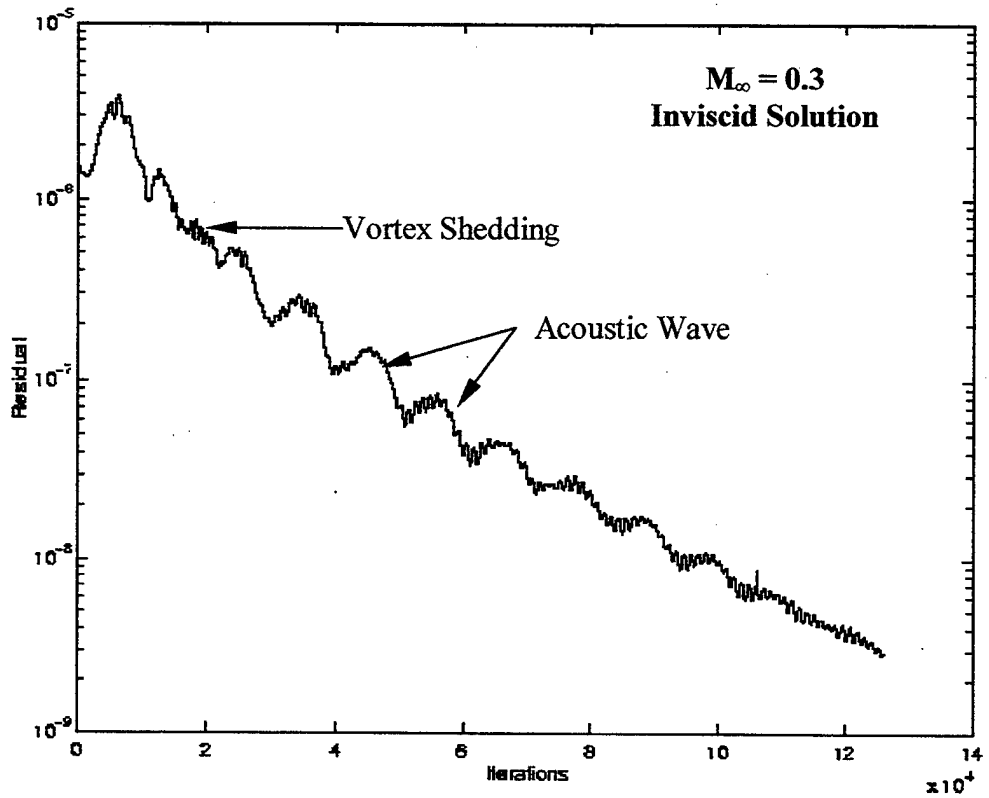

Figure 7. Mach 0.3 (Inviscid) Residual Convergence History

Figure 8 shows the drag coefficient history. Note that the drag coefficient also converged to a steady state as the solution converged. The final achieved drag coefficient was computed was $C_D = 0.0194$.

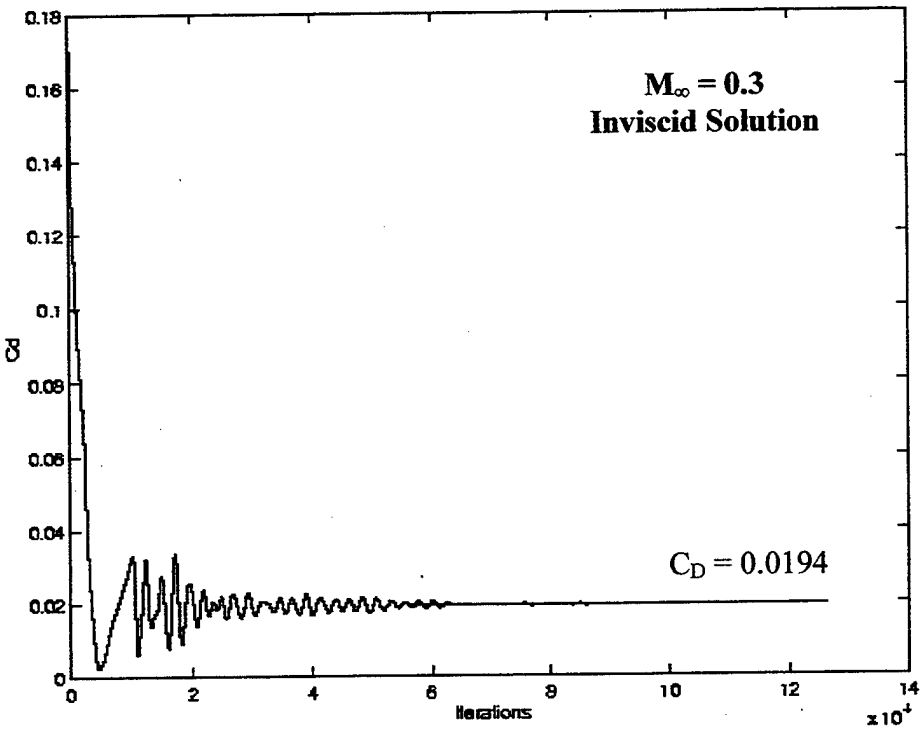

Figure 8. Drag Coefficient vs. Number of Iterations for $M_\infty = 0.3$, Inviscid

Figure 9 shows the lift coefficient history. This force coefficient converged to a stable value coincident with the drop in residuals. At $M_\infty = 0.3$, the lift coefficient converged to $C_L = -0.0310$. The presence of a negative lift coefficient at subsonic speeds was the result of the body geometry that produced lift at supersonic speeds. While the wedge angle of the vehicle forebody created a mean chord line that was a straight line at a positive angle of attack, the nozzle expansion aft of the engine cowl and the shape of the lower wing surface created a negative camber in the vehicle, giving rise to negative lift at zero degrees angle of attack.

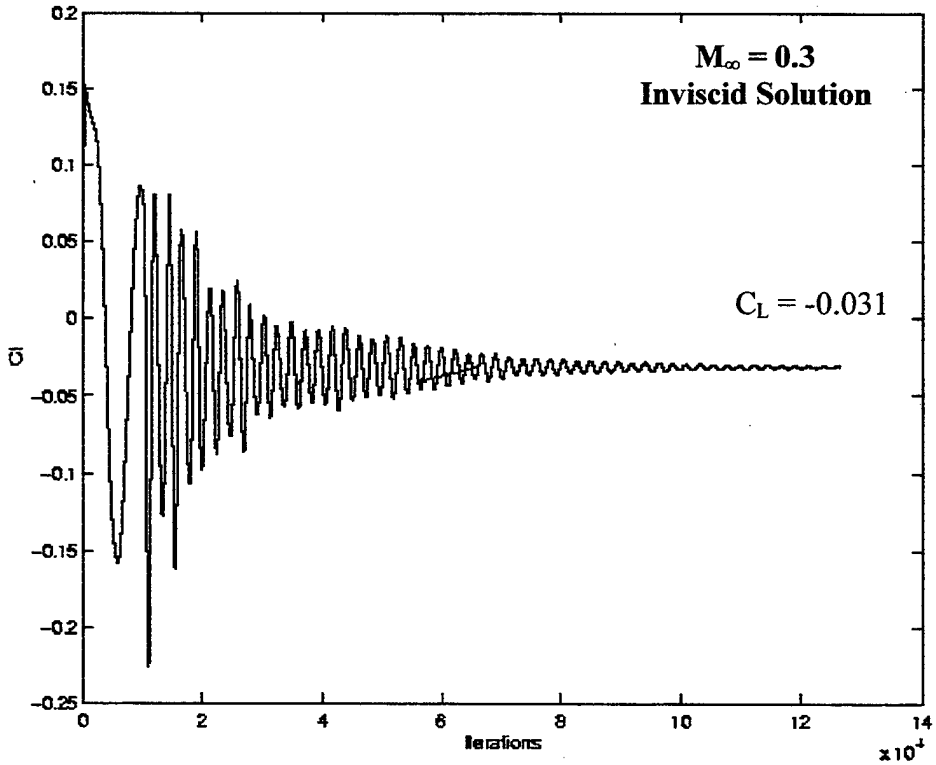

Figure 9. Lift Coefficient vs. Number of Iterations for $M_\infty = 0.3$, Inviscid

Using FAST images, the flowfield solution was graphically examined. Figure 10 shows the distribution of the normalized pressure (pressure is normalized to the freestream static pressure) on the body surface and the Mach number contours normal to the body in the surrounding flowfield. The normalized pressure was equal to the freestream pressure over the entire upper surface. In the inviscid case, the upper surface flow was unperturbed, as the waverider upper surface was aligned with the freestream. The lower surface pressure distribution illustrated a slightly higher pressure area on the lower surface of the vehicle forebody than on the lower aftbody, indicating a potential for significant pitch-up in the vehicle at low speeds. This was borne out by the computed pitching moment coefficient of $C_M = -0.033$. Neither region displayed a pressure distribution that was capable of providing lift, as was confirmed by the negative lift coefficient.

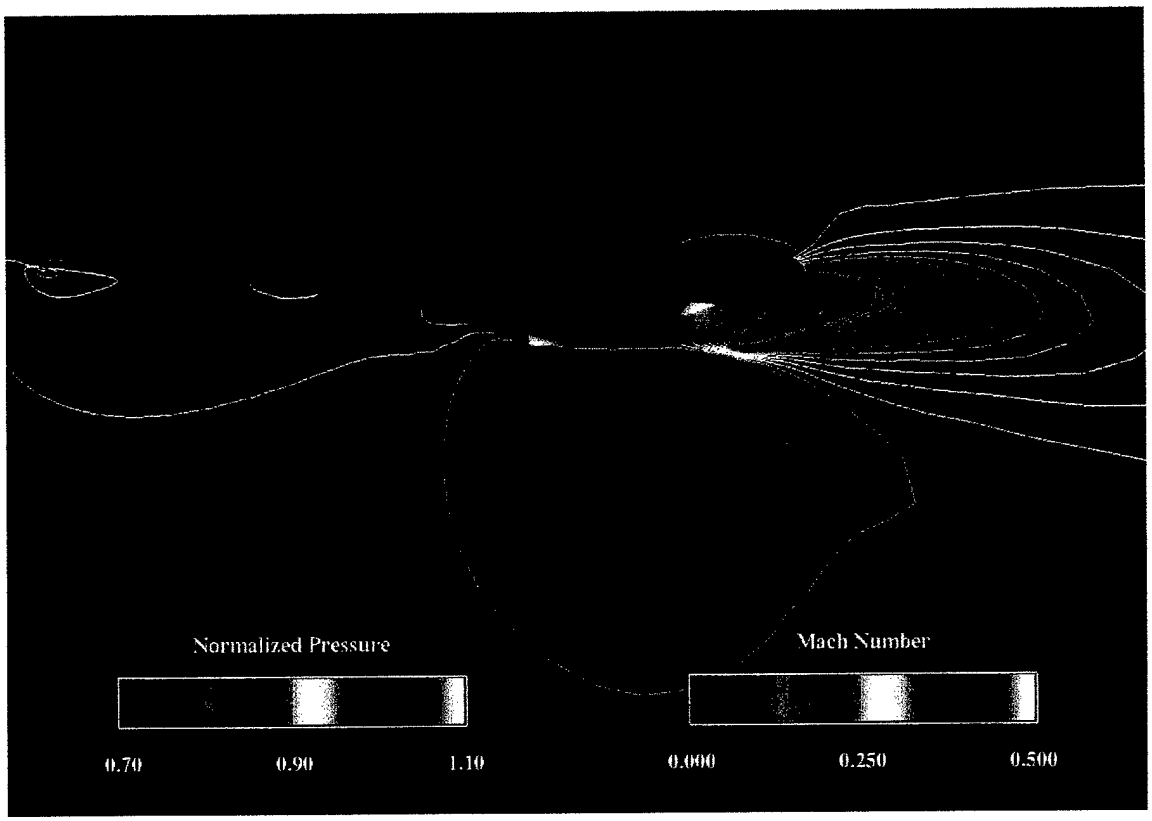

Figure 10. Normalized Surface Pressure and Mach Number Contours, $M_\infty = 0.3$, Inviscid

The Mach number contours confirmed the nearly unperturbed upper surface, which contrasted with the large Mach number gradients at the trailing edge and the less extreme but critical, Mach number contours along the lower surface. The Mach number contours at the nose of the vehicle indicated that the stagnation point was located on the lower surface of the body slightly aft of the nose of the vehicle. Contours along the lower surface outlined the flow compression at the beginning of the first and second engine inlet ramps and subsequent expansion as the flow turned back toward the freestream at the engine cowl and upward again at the engine nozzle. Further away from the body, grid spacing was less dense, which resulted in the Mach contour lines not being represented as smooth curves. This lack of smooth contour lines, indicated a grid dependency within the solution.

2. Mach 0.3 Viscous Results

Viscous terms were added to the partially converged inviscid solution at 66,200 iterations in order to capitalize on the convergence already achieved during the inviscid computation. OVERFLOW1.8b allowed the viscous modification to previously inviscid solutions. This addition had several notable impacts. Shown in Figure 11, residuals rose sharply as the flow was "virtually" perturbed by the addition of viscosity, spiking at well over the initial maximum, but recovering within 1000 iterations. As is seen in Figure 11, short period oscillations remained present, as the more physically representative wake in the viscous model continued to generate and shed vortices. The sonic wave reverberation persisted as well. It should be noted that the addition of viscous terms enabled a slightly more aggressive time step to be used in the remaining computations.

It was hoped that the addition of these viscous terms would serve to stabilize the solution and gain faster convergence, while it can be seen that the opposite result was achieved. Despite the more aggressive time step and expectations of a more rapid convergence, the slope of the declining residuals when compared with the inviscid case appeared to be the same.

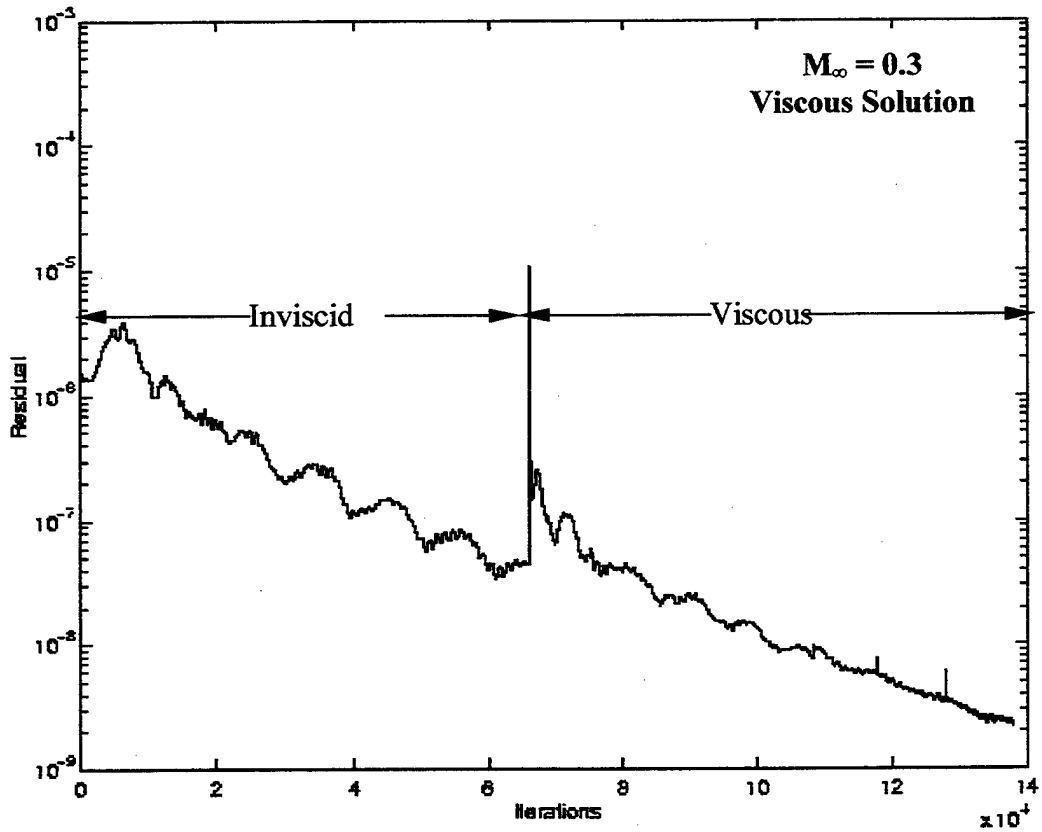

Figure 11. Mach 0.3 (Viscous) Residual Convergence History

Figures 12 and 13 illustrate the impact of the introduction of viscous terms on both the lift coefficient and the drag coefficient. The computation of a more physically realistic wake, enhanced the vehicle performance in both axes. A small, but notable, drop in drag occurred with the addition of viscosity, which demonstrated that the addition of viscous drag over the body was more than compensated by the significant reduction in pressure drag achieved as the viscous terms forestalled the onset of separation at the trailing edge. Similarly, the drag coefficient, which continued to oscillate, shifted upwards to a new mean lift coefficient at the introduction of the viscous terms.

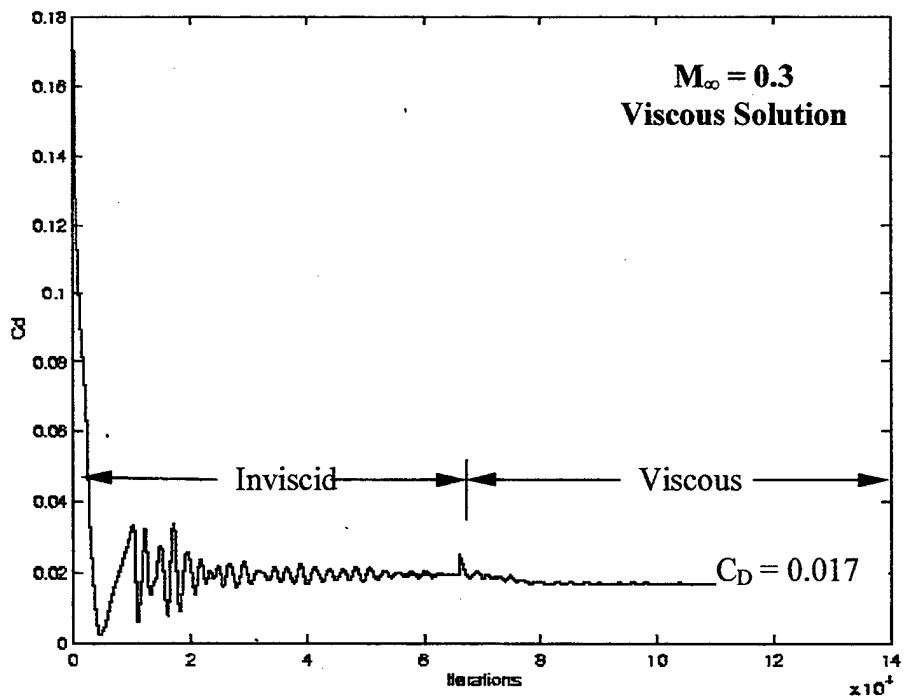

Figure 12. Drag Coefficient vs. Number of Iterations for $M_\infty = 0.3$, Viscous

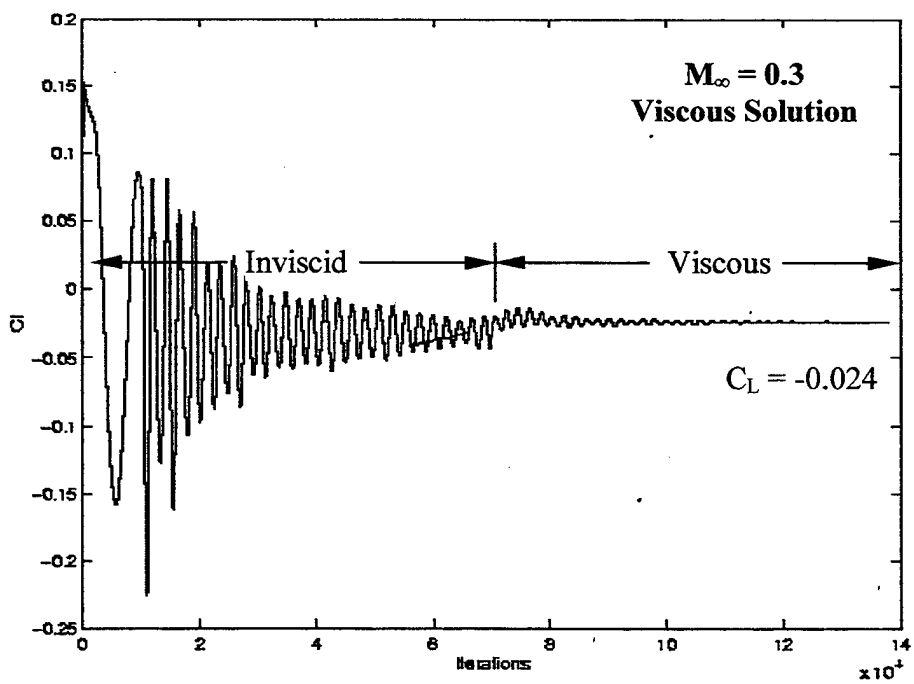

Figure 13. Lift Coefficient vs. Number of Iterations for $M_\infty = 0.3$, Viscous

The graphical representation of the surface pressure and Mach number contours in the viscous case at $M_\infty = 0.3$ are shown in Figure 14. The presence of Mach number variation in the flowfield over the upper surface was an indication of the boundary layer development and propagation into the flowfield. The lower surface boundary layer was visible along the engine cowl. The region of the trailing edge showed a narrower wake that was believed to be more representative of the expected physical wake, due to the presence of viscosity in the flow. The computed viscous wake (Figure 14) was smaller and better defined than the wake in the inviscid case (Figure 10), which indicated less separated flow in the region of the trailing.

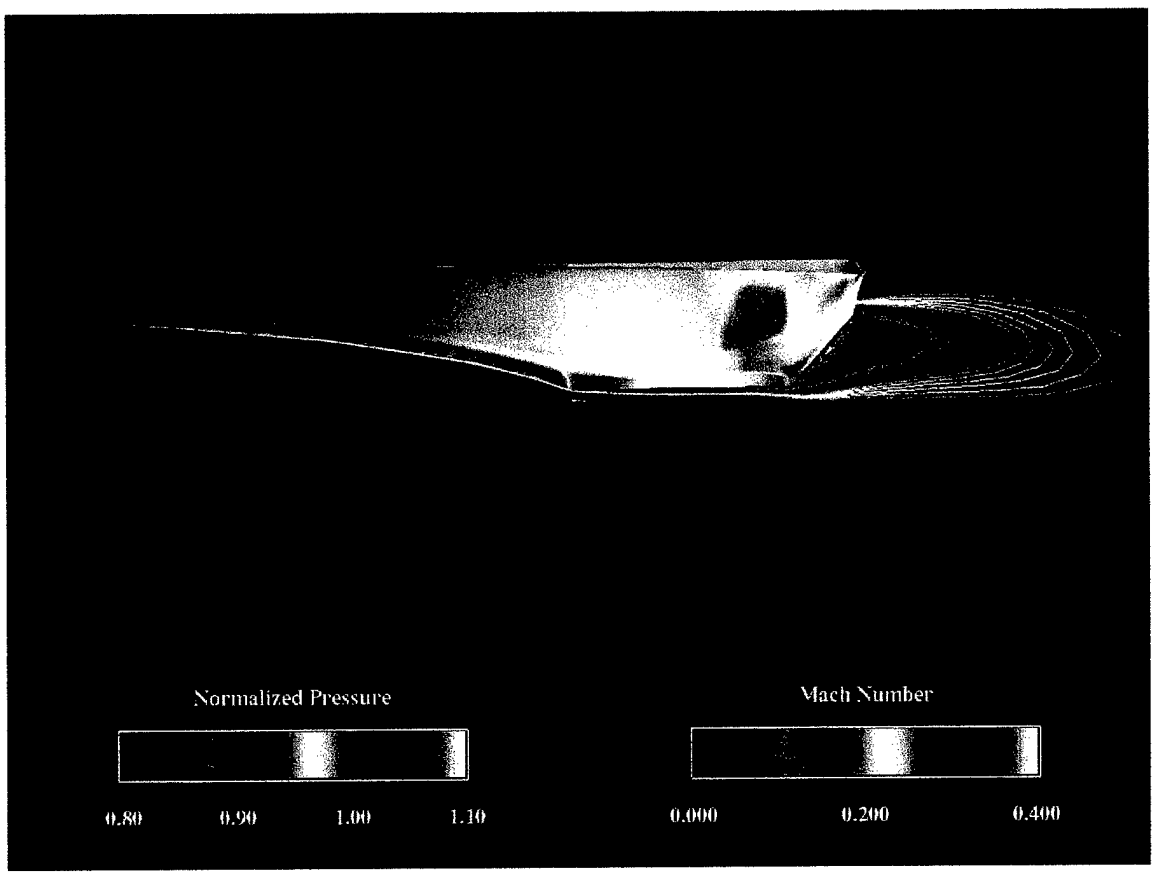

Figure 14. Normalized Surface Pressure and Mach Number Contours, $M_\infty = 0.3$, Viscous

3. Subsonic Trends

The convergence histories, force coefficient histories and FAST images for all solutions can be seen in Appendix C. Flow solutions for the remainder of the subsonic flight conditions demonstrated many similar characteristics. Residual plots demonstrated the requisite convergence to a steady state solution. The addition of viscous forces after a number of inviscid iterations caused a spike to appear in the residual files similar to the spike seen in Figure 11. Beginning at $M_\infty = 0.5$, the presence of the long-period acoustic resonance dampens out in the early iterations leaving only the shot period vortex-shedding oscillation evident within the residual plot. An additional undamped oscillation occurred in the nearly converged viscous solutions at $M_\infty = 0.7$ (See Figure C-10) , 0.8 and 0.9. Visual inspection of the solutions of these flight conditions using FAST showed the separation and recirculation of flow in the wake of the vehicle. This separation was believed to be the cause of the unsteadiness in the residual.

With increasing Mach number the stagnation point, evidenced by the Mach contours seen at the nose, migrated forward from a position aft of the nose to a position coincidence with the nose of the waverider (See Figure C-47 to Figure C-60).

Lift and drag coefficient histories showed very little difference in patterns across the subsonic Mach number spectrum; each file showed oscillating values which damped to a single value as the solution converged. Behaviors of the lift and drag coefficients, with the addition of viscous terms, were similar to the case of $M_\infty = 0.3$ viscous flow. Trends in the values of these coefficients are the subject of the later section on Reynolds number effect.

B. SUPERSONIC RESULTS

The supersonic solutions had the advantage of requiring significantly less computational time to obtain a fully converged solution. The $M_\infty = 4.0$ solution converged in 4,100 iterations, as opposed to the 160,000 iterations required for $M_\infty = 0.5$. In addition to the speed at which the codes ran, a number of other differences between the subsonic and supersonic solutions exists.

1. Mach 6.0 Inviscid Results

Figure 13 shows the convergence history for the inviscid $M_\infty = 6.0$ solution. This solution required some 13,000 iterations due to the small time step required to prevent the solution from going unstable. Nonetheless, the computational time was an order of magnitude lower than the subsonic solutions. Note that both the long-period oscillations, attributed to acoustic wave reverberation within the computational space, and the short period oscillations, attributed to trailing edge vortex shedding, seen in Figures 7 and 11, were absent in the $M_\infty = 6.0$ convergence history.

The shape of the convergence history, when compared to the subsonic results (Figures 7 and 11) , was markedly different. The residuals failed to drop off at the nearly steady rate seen in the subsonic convergence histories, but, instead, maintained a nearly constant value until late in the computation and finally dropped off sharply. The reason for the convergence history remaining nearly constant and then suddenly dropping off was that, within the flowfield of the waverider at supersonic conditions, the bulk of the flowfield was largely unaffected, thus the residuals did not converge until the effected sections were fully updated. Once the solution began to update the region close to the body, the solution converged rapidly.

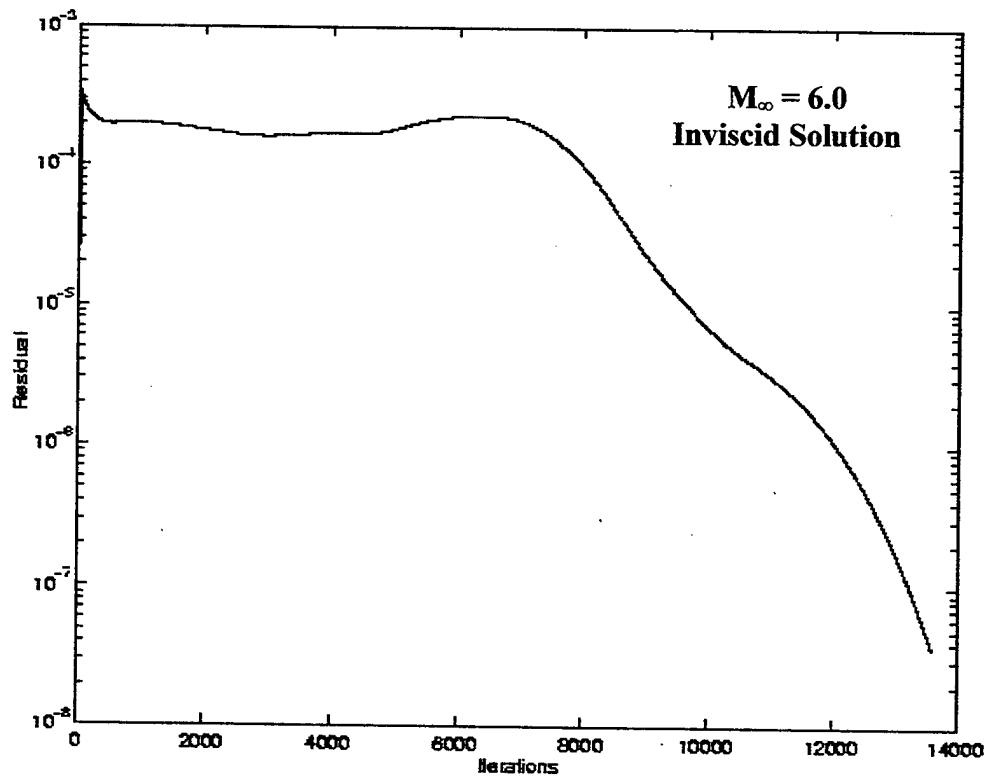

Figure 15. Mach 6.0 (Inviscid) Residual Convergence History

Despite the lack of a fully converged solution early in the computation the drag (Figure 16) and lift (Figure 17) coefficients rose quickly and remained nearly steady throughout the computation. Also noteworthy was the drop in the drag coefficient by half, to $C_D = 0.00439$ from the $M_\infty = 0.3$ inviscid solution of $C_D = 0.0194$. As expected, the lift coefficient at $M_\infty = 6.0$ is positive. At Mach 6.0, the converged lift coefficient was $C_L = 0.018$.

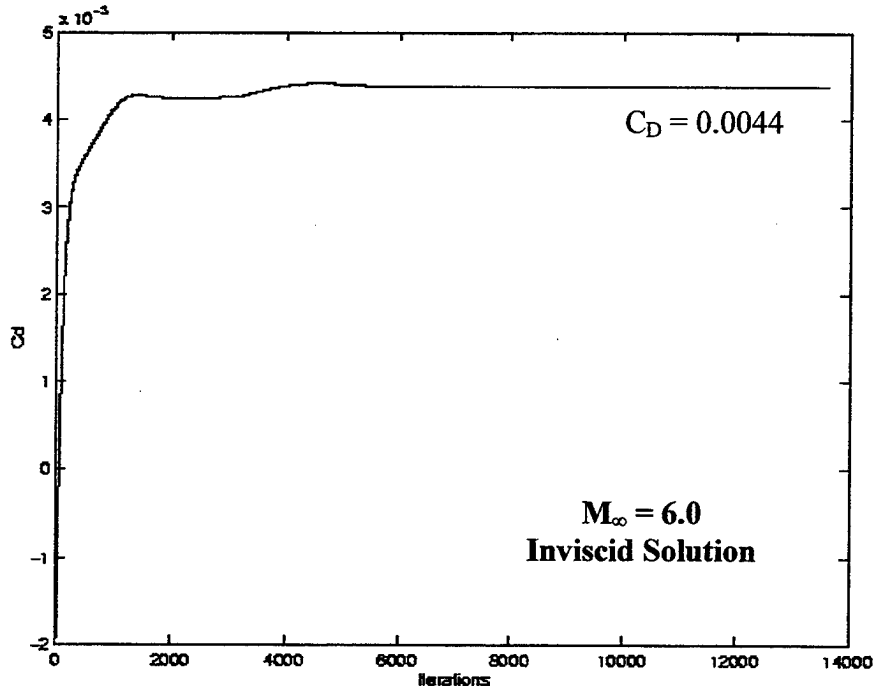

Figure 16. Drag Coefficient vs. Number of Iterations for $M_\infty = 6.0$, Inviscid

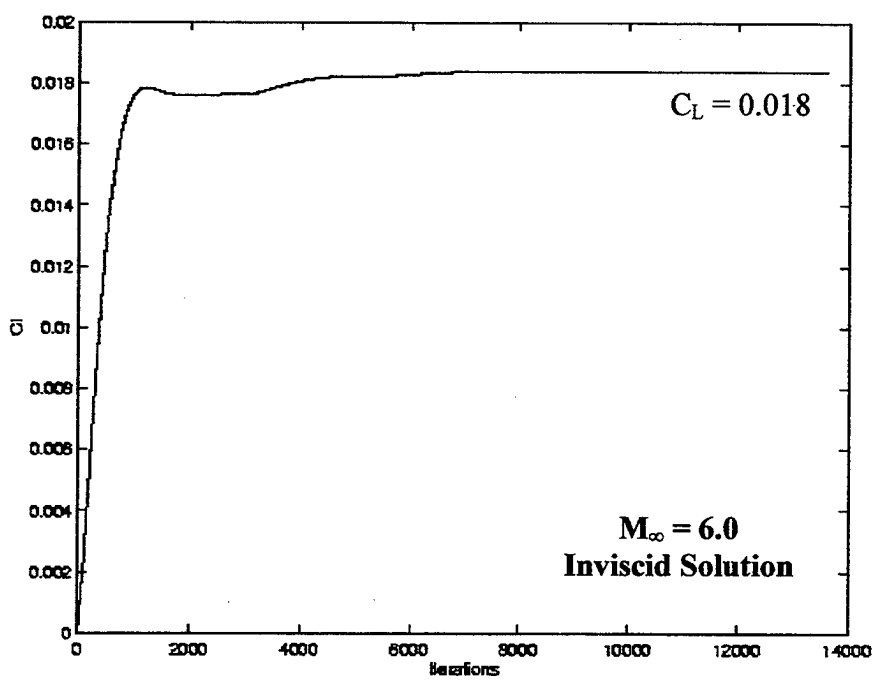

Figure 17. Lift Coefficient vs. Number of Iterations for $M_\infty = 6.0$, Inviscid

Figure 18 shows the normalized pressure on the surface of the waverider as well as the computed Mach number contours in the flowfield surrounding the body. The pressure differential between the fore and aft bodies of the vehicle appeared less pronounced than at $M_\infty = 0.3$, however the scale of the legend was changed to accommodate the large pressure rise at the engine intake. Pressures of nearly 14 times the freestream static pressures were seen in this region of the flow.

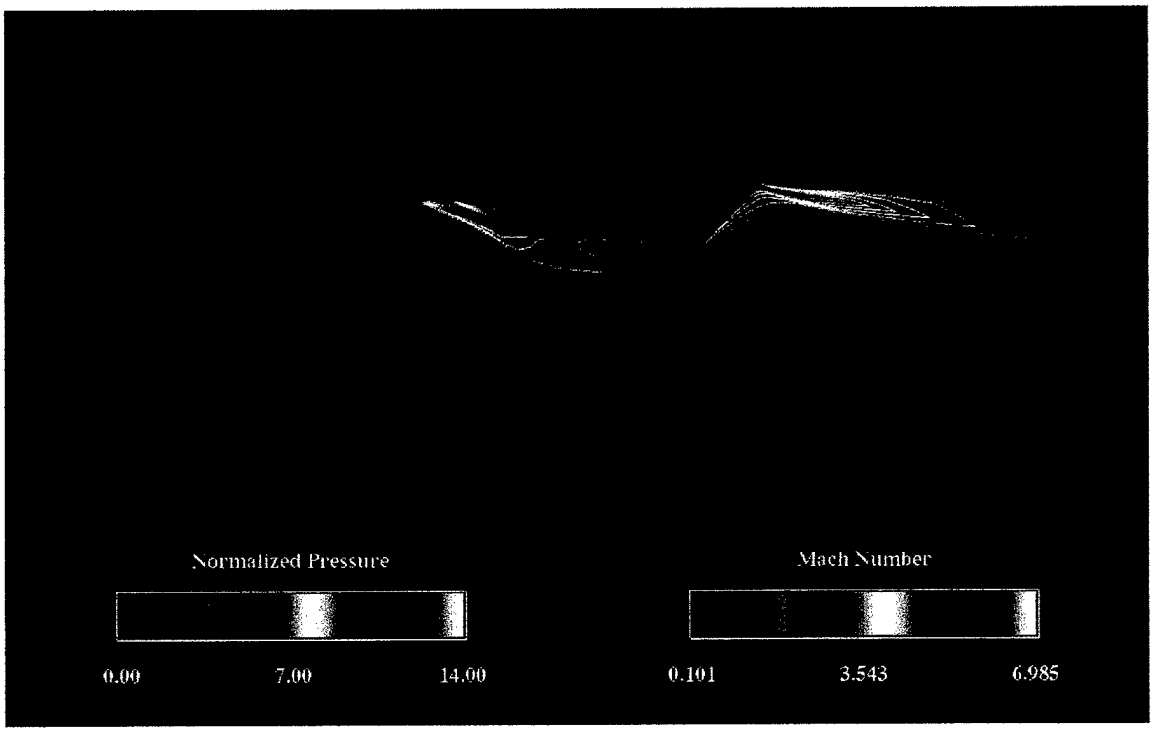

Figure 18. Normalized Surface Pressure and Mach Number Contours, $M_\infty = 6.0$, Inviscid

The Mach contours illustrate the formation of shocks at the nose of the vehicle and at the engine inlet. From the NACA Report 1135 Oblique Shock Chart [Ref. 13], the predicted shock angle for $M_\infty = 6.0$ flow over the 5.2° wedge of the vehicle nose is 13°. Although difficult to measure from the FAST image, this appeared to be the angle at which the shock was computed. At that freestream Mach number the shocks over the engine inlet two-ramp configuration coalesced into a single oblique shock. The engine

inlet however, when modeled as a solid body, dramatically changed the flow angle and caused a distinct shock to form at the engine inlet. Here, where the engine inlet was modeled as a solid body, the engine inlet shock formed at a much higher angle than the shocks off the nose of the vehicle.

2. Mach 6.0 Viscous Results

Due to the tendency of the $M_\infty = 6.0$ solution to go unstable with minor changes in the inputs, the viscous solution was computed from zero iterations. This convergence history (Figure 19) shows that the viscous solution converged more slowly than the inviscid $M_\infty = 6.0$ solution (Figure 15). The viscous effects required additional iterations to allow development of the boundary layer. The drag coefficient and lift coefficient histories shown in Figures 20 and 21, also reflected the presence of viscous effects from the beginning of the computations, rather than showing a change within their values when viscous forces were added.

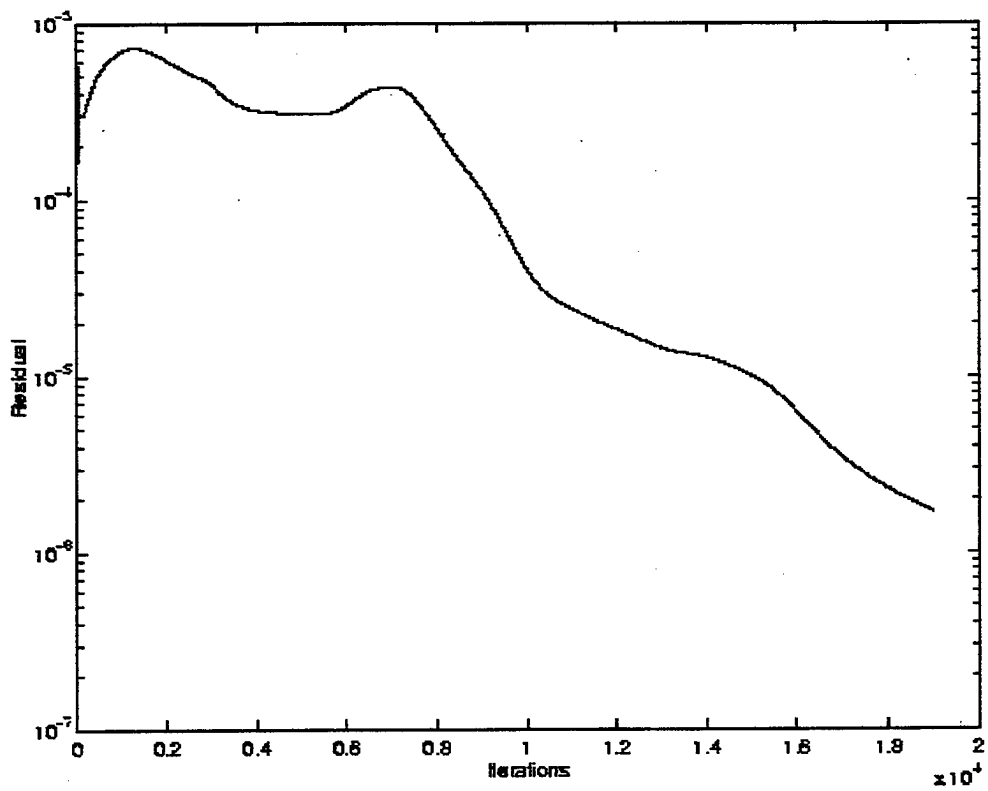

Figure 19. Mach 6.0 (Viscous) Residual Convergence History

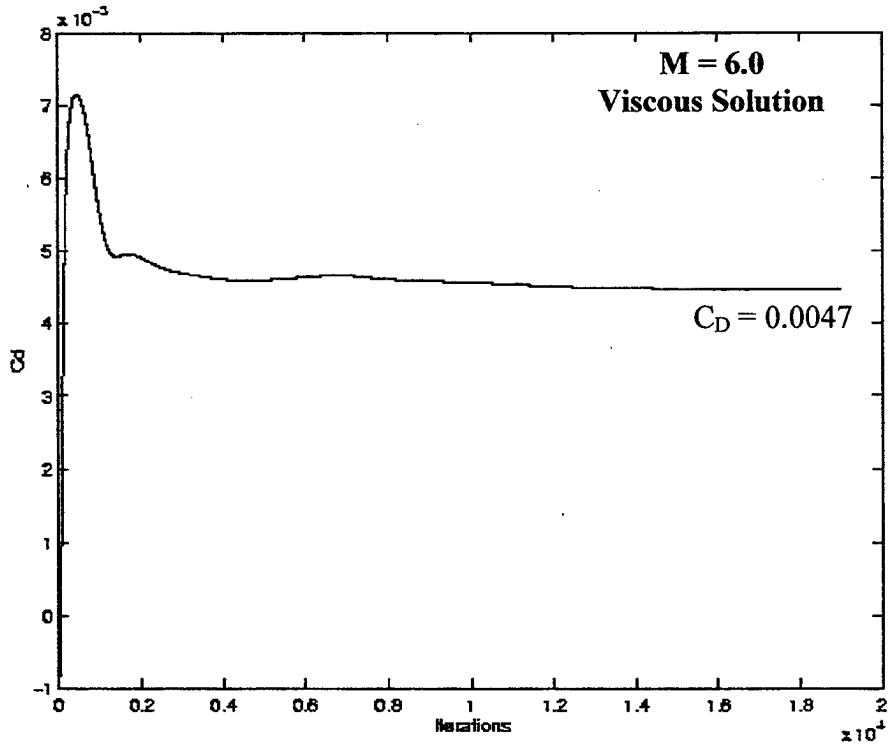

Figure 20. Drag Coefficient vs. Number of Iterations for $M_\infty = 6.0$, Viscous

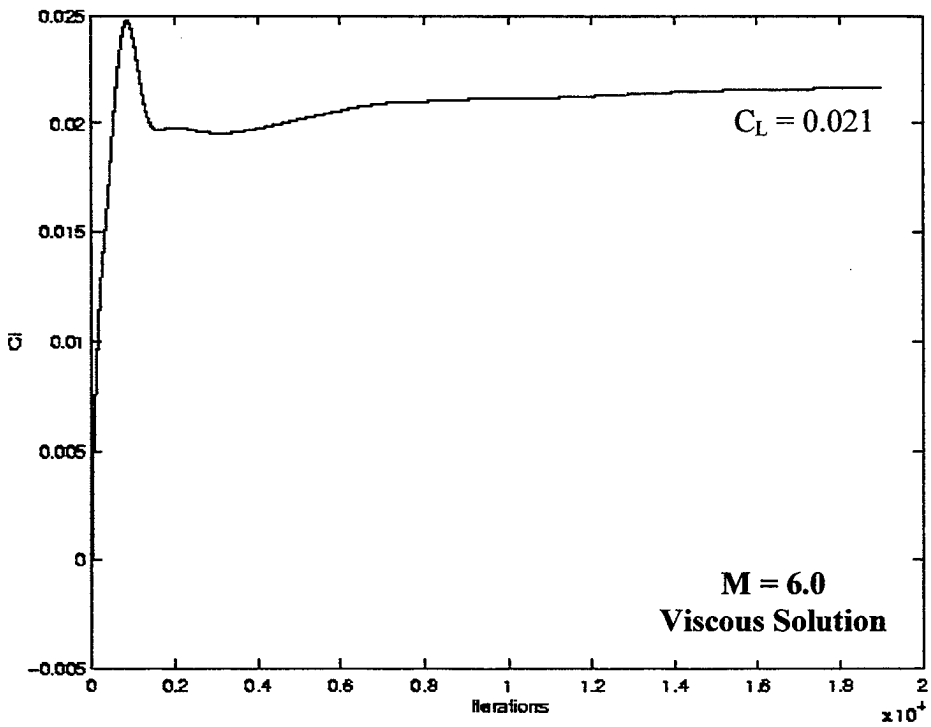

Figure 21. Lift Coefficient vs. Number of Iterations for $M_\infty = 6.0$, Viscous

In Figure 22, the presence of Mach contours in the flowfield near the upper surface of the Price waverider was evidence of the boundary layer formation on that surface. Shocks were more smeared than in the inviscid case and the wake region extended over a larger distance downstream of the trailing edge.

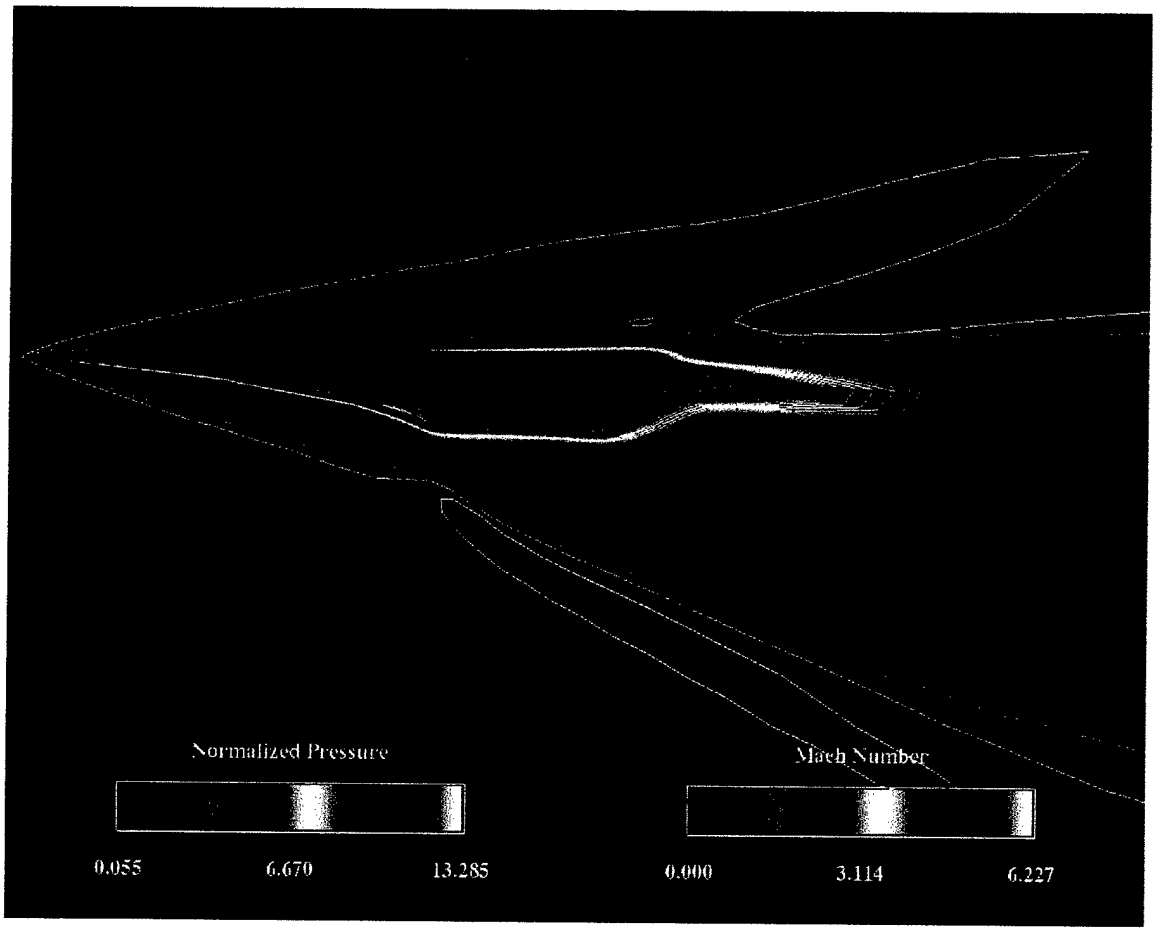

Figure 22. Normalized Surface Pressure and Mach Number Contours, $M_\infty = 6.0$, Viscous

3. Supersonic Trends

Inviscid and viscous solutions were computed for $M_\infty = 1.2$ and $M_\infty = 4.0$, with similar results to the $M_\infty = 6.0$ solutions. The engine flow-through model was only computed for the $M_\infty = 6.0$ flight condition. The results for additional supersonic cases are provided in Appendix C.

C. ENGINE FLOW-THROUGH MODELING

The presence of the extremely high pressure forward of the intake, seen in Figures 18 and 22, did not necessarily represent the true nature of the flowfield of an operating vehicle. To provide data on a more representative configuration engine flow-through was modeled as a follow-on test case to the $M_\infty = 6.0$ computations. This configuration was not modeled for the subsonic case, although the impact is expected to be less significant because the flow in front of an engine in subsonic flight is expected to be slowed significantly at the diffuser and thus will present a surface that more closely resembles a solid body.

The Mach 6.0 engine flow-through computation could not be run from the previously converged $M_\infty = 6.0$ solution because it not only required modification to the boundary conditions, but required the definition of a new set of boundaries. Flow-through was extrapolated from the pressure forward of the intake boundary and the exhaust was modeled as freestream pressure extrapolated flow.

Convergence history for the $M_\infty = 6.0$ engine flow-through case (Figure 23), shows more moderate drops in the residuals than in the initial $M_\infty = 6.0$ solution (Figure 15). Although the residuals began to drop off between 7000 and 8000 iterations, as seen in the previous Mach 6.0 solution, the engine Flow-Through model required nearly twice as many iterations to converge, as the pressure extrapolations from previous iterations were computed as input to follow-on iterations.

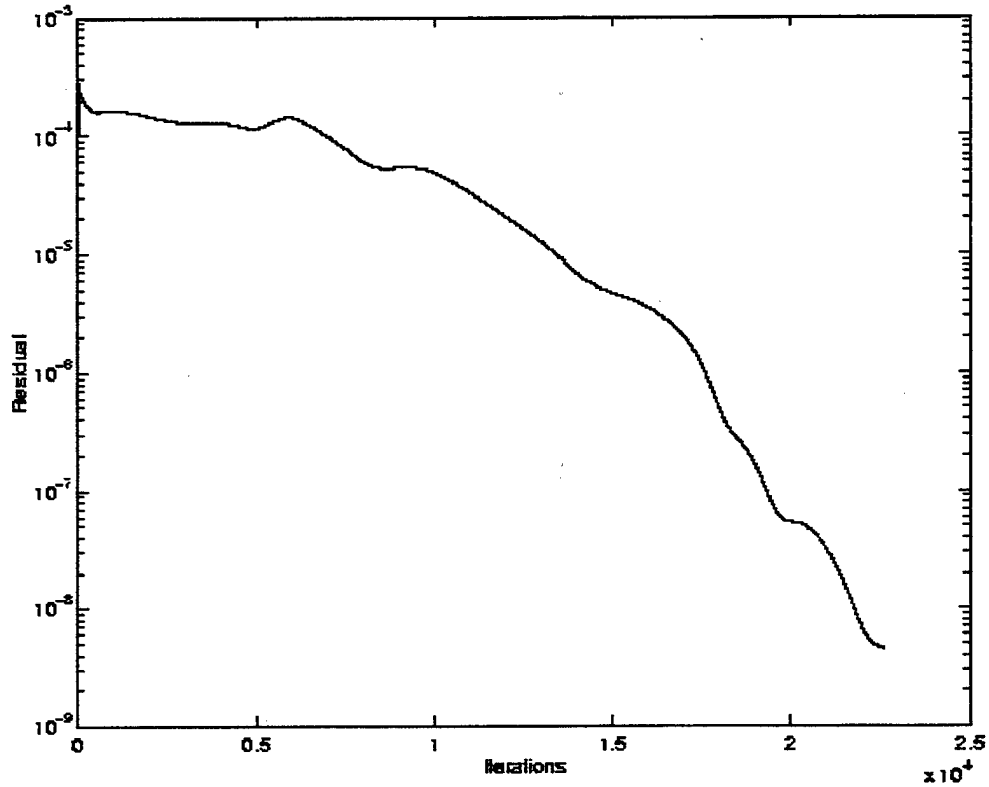

Figure 23. Mach 6.0 (Inviscid) Engine Flow-Through Convergence History

The resulting solution was computed to show decreases in both lift and drag coefficients over the $M_\infty = 6.0$ solution. The lift coefficient, calculated in the inviscid $M_\infty = 6.0$ solution was $C_L = 0.018$, was found in the engine flow-through model to be $C_L = 0.016$. The drag coefficient was found to be $C_D = 0.003$ for the engine flow-through model, whereas previous $M_\infty = 6.0$ solution (without engine flow-through) computed the drag coefficient to be $C_D = 0.0044$. In this calculation, the declining lift was outpaced by the improvements in the drag, resulting in better overall L/D performance than the original calculations demonstrated.

As is illustrated in Figure 24, the pressure at the intake dropped to only twice the freestream static pressure, as opposed to the factor of 14 seen in the initial $M_\infty = 6.0$ solution. Mach number contours also showed that the resulting shocks occurred closer to the body.

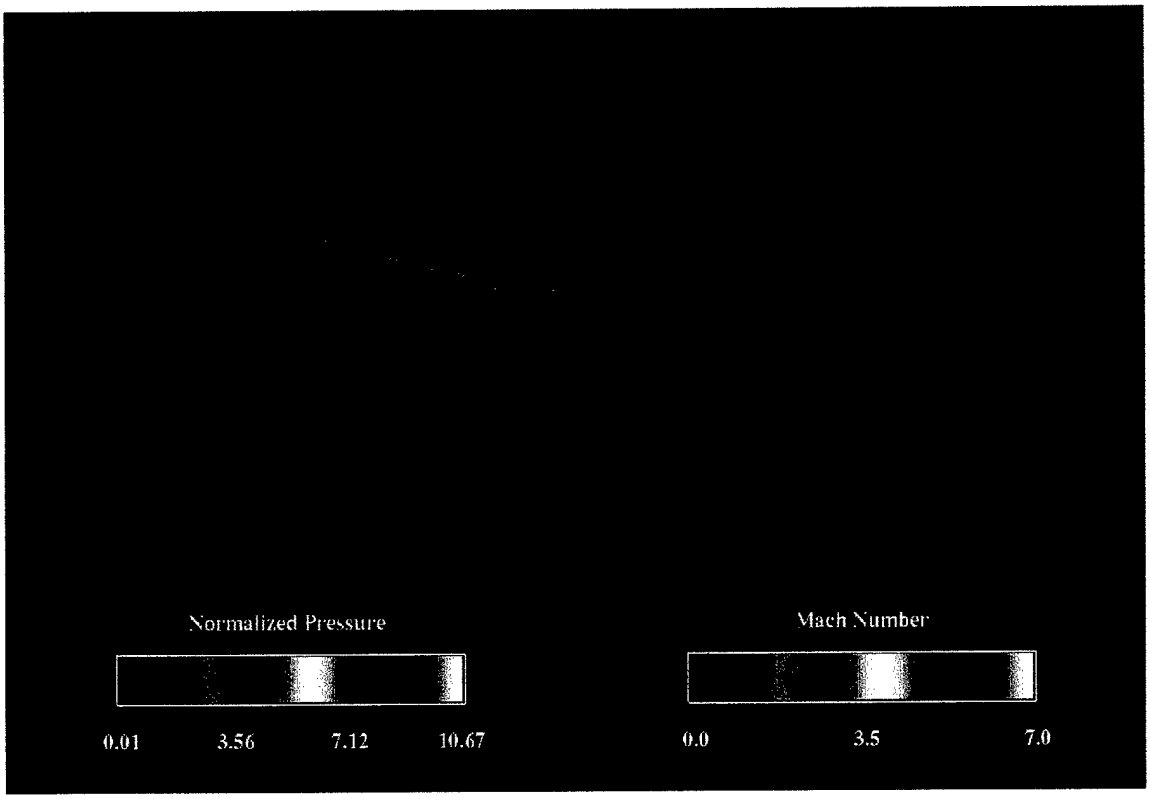

Figure 24. Normalized Surface Pressure and Mach Number Contours, $M_\infty = 6.0$, Engine Flow-Through, Inviscid

D. REYNOLDS NUMBER EFFECTS

Performance of the Price waverider across the spectrum of flight Mach numbers was compared using the lift and drag coefficients and the overall performance factor of the lift-to-drag ratio. The values for lift and drag coefficients were tabulated from the OVERFLOW1.8b output file containing force and moment data. The force and moment file provided the force and moment contributions due to pressure and friction. These results are compiled in Tables 2 and 3. In the inviscid case the contributions due to friction were zero and have not been reported in Table 2. In the viscous cases, the computed contribution of the viscous effects to the lift and drag coefficients, were, in nearly all cases, rounded to zero.

Mach Number	C_L	C_D	L/D	Cm
0.3	-0.0310	0.0194	-1.60	-0.0387
0.4	-0.0329	0.0171	-1.92	-0.0405
0.5	-0.0344	0.0160	-2.15	-0.0424
0.6	-0.0377	0.0159	-2.37	-0.0460
0.7	-0.0402	0.0162	-2.48	-0.0494
0.8	-0.0421	0.0178	-2.37	-0.0530
0.9	-0.0308	0.0230	-1.34	-0.0463
1.2	0.0078	0.0302	0.26	-0.0167
2.0	0.0312	0.0152	2.06	0.0118
4.0	0.0224	0.0064	3.50	0.0108
6.0	0.0184	0.0044	4.20	0.0094

Table 2. Summary of Inviscid Solution Force Coefficients

Mach Number	C_L pressure	C_L friction	C_L total	C_D pressure	C_D friction	C_D total	L/D	Cm
0.3	0.0239	0.0000	-0.0238	0.0169	0.0001	0.0170	-1.40	-0.0332
0.4	0.0203	0.0000	-0.0203	0.0156	0.0001	0.0157	-1.29	-0.0306
0.5	0.0176	0.0000	-0.0176	0.0150	0.0001	0.0150	-1.17	-0.0289
0.6	0.0149	0.0000	-0.0149	0.0149	0.0001	0.0150	-0.99	-0.0272
0.7	0.0109	0.0000	-0.0109	0.0152	0.0001	0.0153	-0.71	-0.0247
0.8	0.0059	0.0000	-0.0059	0.0163	0.0000	0.0164	-0.36	-0.0217
0.9	0.0002	0.0000	-0.0002	0.0201	0.0000	0.0201	-0.01	-0.0186
1.2	-0.0108	0.0000	-0.0108	0.0295	0.0000	0.0296	0.36	-0.0129
2.0	-0.0323	0.0000	-0.0323	0.0155	0.0000	0.0154	2.10	0.0126
4.0	-0.0240	0.0000	-0.0240	0.0070	0.0000	0.0071	3.40	0.0115
6.0	-0.0214	0.0000	-0.0214	0.0047	0.0000	0.0047	4.54	0.0112

Table 3. Summary of Viscous Solution Force Coefficients

These results are compiled for both the viscous and inviscid solutions and shown graphically. Figure 25 shows the lift coefficient as a function of Mach number. The inviscid subsonic lift behavior showed the detrimental effects of separation, although it is not clearly understood what specific effect caused the inviscid lift coefficients to diverge so dramatically from the viscous lift coefficients subsonically. In the supersonic region,

viscous and inviscid lift coefficients showed very good agreement with each other. The implication here is that inviscid solutions closely approximate the behavior of viscous flows, and as such, the viscous effects may be negligible in the initial design phase of supersonic vehicles. The viscous solutions consistently computed higher values for the lift coefficient, which demonstrated the beneficial effects of the attached flow. A significant feature of this configuration was that the lift coefficient does not become positive until the flow is supersonic. In short, the Price waverider, in its current configuration, produced no positive aerodynamic lift until the freestream Mach number became sonic. Studies of the drag coefficient and pitching moment are required to determine the impact of not have positive lift at zero degrees angle-of-attack.

Wind tunnel testing initially performed by Cedrun [Ref. 6] provided a basis of comparison for Huff's follow-on testing [Ref. 7]. Huff demonstrated that his data duplicated Cedrun's original results. Due to the formatting of Cedrun's work, the lift and drag coefficients, with wall and blockage corrections for the wind tunnel, were not provided in tabular form, so for greater accuracy, the values from Huff's work are shown in the comparisons that follow. Since the data of both sets of testing agree, the comparisons made here to Huff's data can be applied to Cedrun's work as well.

The lift coefficient from Huff's highest speed wind tunnel tests is plotted on Figure 25 at $M_\infty = 0.15$. Seen here it lies slightly below the extrapolated path of the viscous solution of computed lift coefficients, demonstrating that the wind tunnel test results are slightly less optimistic than the computed solution. The reason for this is believed to be the addition of the trailing edge cusp on the computational waverider model.

The single engine flow-through configuration lift coefficient is also plotted on Figure 25 and shows the slight decrease in lift at $M_\infty = 6.0$. This is due to the angle of the shock formed at the engine inlet. In the engine flow-through model, this shock was slightly more oblique than the shock seen in the solid body engine model at $M_\infty = 6.0$. The more oblique shock in the engine flow-through model causes a smaller pressure rise across the shock, thus the pressure on the lower surface of the waverider body is less.

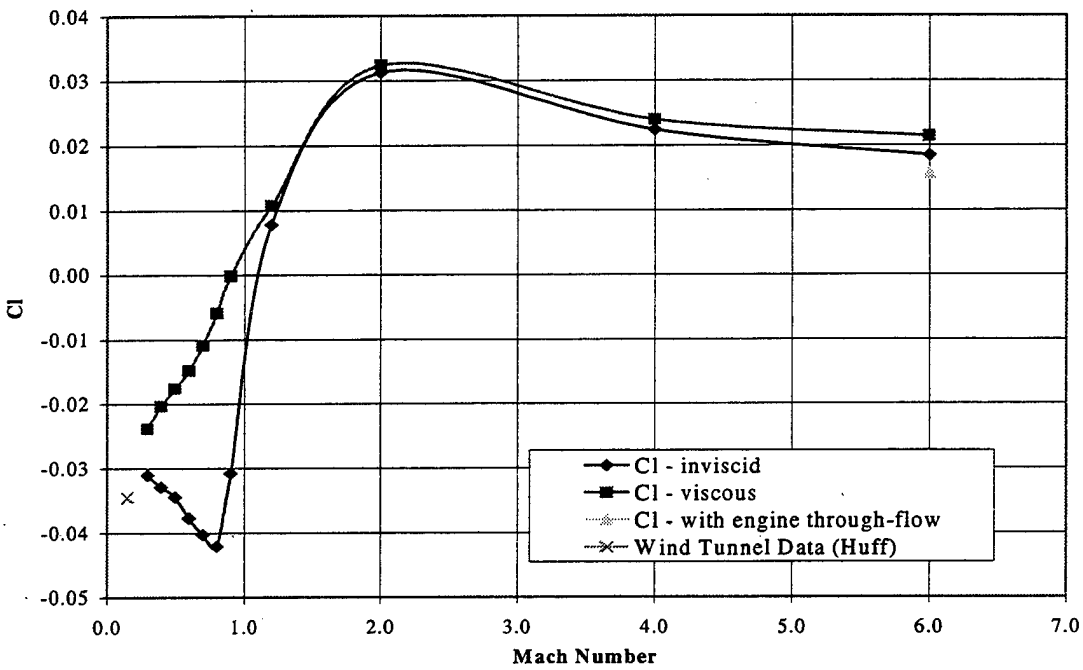

Figure 25. Lift Coefficient vs. Mach Number

In Figure 26, the plot of drag coefficient versus Mach number, we see the transonic drag rise across $M_\infty = 1.0$ in both the viscous and inviscid solutions. The dominant effect of the pressure drag over any viscous forces is supported by the close agreement of these two sets of data through the entire Mach number range computed, $0.3 \leq M_\infty \leq 6.0$. The trough in drag in the subsonic region was an unexpected occurrence. The subsonic flowfield results, shown in Appendix C, indicate that the stagnation point migrated from a position slightly aft and under the nose of the vehicle at $M_\infty = 0.3$, to a position at the nose for $M_\infty = 0.5$ or 0.6. This stagnation point migration presented a more streamlined body to the freestream flow and resulted in a decrease in the drag coefficient. This streamlining effect was overcome by the drag rise in the transonic region. This transonic drag rise was the result of the presence of regions of supersonic flow that had to shock back to freestream along the surface of the body. The presence of these shocks caused the early onset of separation, which increased the pressure drag felt by the body.

Included within the graphical representation of drag coefficients is the $M_\infty = 0.15$ value of C_D from Huff's wind tunnel tests. This point lies slightly above the extrapolation of the computed solutions. Also plotted is the drag coefficient for the $M_\infty = 6.0$ engine flow-through configuration. As in Figure 24, the modeling of engine flow-through reduced the shock angle, and presented a more streamlined body to the freestream flow, which reduced the drag significantly.

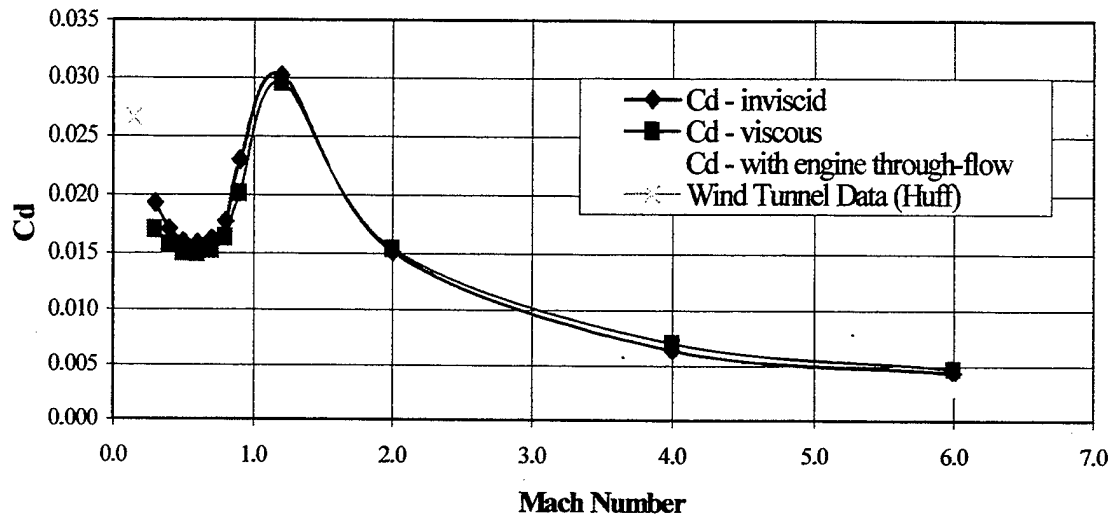

Figure 26. Drag Coefficient vs. Mach Number

Overall performance of the Price waverider is shown in Figure 27. The plot of lift-to-drag ratio versus Mach Number shows the optimum performance at $M_\infty = 6.0$. This result was expected, since the vehicle configuration was optimized for $M_\infty = 6.0$, although this performance indicator did not reflect the product of lift-to-drag ratio and specific impulse. This study did not include the estimation of engine performance. It should also be noted that, for purposes of consistency throughout the study, all Mach numbers and Reynolds numbers were computed at sea level, an unrealistic environment for the $M_\infty = 6.0$ flight condition.

The engine flow-through performance indicated that the decrease in drag in this configuration outpaced the decline in lift performance. Also plotted are the $M_\infty = 0.15$ lift-to-drag ratio for Huff's wind tunnel test data which lies in the plane of the extrapolated L/D curve from the computed solutions.

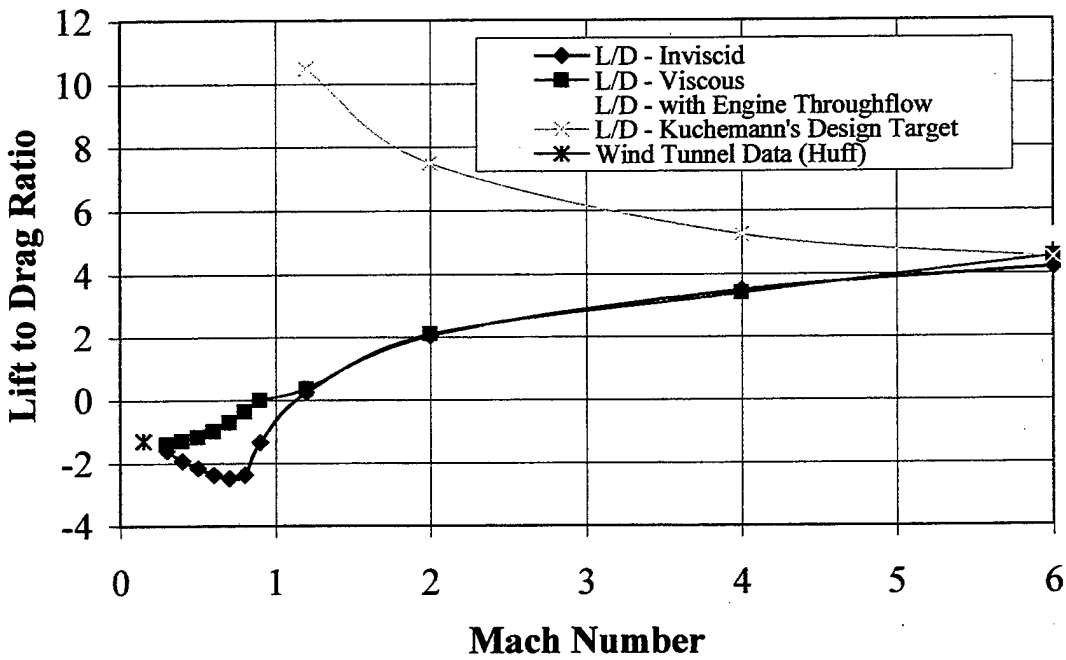

Figure 27. Lift-to-Drag Ratio vs. Mach Number

Maximum L/D performance for a given design Mach number waverider is shown for the supersonic range. Shown here, Kuchemann's maximum on-design performance is compared to the off-design performance data for the Price waverider. This estimate was based on Kuchemann's equation [Ref. 3] of what should be attainable in optimized design:

$$\frac{L}{D} = \frac{3(M_\infty + 3)}{M_\infty}$$

Kuchemann's equation is based on empirical data and predicts that, in the limit as M_∞ goes to infinity, L/D will asymptote to 3.0. At the design Mach number of $M_\infty = 6.0$,

all L/D performance values are shown to converge, demonstrating close agreement between the computed and the theoretical L/D performance of the vehicle. The predicted value of L/D at $M_\infty = 6.0$ is 4.5. This performance is closely matched by the computed values of L/D = 4.19 for the inviscid solution, L/D = 4.54 for the viscous solution and L/D = 5.17 for the engine flow-through solution. Note that both the viscous solution and the engine flow-through solution exceed that maximum predicted value for L/D. Anderson [Ref. 1], disputed Kuchemann's performance limits, estimating that L/D_{MAX} for supersonic vehicles should be about 50% higher than Kuchemann's predictions for Mach 6.0 optimized vehicles. Anderson, however, based that dispute on a class of waverider-configured vehicles generated using his viscous-optimization routine. While the viscous effects have been taken into account in the computations reported herein, the Price waverider was designed using an inviscid optimization routine.

Figure 28 shows the value of the pitching moment coefficient for the computed solutions. Based on the coordinate system used, the positive pitching moment represents a nose down pitching force. Without employment of control surfaces, the Price waverider appears to be statically unstable. The datum employed here is the y-axis, the nose of the vehicle. The inviscid solution shown here continues to demonstrate the adverse effect of the non-physically representative wake in the CFD solution, and the subsonic values for C_M do not reflect a realistic solution.

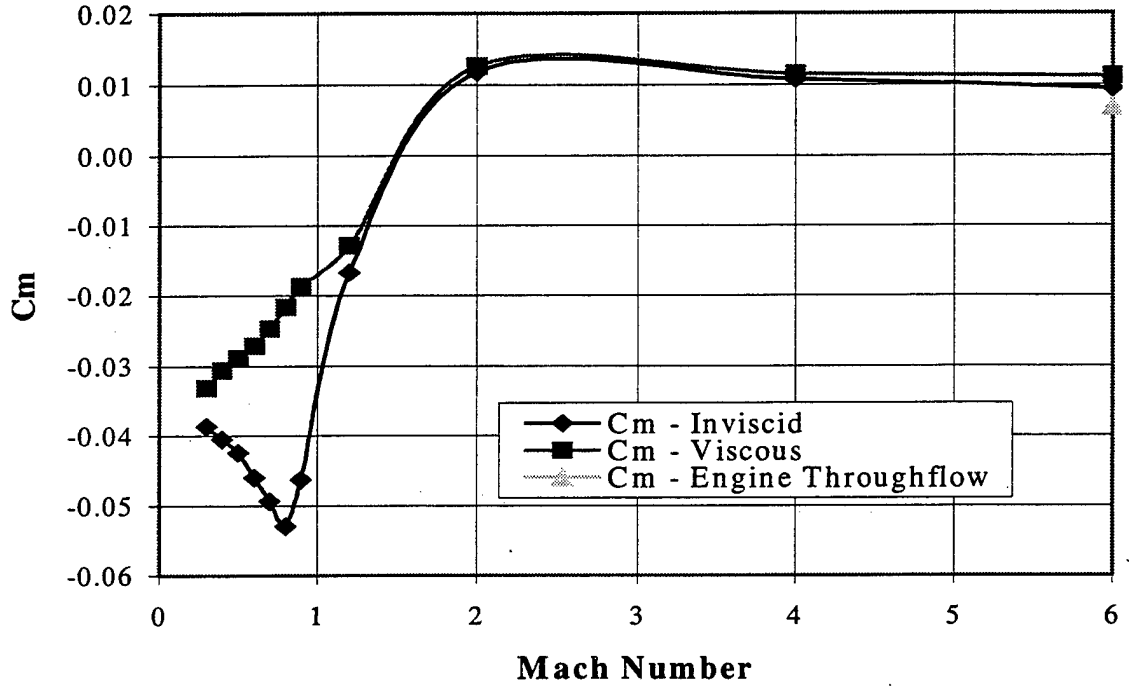

Figure 28. Pitching Moment Coefficient vs. Mach Number

As is seen in Figures 25 through 28, the computed force coefficients demonstrated agreement with the experimental data from Huff's low-speed wind tunnel testing. Overall, the modeling of engine flow-through improved the performance data. Close agreement between the viscous and inviscid solutions in the supersonic region supported the premise that, for a first approximation, viscous effects can be neglected in the initial design phases. This argument cannot be supported for the subsonic region, as the effects of the non-physically representative wake cause lift, L/D performance and pitching moment parameters to diverge from the viscous case.

E. ALPHA SWEEP

Computations for the range of angles of attack of $-10° \leq \alpha \leq +10°$ were conducted at $M_\infty = 0.3$, for viscous conditions. The convergence history, as well as lift and drag coefficient history, were similar to those seen in the zero degree angle of attack solution for $M_\infty = 0.3$, viscous flow. The calculated effect on the lift coefficient is shown

in Figure 29. Wind tunnel data for $M_\infty = 0.15$ from Huff's thesis are shown for comparison. The computed values demonstrated a lift curve slope of $C_{L\alpha} = 0.884$, compared to the wind tunnel test lift curve slope of $C_{L\alpha} = 2.526$. This discrepancy is most likely due to the coarseness of the grid. It is also possible that a better match may be obtained by using a different turbulence model for the computations. Cedrun's test results, although not plotted, matched Huff's data. Cedrun noted no marked difference in the lift curve slope relative to Mach number, so the impact of the difference in freestream Mach number between the wind tunnel data and the computed solutions was discounted as the cause for the differential in lift curve slope.

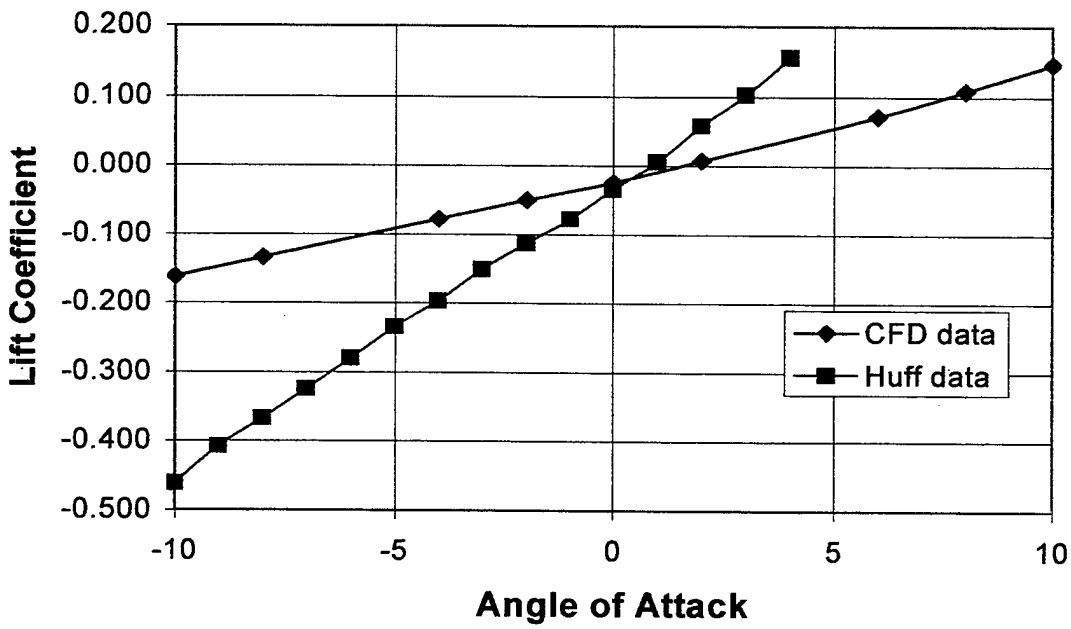

Figure 29. Lift Coefficient vs. Angle of Attack

The onset of stall was not predicted to occur within the range of angles of attack for which solutions were computed. Cedrun's lowest speed wind tunnel test ($M_\infty \approx 0.003$) concluded that stall occurred at 34 degrees AOA. Neither Huff nor Cedrun achieved stall in higher speed wind tunnel tests, due to the total force vector exceeding the wind tunnel sting force constraint.

Figure 30 shows the impact of angle of attack on the drag coefficient for both wind tunnel data and computed solutions. The computed drag coefficient was consistently lower than the wind tunnel test data. The optimistic prediction of drag coefficients was presumed to be the result of the addition of the trailing edge cusp. The addition of the cusp also caused a smaller variation in drag coefficient over the range of angles of attack, thus flattening the curve when compared to the wind tunnel data. Minimum drag was found to occur at zero degrees angle of attack.

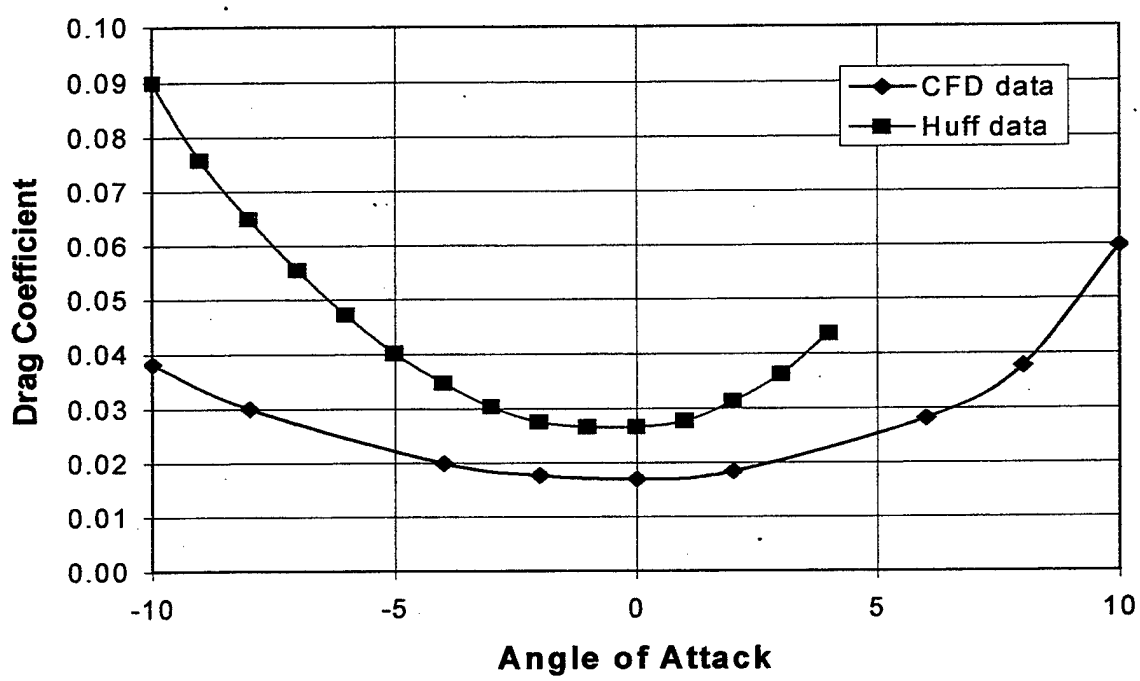

Figure 30. Drag Coefficient vs. Angle of Attack

A final comparison was made between the wind tunnel data and the computed solutions' L/D performance. Shown in Figure 31, the measurements on the wind tunnel model showed a steeper variation of L/D with changing angle of attack. The lift curve slope variation was the largest contributor to the difference in L/D performance, however the addition of the trailing edge cusp also played a role in the differences in performance. Maximum L/D performance was calculated to be L/D = 2.87, which occurred at eight degrees angle of attack. The wind tunnel data showed a maximum of L/D = 3.58, which

occurred at four degrees of angle of attack. This value may have continued to rise had higher AOA's been tested. At negative angles of attack the computed L/D performance predicts a minimum L/D between –4 and –8 degrees, closely matching the wind tunnel measurements, which measured a minimum L/D at –6 degrees.

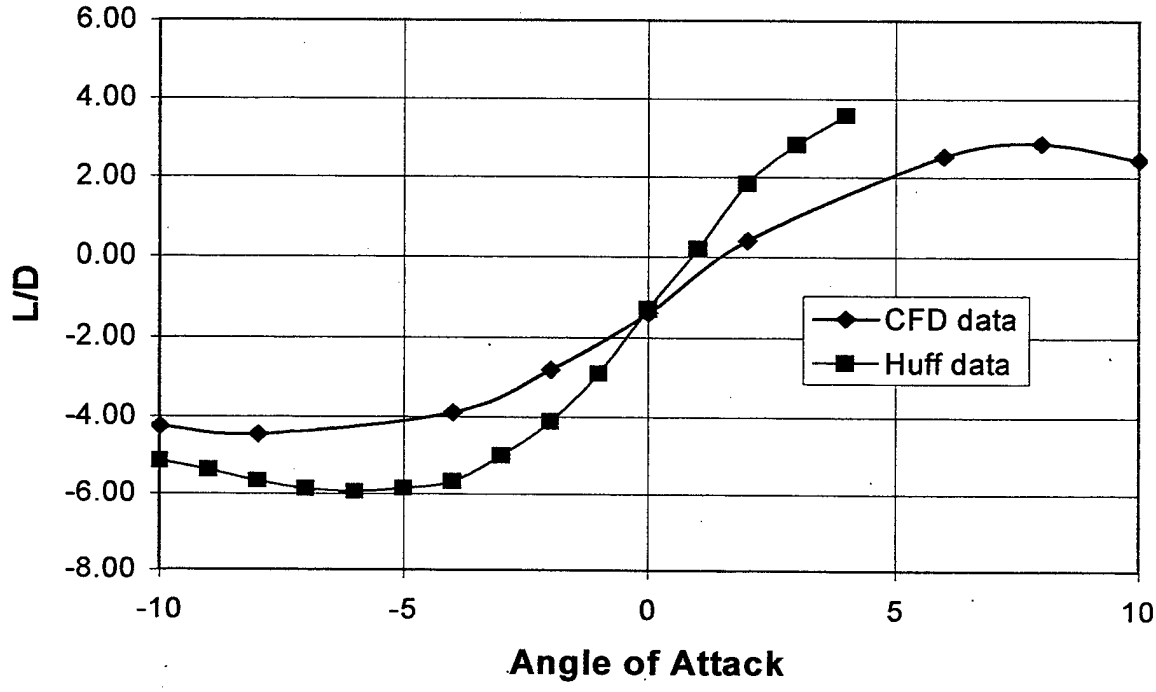

Figure 31. Lift-to-Drag Ratio vs. Angle of Attack

The normalized surface pressure and Mach number contours for the positive 10 degrees angle of attack case are shown in Figure 32. The sharp Mach number contour gradient showed the presence of the boundary layer on the upper surface of the body. Mach contours outlined the stagnation point located aft of the nose on the lower surface and indicated a region of separated flow on the upper surface. The portion of the upper surface where flow was separated was also indicated by the region of lower surface pressure seen along the leading edge from the nose to mid-chord.

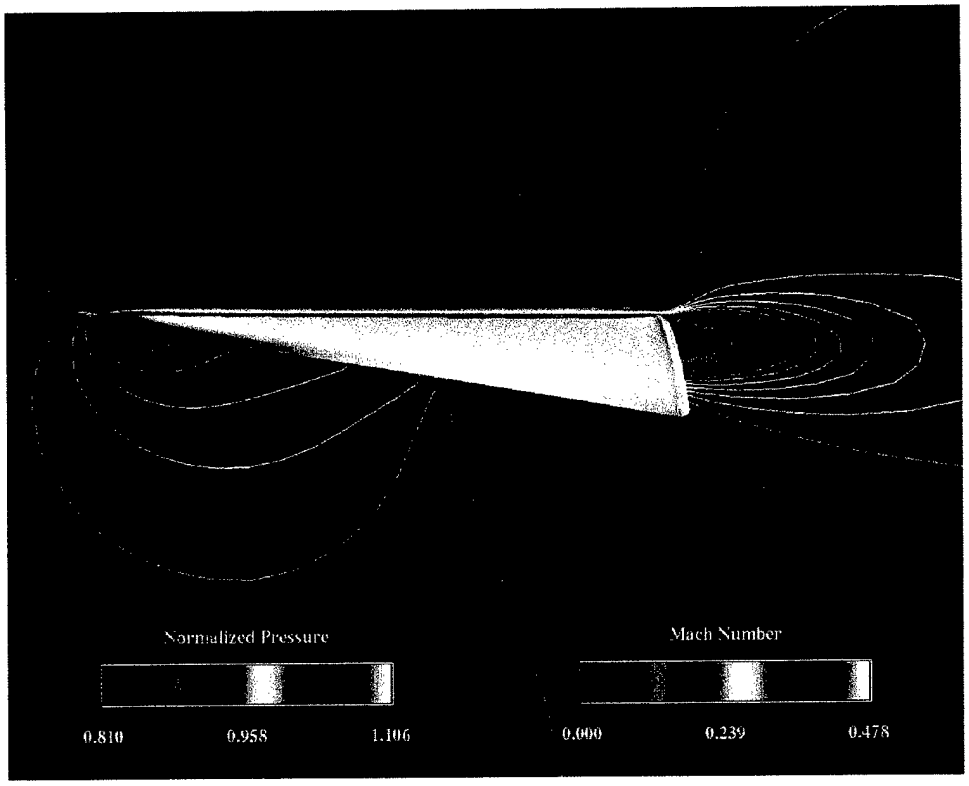

Figure 32. Normalized Surface Pressure and Mach Contours, Mach 0.3 at 10° AOA

F. CFD VALIDITY

Based on the data presented above, the CFD appeared to calculate solutions, which represented realistic flowfields. While computational limitations prohibited calculation of the flowfield solution below $M_\infty = 0.3$, the computed lift and drag coefficients and L/D for $0.3 \leq M_\infty \leq 6.0$ trended toward the values obtained in the $M_\infty = 0.15$ tests conducted by Huff and Cedrun. While precise comparison was not made, due to the mismatch of Mach numbers in the CFD and wind tunnel test, it appeared that the CFD trends were slightly optimistic. The optimism of the CFD calculations for lift and drag was believed to be the result of the addition of the trailing edge cusp to the CFD model.

Angle of attack sweeps showed disagreement in all computed performance parameters. While some of the discrepancy was attributable to the addition of the trailing

edge cusp, the significant difference in the lift curve slope is believed to be the result of the grid coarseness and turbulence model. Despite disagreement at both positive and negative angles of attack, the solutions at zero degrees angle of attack were in close agreement. For that reason, the zero degree AOA data were still considered valid.

The flight conditions considered herein represent the Mach number and Reynolds number calculated for the 15-inch model at sea level. To better approximate the boundary layer development, Reynolds numbers should be chosen to reflect the length of the Price waverider, rather than the model root mean chord.

G. CFD LIMITATIONS

For purposes of this study, a broad range of Mach numbers was examined, however the extent to which existing data could be matched was limited by the flow solver. Flow solutions were not obtained for Mach numbers below $M_\infty = 0.3$, whereas wind tunnel test data was not available above $M_\infty = 0.15$. This mismatch prevented the validation of CFD results with corresponding wind tunnel data.

Difficulty in creating a grid that correctly modeled the blunt trailing edge, led to the addition of the trailing edge cusp to the CFD model. This difference in configuration is believed to have caused the lift and drag coefficients to be more optimistic than the wind tunnel test data.

The use of the elliptic solver, GRIDGEN3D, to resolve the negative cell volumes in the grid also tended to pull grid points away from the body of the waverider. Due the migration of grid points away from the body of the waverider, the boundary layer calculations, while seen in the Mach number contours, may not be representative of actual boundary layer size.

V. CONCLUSIONS

The computational fluid dynamic analysis of the Price waverider was demonstrated to produce valid results for subsonic and supersonic flowfield computations. The prediction of lift and drag coefficients and L/D closely resembled the data obtained in wind tunnel testing. Although the lift and drag coefficients appeared slightly more optimistic than the wind tunnels tests, this was likely the result of the addition of the cusped trailing edge. While that modification was made to facilitate the grid generation, the physical impact was to reduce the pressure drag and increase the lift through the expansion over the upper surface trailing edge. The differences in the computed and measured values were in the same order of magnitude as the tunnel wall corrections applied to the wind tunnel results.

The use of computational methods provided the opportunity to expand the body of knowledge available defining the behavior of flow surrounding the Price waverider over a broad range of flight conditions.

The angle of attack sweep calculation, while showing similar trends in performance parameters, did not achieve very good agreement, except at zero degrees angle of attack. The lift curve slope showed the largest discrepancy when compared to the wind tunnel data. This was believed to be the result of the grid coarseness. Further study is required to determine whether grid refinements or use of a different turbulence model would improve agreement.

Instability of the solution at high Mach numbers precluded the extension of CFD analysis to flight conditions above the design condition. Time steps required to maintain a stable solution at $M_\infty = 6.0$ were an order of magnitude smaller than any other computation. Similarly, the excessive computational time required to compute the low subsonic solutions, prohibits the use of OVERFLOW1.8b to speeds lower than $M_\infty = 0.3$.

The computed flow solutions demonstrated several areas of concern. The first concern was the lack of positive lift generation in subsonic flight at zero degrees angle of attack. With a tendency to pitch up at this angle of attack present, the risk of flying at a slightly nose up attitude, to gain positive lift, is that this attitude will exacerbate the

pitching moment. The second area of concern was the transonic drag rise and the effect of the drag trough in the subsonic regime on the specific excess power curves.

A number of opportunities exist to improve the body of knowledge regarding the Price waverider and in the extension of the existing analysis.

A. GRID REFINEMENTS

The existing grid provided a computational space that allowed the computation of reasonable solutions, however, there were a number of areas that needed improvement. The existing grid, after using the elliptical solver to resolve the presence of negative cell volumes, failed to maintain the initially specified grid spacing near the body except at the centerline where all points were held as fixed points. This spacing contributed to inaccuracies in the computation of viscous drag insofar as the velocity gradient in the boundary layer was dependent on the existence of sufficient points near the body to capture the gradient correctly. Additionally, the lift curve slope in the alpha sweep did not mirror the wind tunnel results. Grid density was believed to be the reason for this disagreement.

The addition of the cusp at the trailing edge of the Price waverider, while a likely design change in the real world, did not reflect the vehicle as-tested. It was seen that the lift and drag forces computed over the existing grid were optimistic when compared to the wind tunnel test data. Use of multi-block grid generation techniques may improve the opportunity to match the grid geometry to the wind tunnel model

It should be noted that the leading edge of the computational model was represented by a single point line, with no leading edge radius. This contributed to a departure from both the model, as-tested, and the real-world vehicle requirements. While the leading edge radius of the Price waverider was not included in the design criteria, it can be safely assumed that the leading edge would have to have some bluntness. An infinitely thin leading is unrealistic to build, and would not be able to withstand the high heating conditions produced at hypersonic speeds. This lack of bluntness at the leading edge contributed to unrealistic boundary layer development.

In general, the grid was fairly coarse, as only 45 points along the length of the waverider body were used during the computations. Grid dependence could be seen in the unevenness of the Mach contours in several of the solutions.

B. OPPORTUNITIES FOR FURTHER TESTING

The use of a multi-grid computational model would enable the closer examination of some aspects of the flowfield. This method could also be used to make modifications to the basic waverider, to include cockpit, vertical tails or high-lift devices to gain a better understanding of the aerodynamic impacts of varying configurations. Included in this list is the modeling of the engine as a thrust producing element rather than as a solid body or a flow-through duct. As with the employment of a cusped trailing edge, a number of configuration changes or proposed changes will require analysis before the feasibility of the Price waverider, or a derivative, can be fully assessed.

This study did not examine the effects of yaw angles or the combinations of angle-of-attack and yaw on the flowfield. The opportunity, therefore, exists to further the understanding of the flight characteristics of the Price waverider at those off-design flight conditions.

To date, supersonic wind tunnel testing has not been accomplished for the Price waverider. A study that combined supersonic wind tunnel test data, with the results provided herein would serve to validate the CFD code further.

THIS PAGE INTENTIONALLY LEFT BLANK

LIST OF REFERENCES

1. Anderson, John D., Bowcutt, Kevin G. and Capriotti, Diego, "Numerical Optimization of Conical Flow Waveriders Including Detailed Viscous Effects", University of Maryland, 1987.

2. Rasmussen, M. L. and He, X., "Computational Analysis of Off-Design Waveriders", AIAA-93-3488-CP, American Institute of Aeronautics and Astronautics, Inc., 1993.

3. Newberry, C. F., "The Conceptual Design of Deck-Launched Waverider Configured Aircraft," Aircraft Design, Vol. I, No. 3, September 1998, pp 159-191. (Also AIAA-95-6155, 1995)

4. Price, David R. , Optimization and Performance Analysis of a Supersonic Conical-Flow Waverider for a Deck-Launched Intercept Mission, Master's Thesis, Naval Postgraduate School, Monterey, California, June 1993.

5. Johnson, Lowell N., Hydrodynamic Flowfield Visualization Studies of a Mach 6 Waverider, Master's Thesis, Naval Postgraduate School, Monterey, California, March 1994.

6. Cedrun, Mark E., Low-Speed Wind Tunnel Testing of the NPS/NASA Ames Mach 6 Optimized Waverider, Master's Thesis, Naval Postgraduate School, Monterey, California, June 1994.

7. Huff, Michael R., A Labview© Based Wind Tunnel Data Acquisition System, Master's Thesis, Naval Postgraduate School, Monterey, California, September 1998.

8. Pessin, David N., Aerodynamic Analysis of Hypersonic Waverider Aircraft, Master's Thesis, California Polytechnic State University, San Luis Obispo, California, March 1993.

9. Steinbrenner, John P., and Chawner, John R., GRIDGEN Manual, MDA Engineering, Arlington, TX, October 1984.

10. Buning, Pieter G., Jesperson, Dennis C., Pulliam, Thomas H., Chan, William H, Slotnick, Jeffrey P., Krist Steven E. and Renze, Kevin J., OVERFLOW User's Manual, NASA Ames Research Center, March 1998.

11. Walatka, Pamela P., and Clucas, Jean, FAST User's Manual, Computer Science Corporation, June 1993.

12. Tannehill, John C., Anderson, Dale A., and Pletcher, Richard H., Computational Fluid Mechanics and Heat Transfer, Second Edition, Taylor and Francis, Washington D. C., 1997.

13. NACA Report 1135, "Equations, Tables, and Charts for Compressible Flow", 1953.

APPENDIX A. WAVERIDER SURFACE GRID POINTS

1			1		
0.00000	0.00000	0.00000	0.00000	0.00000	0.00000
2			2		
0.00436	0.00000	-0.00001	0.00436	0.00000	0.00036
0.00436	0.01629	0.00082	0.00436	0.01629	0.00082
3			3		
0.01047	0.00000	0.00001	0.01047	0.00000	0.00090
0.01047	0.01629	0.00080	0.01047	0.01630	0.00132
0.01047	0.03258	0.00170	0.01047	0.03258	0.00170
4			4		
0.01837	0.00000	0.00001	0.01837	0.00000	0.00157
0.01837	0.01629	0.00083	0.01837	0.01632	0.00202
0.01837	0.03258	0.00170	0.01837	0.03261	0.00237
0.01837	0.04887	0.00262	0.01837	0.04887	0.00262
5			5		
0.02809	0.00000	0.00001	0.02809	0.00000	0.00239
0.02809	0.01629	0.00083	0.02809	0.01634	0.00284
0.02809	0.03258	0.00170	0.02809	0.03265	0.00320
0.02809	0.04887	0.00263	0.02809	0.04892	0.00345
0.02809	0.06515	0.00361	0.02809	0.06515	0.00361
9			9		
0.03966	0.00000	0.00001	0.03966	0.00000	0.00339
0.03966	0.01629	0.00084	0.03966	0.01636	0.00384
0.03966	0.03258	0.00170	0.03966	0.03269	0.00418
0.03966	0.04887	0.00262	0.03966	0.04899	0.00443
0.03966	0.06515	0.00362	0.03966	0.06524	0.00459
0.03966	0.06824	0.00378	0.03966	0.06831	0.00459
0.03966	0.06839	0.00379	0.03966	0.06846	0.00459
0.03966	0.06854	0.00380	0.03966	0.06861	0.00459
0.03966	0.08143	0.00467	0.03966	0.08143	0.00467
10			10		
0.05312	0.00000	0.00001	0.05312	0.00000	0.00455
0.05312	0.01629	0.00083	0.05312	0.01638	0.00499
0.05312	0.03258	0.00170	0.05312	0.03274	0.00534
0.05312	0.04887	0.00263	0.05312	0.04907	0.00558
0.05312	0.06515	0.00361	0.05312	0.06534	0.00573
0.05312	0.06824	0.00381	0.05312	0.06842	0.00575
0.05312	0.06839	0.00382	0.05312	0.06857	0.00575
0.05312	0.06854	0.00383	0.05312	0.06872	0.00575

0.05312	0.08143	0.00468	0.05312	0.08156	0.00582
0.05312	0.09770	0.00583	0.05312	0.09770	0.00583
11			11		
0.06850	0.00000	0.00001	0.06850	0.00000	0.00588
0.06850	0.01629	0.00084	0.06850	0.01641	0.00633
0.06850	0.03258	0.00170	0.06850	0.03280	0.00667
0.06850	0.04887	0.00262	0.06850	0.04915	0.00689
0.06850	0.06515	0.00362	0.06850	0.06546	0.00705
0.06850	0.06824	0.00382	0.06850	0.06854	0.00707
0.06850	0.06839	0.00382	0.06850	0.06869	0.00707
0.06850	0.06854	0.00383	0.06850	0.06884	0.00707
0.06850	0.08143	0.00468	0.06850	0.08170	0.00712
0.06850	0.09770	0.00584	0.06850	0.09787	0.00713
0.06850	0.11397	0.00709	0.06850	0.11397	0.00709
12			12		
0.08584	0.00000	0.00001	0.08584	0.00000	0.00740
0.08584	0.01629	0.00083	0.08584	0.01645	0.00784
0.08584	0.03258	0.00170	0.08584	0.03287	0.00816
0.08584	0.04887	0.00263	0.08584	0.04925	0.00840
0.08584	0.06515	0.00362	0.08584	0.06559	0.00854
0.08584	0.06824	0.00381	0.08584	0.06868	0.00856
0.08584	0.06839	0.00382	0.08584	0.06883	0.00856
0.08584	0.06854	0.00383	0.08584	0.06898	0.00856
0.08584	0.08143	0.00468	0.08584	0.08186	0.00860
0.08584	0.09770	0.00584	0.08584	0.09807	0.00860
0.08584	0.11397	0.00710	0.08584	0.11419	0.00855
0.08584	0.13022	0.00847	0.08584	0.13022	0.00847
13			13		
0.10517	0.00000	-0.00001	0.10517	0.00000	0.00908
0.10517	0.01629	0.00083	0.10517	0.01649	0.00953
0.10517	0.03258	0.00170	0.10517	0.03294	0.00983
0.10517	0.04887	0.00263	0.10517	0.04937	0.01009
0.10517	0.06515	0.00361	0.10517	0.06574	0.01021
0.10517	0.06824	0.00381	0.10517	0.06883	0.01022
0.10517	0.06839	0.00382	0.10517	0.06898	0.01022
0.10517	0.06854	0.00383	0.10517	0.06913	0.01022
0.10517	0.08143	0.00469	0.10517	0.08204	0.01023
0.10517	0.09770	0.00583	0.10517	0.09829	0.01024
0.10517	0.11397	0.00710	0.10517	0.11444	0.01019
0.10517	0.13022	0.00847	0.10517	0.13051	0.01009
0.10517	0.14646	0.00998	0.10517	0.14646	0.00998
14			14		
0.12654	0.00000	0.00000	0.12654	0.00000	0.01098
0.12654	0.01629	0.00083	0.12654	0.01653	0.01143
0.12654	0.03258	0.00171	0.12654	0.03303	0.01175

0.12654	0.04887	0.00260
0.12654	0.06515	0.00361
0.12654	0.06824	0.00381
0.12654	0.06839	0.00382
0.12654	0.06854	0.00383
0.12654	0.08143	0.00469
0.12654	0.09770	0.00582
0.12654	0.11397	0.00710
0.12654	0.13022	0.00848
0.12654	0.14646	0.00998
0.12654	0.16269	0.01164

15

0.14999	0.00000	0.00001
0.14999	0.01629	0.00084
0.14999	0.03258	0.00171
0.14999	0.04887	0.00262
0.14999	0.06515	0.00362
0.14999	0.06824	0.00382
0.14999	0.06839	0.00382
0.14999	0.06854	0.00383
0.14999	0.08143	0.00468
0.14999	0.09770	0.00584
0.14999	0.11397	0.00708
0.14999	0.13022	0.00848
0.14999	0.14647	0.00999
0.14999	0.16269	0.01165
0.14999	0.17890	0.01348

16

0.17554	0.00000	0.00001
0.17554	0.01629	0.00084
0.17554	0.03258	0.00171
0.17554	0.04887	0.00262
0.17554	0.06515	0.00359
0.17554	0.06824	0.00382
0.17554	0.06839	0.00383
0.17554	0.06854	0.00384
0.17554	0.08143	0.00468
0.17554	0.09770	0.00584
0.17554	0.11397	0.00709
0.17554	0.13022	0.00848
0.17554	0.14646	0.00996
0.17554	0.16269	0.01165
0.17554	0.17890	0.01348
0.17554	0.19509	0.01551

17

0.20323	0.00000	0.00001

0.12654	0.04949	0.01193
0.12654	0.06590	0.01208
0.12654	0.06901	0.01209
0.12654	0.06916	0.01209
0.12654	0.06931	0.01209
0.12654	0.08225	0.01209
0.12654	0.09853	0.01207
0.12654	0.11472	0.01201
0.12654	0.13082	0.01189
0.12654	0.14682	0.01176
0.12654	0.16269	0.01164

15

0.14999	0.00000	0.01308
0.14999	0.01657	0.01352
0.14999	0.03312	0.01383
0.14999	0.04963	0.01403
0.14999	0.06608	0.01415
0.14999	0.06920	0.01416
0.14999	0.06935	0.01416
0.14999	0.06950	0.01416
0.14999	0.08248	0.01417
0.14999	0.09880	0.01412
0.14999	0.11503	0.01401
0.14999	0.13117	0.01389
0.14999	0.14720	0.01374
0.14999	0.16312	0.01359
0.14999	0.17890	0.01348

16

0.17554	0.00000	0.01539
0.17554	0.01663	0.01582
0.17554	0.03322	0.01612
0.17554	0.04978	0.01631
0.17554	0.06628	0.01639
0.17554	0.06941	0.01639
0.17554	0.06956	0.01639
0.17554	0.06971	0.01643
0.17554	0.08273	0.01642
0.17554	0.09909	0.01636
0.17554	0.11538	0.01624
0.17554	0.13156	0.01608
0.17554	0.14763	0.01589
0.17554	0.16359	0.01574
0.17554	0.17941	0.01560
0.17554	0.19509	0.01551

17

0.20323	0.00000	0.01791

0.20323	0.01629	0.00084	0.20323	0.01668	0.01833
0.20323	0.03258	0.00171	0.20323	0.03333	0.01863
0.20323	0.04887	0.00262	0.20323	0.04994	0.01881
0.20323	0.06515	0.00362	0.20323	0.06650	0.01890
0.20323	0.06824	0.00382	0.20323	0.06964	0.01890
0.20323	0.06839	0.00383	0.20323	0.06979	0.01891
0.20323	0.06854	0.00384	0.20323	0.06994	0.01891
0.20323	0.08143	0.00466	0.20323	0.08300	0.01887
0.20323	0.09770	0.00581	0.20323	0.09942	0.01879
0.20323	0.11397	0.00709	0.20323	0.11575	0.01866
0.20323	0.13022	0.00848	0.20323	0.13198	0.01849
0.20323	0.14647	0.00999	0.20323	0.14810	0.01828
0.20323	0.16269	0.01165	0.20323	0.16410	0.01808
0.20323	0.17890	0.01349	0.20323	0.17996	0.01791
0.20323	0.19509	0.01552	0.20323	0.19568	0.01779
0.20323	0.21124	0.01776	0.20323	0.21124	0.01776

18			18		
0.23308	0.00000	0.00001	0.23308	0.00000	0.02064
0.23308	0.01629	0.00084	0.23308	0.01674	0.02106
0.23308	0.03258	0.00171	0.23308	0.03345	0.02136
0.23308	0.04887	0.00262	0.23308	0.05012	0.02152
0.23308	0.06515	0.00362	0.23308	0.06674	0.02160
0.23308	0.06824	0.00382	0.23308	0.06989	0.02160
0.23308	0.06839	0.00383	0.23308	0.07004	0.02160
0.23308	0.06854	0.00384	0.23308	0.07019	0.02160
0.23308	0.08143	0.00468	0.23308	0.08330	0.02158
0.23308	0.09770	0.00584	0.23308	0.09977	0.02147
0.23308	0.11396	0.00708	0.23308	0.11615	0.02129
0.23308	0.13022	0.00848	0.23308	0.13244	0.02111
0.23308	0.14647	0.00998	0.23308	0.14861	0.02087
0.23308	0.16269	0.01165	0.23308	0.16466	0.02064
0.23308	0.17890	0.01348	0.23308	0.18056	0.02042
0.23308	0.19509	0.01552	0.23308	0.19633	0.02028
0.23308	0.21125	0.01776	0.23308	0.21193	0.02021
0.23308	0.22737	0.02023	0.23308	0.22737	0.02023

19			19		
0.26514	0.00000	0.00001	0.26514	0.00000	0.02360
0.26514	0.01629	0.00084	0.26514	0.01681	0.02402
0.26514	0.03258	0.00171	0.26514	0.03359	0.02431
0.26514	0.04887	0.00263	0.26514	0.05032	0.02447
0.26514	0.06515	0.00360	0.26514	0.06700	0.02451
0.26514	0.06824	0.00379	0.26514	0.07016	0.02450
0.26514	0.06839	0.00380	0.26514	0.07031	0.02450
0.26514	0.06854	0.00381	0.26514	0.07046	0.02450
0.26514	0.08143	0.00469	0.26514	0.08362	0.02449
0.26514	0.09770	0.00584	0.26514	0.10015	0.02436
0.26514	0.11397	0.00710	0.26514	0.11660	0.02418

0.26514	0.13022	0.00848	0.26514	0.13294	0.02395
0.26514	0.14646	0.00998	0.26514	0.14917	0.02368
0.26514	0.16269	0.01165	0.26514	0.16526	0.02342
0.26514	0.17890	0.01349	0.26514	0.18123	0.02318
0.26514	0.19508	0.01549	0.26514	0.19703	0.02296
0.26514	0.21125	0.01777	0.26514	0.21268	0.02287
0.26514	0.22737	0.02024	0.26514	0.22816	0.02285
0.26514	0.24345	0.02297	0.26514	0.24345	0.02297
20			20		
0.29940	0.00000	0.00000	0.29940	0.00000	0.02681
0.29940	0.01629	0.00083	0.29940	0.01688	0.02722
0.29940	0.03258	0.00171	0.29940	0.03373	0.02750
0.29940	0.04887	0.00263	0.29940	0.05053	0.02765
0.29940	0.06515	0.00361	0.29940	0.06728	0.02769
0.29940	0.06824	0.00381	0.29940	0.07045	0.02768
0.29940	0.06839	0.00382	0.29940	0.07060	0.02768
0.29940	0.06854	0.00383	0.29940	0.07076	0.02768
0.29940	0.08143	0.00469	0.29940	0.08397	0.02763
0.29940	0.09770	0.00583	0.29940	0.10057	0.02748
0.29940	0.11397	0.00710	0.29940	0.11708	0.02728
0.29940	0.13022	0.00847	0.29940	0.13348	0.02701
0.29940	0.14647	0.00999	0.29940	0.14976	0.02672
0.29940	0.16269	0.01166	0.29940	0.16591	0.02639
0.29940	0.17890	0.01350	0.29940	0.18194	0.02615
0.29940	0.19509	0.01553	0.29940	0.19780	0.02591
0.29940	0.21125	0.01777	0.29940	0.21349	0.02575
0.29940	0.22737	0.02025	0.29940	0.22901	0.02568
0.29940	0.24345	0.02298	0.29940	0.24435	0.02575
0.29940	0.25948	0.02598	0.29940	0.25948	0.02598
22			22		
0.33590	0.00000	-0.00001	0.33590	0.00000	0.03057
0.33590	0.01629	0.00082	0.33590	0.01695	0.03065
0.33590	0.03258	0.00171	0.33590	0.03388	0.03093
0.33590	0.04887	0.00263	0.33590	0.05076	0.03107
0.33590	0.06515	0.00361	0.33590	0.06758	0.03109
0.33590	0.06824	0.00381	0.33590	0.07077	0.03108
0.33590	0.06839	0.00382	0.33590	0.07092	0.03108
0.33590	0.06854	0.00383	0.33590	0.07107	0.03108
0.33590	0.08143	0.00469	0.33590	0.08434	0.03102
0.33590	0.09770	0.00584	0.33590	0.10101	0.03085
0.33590	0.11397	0.00710	0.33590	0.11759	0.03061
0.33590	0.13022	0.00846	0.33590	0.13406	0.03031
0.33590	0.14647	0.00999	0.33590	0.15041	0.03000
0.33590	0.16269	0.01166	0.33590	0.16663	0.02966
0.33590	0.17890	0.01349	0.33590	0.18270	0.02934
0.33590	0.19509	0.01551	0.33590	0.19861	0.02904
0.33590	0.21125	0.01776	0.33590	0.21436	0.02884

0.33590	0.22737	0.02024
0.33590	0.24344	0.02295
0.33590	0.25949	0.02599
0.33590	0.27376	0.02892
0.33590	0.27546	0.02929

0.33590	0.22993	0.02873
0.33590	0.24530	0.02872
0.33590	0.26049	0.02893
0.33590	0.27388	0.02924
0.33590	0.27546	0.02929

23

0.37461	0.00000	0.00001
0.37461	0.01629	0.00083
0.37461	0.03258	0.00170
0.37461	0.04887	0.00263
0.37461	0.06515	0.00362
0.37461	0.06824	0.00379
0.37461	0.06839	0.00380
0.37461	0.06854	0.00381
0.37461	0.08143	0.00467
0.37461	0.09770	0.00584
0.37461	0.11397	0.00709
0.37461	0.13022	0.00848
0.37461	0.14647	0.00999
0.37461	0.16269	0.01164
0.37461	0.17890	0.01349
0.37461	0.19509	0.01552
0.37461	0.21124	0.01775
0.37461	0.22737	0.02024
0.37461	0.24345	0.02297
0.37461	0.25948	0.02597
0.37461	0.27377	0.02894
0.37461	0.27546	0.02930
0.37461	0.29136	0.03293

23

0.37461	0.00000	0.03750
0.37461	0.01711	0.03750
0.37461	0.03417	0.03750
0.37461	0.05119	0.03750
0.37461	0.06815	0.03750
0.37461	0.07136	0.03750
0.37461	0.07126	0.03471
0.37461	0.07141	0.03471
0.37461	0.08474	0.03463
0.37461	0.10149	0.03445
0.37461	0.11814	0.03418
0.37461	0.13468	0.03386
0.37461	0.15110	0.03350
0.37461	0.16738	0.03312
0.37461	0.18352	0.03276
0.37461	0.19950	0.03244
0.37461	0.21530	0.03216
0.37461	0.23092	0.03201
0.37461	0.24635	0.03197
0.37461	0.26157	0.03207
0.37461	0.27500	0.03236
0.37461	0.27658	0.03240
0.37461	0.29136	0.03293

24

0.41557	0.00000	0.00002
0.41557	0.01629	0.00084
0.41557	0.03258	0.00170
0.41557	0.04887	0.00263
0.41557	0.06515	0.00362
0.41557	0.06824	0.00382
0.41557	0.06839	0.00383
0.41557	0.06854	0.00384
0.41557	0.08143	0.00468
0.41557	0.09770	0.00584
0.41557	0.11396	0.00707
0.41557	0.13022	0.00848
0.41557	0.14646	0.00998
0.41557	0.16269	0.01165
0.41557	0.17890	0.01350
0.41557	0.19509	0.01553
0.41557	0.21125	0.01777

24

0.41557	0.00000	0.04483
0.41557	0.01727	0.04483
0.41557	0.03450	0.04483
0.41557	0.05167	0.04483
0.41557	0.06880	0.04483
0.41557	0.07204	0.04482
0.41557	0.07162	0.03862
0.41557	0.07178	0.03862
0.41557	0.08517	0.03852
0.41557	0.10200	0.03830
0.41557	0.11873	0.03799
0.41557	0.13534	0.03762
0.41557	0.15184	0.03725
0.41557	0.16820	0.03684
0.41557	0.18440	0.03644
0.41557	0.20045	0.03607
0.41557	0.21631	0.03576

0.41557	0.22737	0.02025	0.41557	0.23199	0.03554
0.41557	0.24345	0.02298	0.41557	0.24747	0.03544
0.41557	0.25948	0.02599	0.41557	0.26273	0.03549
0.41557	0.27377	0.02893	0.41557	0.27620	0.03569
0.41557	0.27545	0.02929	0.41557	0.27778	0.03572
0.41557	0.29136	0.03294	0.41557	0.29260	0.03620
0.41557	0.30718	0.03691	0.41557	0.30718	0.03691
25			25		
0.45874	0.00000	0.00001	0.45874	0.00000	0.05255
0.45874	0.01629	0.00084	0.45874	0.01744	0.05255
0.45874	0.03258	0.00171	0.45874	0.03484	0.05255
0.45874	0.04887	0.00263	0.45874	0.05219	0.05255
0.45874	0.06515	0.00360	0.45874	0.06948	0.05255
0.45874	0.06824	0.00379	0.45874	0.07275	0.05255
0.45874	0.06839	0.00380	0.45874	0.07200	0.04274
0.45874	0.06854	0.00381	0.45874	0.07216	0.04274
0.45874	0.08143	0.00469	0.45874	0.08562	0.04265
0.45874	0.09770	0.00583	0.45874	0.10254	0.04240
0.45874	0.11397	0.00710	0.45874	0.11936	0.04208
0.45874	0.13022	0.00847	0.45874	0.13606	0.04168
0.45874	0.14646	0.00996	0.45874	0.15263	0.04123
0.45874	0.16269	0.01166	0.45874	0.16906	0.04081
0.45874	0.17890	0.01349	0.45874	0.18534	0.04035
0.45874	0.19509	0.01552	0.45874	0.20145	0.03993
0.45874	0.21125	0.01776	0.45874	0.21738	0.03956
0.45874	0.22737	0.02024	0.45874	0.23312	0.03928
0.45874	0.24345	0.02298	0.45874	0.24866	0.03913
0.45874	0.25947	0.02596	0.45874	0.26397	0.03910
0.45874	0.27377	0.02894	0.45874	0.27748	0.03927
0.45874	0.27546	0.02930	0.45874	0.27907	0.03930
0.45874	0.29136	0.03293	0.45874	0.29393	0.03968
0.45874	0.30717	0.03690	0.45874	0.30854	0.04032
0.45874	0.32290	0.04126	0.45874	0.32290	0.04126
26			26		
0.50409	0.00000	0.00000	0.50409	0.00000	0.06066
0.50409	0.01629	0.00083	0.50409	0.01762	0.06066
0.50409	0.03258	0.00171	0.50409	0.03520	0.06066
0.50409	0.04887	0.00264	0.50409	0.05273	0.06066
0.50409	0.06515	0.00362	0.50409	0.07020	0.06066
0.50409	0.06824	0.00381	0.50409	0.07351	0.06066
0.50409	0.06839	0.00382	0.50409	0.07241	0.04716
0.50409	0.06854	0.00383	0.50409	0.07257	0.04716
0.50409	0.08143	0.00469	0.50409	0.08611	0.04703
0.50409	0.09770	0.00584	0.50409	0.10311	0.04673
0.50409	0.11396	0.00708	0.50409	0.12002	0.04638
0.50409	0.13022	0.00848	0.50409	0.13681	0.04598
0.50409	0.14647	0.00999	0.50409	0.15347	0.04551

0.50409	0.16269	0.01165
0.50409	0.17890	0.01347
0.50409	0.19509	0.01553
0.50409	0.21125	0.01777
0.50409	0.22737	0.02025
0.50409	0.24345	0.02298
0.50409	0.25948	0.02599
0.50409	0.27377	0.02893
0.50409	0.27545	0.02929
0.50409	0.29136	0.03294
0.50409	0.30718	0.03692
0.50409	0.32290	0.04125
0.50409	0.33851	0.04599

27

0.53104	0.00000	0.00001
0.53104	0.01629	0.00084
0.53104	0.03258	0.00171
0.53104	0.04887	0.00263
0.53104	0.06515	0.00362
0.53104	0.06824	0.00381
0.53104	0.06839	0.00382
0.53104	0.06854	0.00383
0.53104	0.08143	0.00469
0.53104	0.09770	0.00583
0.53104	0.11397	0.00710
0.53104	0.13022	0.00847
0.53104	0.14647	0.00999
0.53104	0.16269	0.01166
0.53104	0.17890	0.01349
0.53104	0.19509	0.01551
0.53104	0.21125	0.01777
0.53104	0.22737	0.02024
0.53104	0.24345	0.02296
0.53104	0.25948	0.02598
0.53104	0.27377	0.02893
0.53104	0.27546	0.02930
0.53104	0.29136	0.03294
0.53104	0.30718	0.03691
0.53104	0.32289	0.04125
0.53104	0.33851	0.04599
0.53104	0.34740	0.04888

28

0.55158	0.00000	0.00002
0.55158	0.01629	0.00084
0.55158	0.03258	0.00170
0.55158	0.04887	0.00263
0.55158	0.06515	0.00363

0.50409	0.16998	0.04500
0.50409	0.18634	0.04450
0.50409	0.20252	0.04404
0.50409	0.21853	0.04363
0.50409	0.23432	0.04326
0.50409	0.24993	0.04307
0.50409	0.26530	0.04299
0.50409	0.27885	0.04307
0.50409	0.28044	0.04309
0.50409	0.29535	0.04342
0.50409	0.31000	0.04398
0.50409	0.32439	0.04482
0.50409	0.33851	0.04599

27

0.53104	0.00000	0.06549
0.53104	0.01773	0.06549
0.53104	0.03541	0.06549
0.53104	0.05305	0.06549
0.53104	0.07063	0.06548
0.53104	0.07395	0.06548
0.53104	0.07266	0.04980
0.53104	0.07282	0.04980
0.53104	0.08640	0.04966
0.53104	0.10346	0.04936
0.53104	0.12042	0.04900
0.53104	0.13726	0.04854
0.53104	0.15397	0.04806
0.53104	0.17054	0.04753
0.53104	0.18694	0.04700
0.53104	0.20316	0.04649
0.53104	0.21921	0.04606
0.53104	0.23505	0.04569
0.53104	0.25068	0.04542
0.53104	0.26609	0.04531
0.53104	0.27967	0.04537
0.53104	0.28127	0.04539
0.53104	0.29620	0.04566
0.53104	0.31087	0.04618
0.53104	0.32528	0.04696
0.53104	0.33942	0.04809
0.53104	0.34740	0.04888

28

0.55158	0.00000	0.07181
0.55158	0.01787	0.07181
0.55158	0.03569	0.07181
0.55158	0.05347	0.07181
0.55158	0.07119	0.07181

0.55158	0.06824	0.00382
0.55158	0.06839	0.00383
0.55158	0.06854	0.00384
0.55158	0.08143	0.00468
0.55158	0.09770	0.00584
0.55158	0.11397	0.00710
0.55158	0.13022	0.00848
0.55158	0.14646	0.00998
0.55158	0.16269	0.01166
0.55158	0.17890	0.01350
0.55158	0.19509	0.01553
0.55158	0.21124	0.01775
0.55158	0.22737	0.02024
0.55158	0.24345	0.02298
0.55158	0.25949	0.02599
0.55158	0.27377	0.02894
0.55158	0.27546	0.02931
0.55158	0.29135	0.03292
0.55158	0.30717	0.03689
0.55158	0.32290	0.04127
0.55158	0.33851	0.04598
0.55158	0.34739	0.04886
0.55158	0.35399	0.05112

0.55158	0.07454	0.07181
0.55158	0.07285	0.05183
0.55158	0.07300	0.05182
0.55158	0.08662	0.05166
0.55158	0.10373	0.05137
0.55158	0.12073	0.05098
0.55158	0.13761	0.05052
0.55158	0.15436	0.05002
0.55158	0.17096	0.04947
0.55158	0.18740	0.04892
0.55158	0.20366	0.04840
0.55158	0.21973	0.04790
0.55158	0.23561	0.04753
0.55158	0.25127	0.04724
0.55158	0.26670	0.04707
0.55158	0.28031	0.04713
0.55158	0.28191	0.04714
0.55158	0.29685	0.04737
0.55158	0.31154	0.04784
0.55158	0.32596	0.04860
0.55158	0.34012	0.04970
0.55158	0.34810	0.05045
0.55158	0.35399	0.05112

29

0.60117	0.00000	0.00002
0.60117	0.01629	0.00084
0.60117	0.03258	0.00171
0.60117	0.04887	0.00263
0.60117	0.06515	0.00362
0.60117	0.06824	0.00382
0.60117	0.06839	0.00383
0.60117	0.06854	0.00384
0.60117	0.08143	0.00469
0.60117	0.09770	0.00583
0.60117	0.11397	0.00711
0.60117	0.13022	0.00847
0.60117	0.14647	0.00999
0.60117	0.16269	0.01166
0.60117	0.17890	0.01349
0.60117	0.19509	0.01552
0.60117	0.21125	0.01777
0.60117	0.22736	0.02021
0.60117	0.24345	0.02298
0.60117	0.25948	0.02599
0.60117	0.27376	0.02892
0.60117	0.27546	0.02930
0.60117	0.29136	0.03294
0.60117	0.30717	0.03691

29

0.60117	0.00000	0.08710
0.60117	0.01821	0.08710
0.60117	0.03637	0.08710
0.60117	0.05448	0.08710
0.60117	0.07254	0.08710
0.60117	0.07596	0.08710
0.60117	0.07330	0.05674
0.60117	0.07346	0.05673
0.60117	0.08716	0.05656
0.60117	0.10437	0.05622
0.60117	0.12147	0.05581
0.60117	0.13845	0.05530
0.60117	0.15529	0.05476
0.60117	0.17199	0.05417
0.60117	0.18851	0.05356
0.60117	0.20486	0.05300
0.60117	0.22101	0.05247
0.60117	0.23695	0.05198
0.60117	0.25269	0.05166
0.60117	0.26819	0.05145
0.60117	0.28184	0.05140
0.60117	0.28345	0.05141
0.60117	0.29845	0.05158
0.60117	0.31319	0.05198

0.60117	0.32290	0.04126
0.60117	0.33850	0.04597
0.60117	0.34740	0.04887
0.60117	0.35399	0.05112
0.60117	0.36933	0.05667

0.60117	0.32766	0.05267
0.60117	0.34183	0.05363
0.60117	0.34984	0.05436
0.60117	0.35573	0.05497
0.60117	0.36933	0.05667

30

0.65278	0.00000	-0.00001
0.65278	0.01629	0.00084
0.65278	0.03258	0.00171
0.65278	0.04887	0.00264
0.65278	0.06515	0.00362
0.65278	0.06824	0.00381
0.65278	0.06839	0.00382
0.65278	0.06854	0.00383
0.65278	0.08143	0.00469
0.65278	0.09770	0.00585
0.65278	0.11397	0.00710
0.65278	0.13022	0.00848
0.65278	0.14646	0.00996
0.65278	0.16269	0.01165
0.65278	0.17890	0.01350
0.65278	0.19509	0.01553
0.65278	0.21124	0.01774
0.65278	0.22737	0.02025
0.65278	0.24345	0.02298
0.65278	0.25949	0.02599
0.65278	0.27377	0.02894
0.65278	0.27546	0.02931
0.65278	0.29135	0.03291
0.65278	0.30718	0.03692
0.65278	0.32289	0.04125
0.65278	0.33851	0.04599
0.65278	0.34740	0.04888
0.65278	0.35399	0.05111
0.65278	0.36933	0.05667
0.65278	0.38451	0.06264

30

0.65278	0.00000	0.10925
0.65278	0.01870	0.10925
0.65278	0.03735	0.10925
0.65278	0.05595	0.10925
0.65278	0.07450	0.10925
0.65278	0.07801	0.10925
0.65278	0.07818	0.10925
0.65278	0.07828	0.06183
0.65278	0.08773	0.06170
0.65278	0.10505	0.06135
0.65278	0.12225	0.06089
0.65278	0.13933	0.06032
0.65278	0.15627	0.05973
0.65278	0.17307	0.05912
0.65278	0.18969	0.05848
0.65278	0.20612	0.05785
0.65278	0.22235	0.05723
0.65278	0.23839	0.05673
0.65278	0.25419	0.05632
0.65278	0.26975	0.05601
0.65278	0.28347	0.05593
0.65278	0.28508	0.05593
0.65278	0.30013	0.05599
0.65278	0.31493	0.05634
0.65278	0.32943	0.05692
0.65278	0.34366	0.05783
0.65278	0.35167	0.05849
0.65278	0.35757	0.05905
0.65278	0.37120	0.06065
0.65278	0.38451	0.06264

32

0.70633	0.00000	0.00002
0.70633	0.01629	0.00083
0.70633	0.03258	0.00169
0.70633	0.04887	0.00263
0.70633	0.06515	0.00363
0.70633	0.06824	0.00382
0.70633	0.06839	0.00383
0.70633	0.06854	0.00384
0.70633	0.08143	0.00467
0.70633	0.09770	0.00585

32

0.70633	0.00000	0.10925
0.70633	0.01870	0.10925
0.70633	0.03735	0.10925
0.70633	0.05595	0.10925
0.70633	0.07450	0.10925
0.70633	0.07801	0.10925
0.70633	0.07818	0.10925
0.70633	0.07828	0.06724
0.70633	0.08832	0.06707
0.70633	0.10575	0.06667

0.70633	0.11397	0.00710
0.70633	0.13022	0.00848
0.70633	0.14647	0.00999
0.70633	0.16270	0.01166
0.70633	0.17890	0.01347
0.70633	0.19509	0.01552
0.70633	0.21125	0.01777
0.70633	0.22736	0.02022
0.70633	0.24345	0.02298
0.70633	0.25949	0.02599
0.70633	0.27376	0.02892
0.70633	0.27546	0.02930
0.70633	0.29136	0.03294
0.70633	0.30717	0.03690
0.70633	0.32290	0.04126
0.70633	0.33850	0.04597
0.70633	0.34740	0.04888
0.70633	0.35400	0.05113
0.70633	0.36933	0.05666
0.70633	0.38451	0.06264
0.70633	0.38642	0.06343
0.70633	0.39951	0.06906

0.70633	0.12307	0.06621
0.70633	0.14027	0.06564
0.70633	0.15731	0.06500
0.70633	0.17420	0.06432
0.70633	0.19091	0.06360
0.70633	0.20745	0.06292
0.70633	0.22377	0.06228
0.70633	0.23988	0.06166
0.70633	0.25577	0.06121
0.70633	0.27141	0.06086
0.70633	0.28517	0.06066
0.70633	0.28679	0.06066
0.70633	0.30192	0.06068
0.70633	0.31675	0.06091
0.70633	0.33131	0.06143
0.70633	0.34557	0.06222
0.70633	0.35361	0.06285
0.70633	0.35953	0.06338
0.70633	0.37317	0.06486
0.70633	0.38650	0.06676
0.70633	0.38817	0.06702
0.70633	0.39951	0.06906

33

0.76178	0.00000	0.00002
0.76178	0.01629	0.00085
0.76178	0.03258	0.00171
0.76178	0.04887	0.00262
0.76178	0.06515	0.00362
0.76178	0.06824	0.00382
0.76178	0.06839	0.00383
0.76178	0.06854	0.00384
0.76178	0.08143	0.00469
0.76178	0.09770	0.00583
0.76178	0.11397	0.00711
0.76178	0.13022	0.00846
0.76178	0.14647	0.01000
0.76178	0.16269	0.01165
0.76178	0.17890	0.01350
0.76178	0.19509	0.01553
0.76178	0.21125	0.01777
0.76178	0.22737	0.02025
0.76178	0.24345	0.02298
0.76178	0.25947	0.02596
0.76178	0.27377	0.02894
0.76178	0.27546	0.02931
0.76178	0.29136	0.03294
0.76178	0.30718	0.03692
0.76178	0.32290	0.04126

33

0.76178	0.00000	0.10925
0.76178	0.01870	0.10925
0.76178	0.03735	0.10925
0.76178	0.05595	0.10925
0.76178	0.07450	0.10925
0.76178	0.07801	0.10925
0.76178	0.07818	0.10925
0.76178	0.07828	0.07290
0.76178	0.08894	0.07273
0.76178	0.10649	0.07230
0.76178	0.12393	0.07179
0.76178	0.14124	0.07116
0.76178	0.15840	0.07049
0.76178	0.17539	0.06975
0.76178	0.19221	0.06900
0.76178	0.20884	0.06826
0.76178	0.22526	0.06754
0.76178	0.24145	0.06688
0.76178	0.25742	0.06634
0.76178	0.27313	0.06588
0.76178	0.28697	0.06567
0.76178	0.28859	0.06564
0.76178	0.30378	0.06557
0.76178	0.31868	0.06574
0.76178	0.33328	0.06615

0.76178	0.33851	0.04598
0.76178	0.34740	0.04887
0.76178	0.35400	0.05113
0.76178	0.36934	0.05668
0.76178	0.38451	0.06264
0.76178	0.38642	0.06342
0.76178	0.39951	0.06906
0.76178	0.41431	0.07592

34

0.81896	0.00000	0.00000
0.81896	0.01629	0.00083
0.81896	0.03258	0.00172
0.81896	0.04887	0.00264
0.81896	0.06515	0.00360
0.81896	0.06824	0.00381
0.81896	0.06839	0.00382
0.81896	0.06854	0.00383
0.81896	0.08143	0.00465
0.81896	0.09770	0.00585
0.81896	0.11397	0.00709
0.81896	0.13022	0.00849
0.81896	0.14647	0.00999
0.81896	0.16269	0.01166
0.81896	0.17890	0.01350
0.81896	0.19509	0.01552
0.81896	0.21125	0.01776
0.81896	0.22736	0.02022
0.81896	0.24345	0.02298
0.81896	0.25949	0.02599
0.81896	0.27376	0.02891
0.81896	0.27545	0.02928
0.81896	0.29136	0.03293
0.81896	0.30718	0.03692
0.81896	0.32289	0.04124
0.81896	0.33851	0.04599
0.81896	0.34740	0.04889
0.81896	0.35399	0.05110
0.81896	0.36933	0.05667
0.81896	0.38450	0.06262
0.81896	0.38643	0.06344
0.81896	0.39950	0.06905
0.81896	0.41431	0.07593
0.81896	0.42889	0.08323

35

0.84998	0.00000	0.00001
0.84998	0.01629	0.00084
0.84998	0.03258	0.00171

0.76178	0.34758	0.06685
0.76178	0.35564	0.06742
0.76178	0.36158	0.06792
0.76178	0.37524	0.06929
0.76178	0.38860	0.07109
0.76178	0.39026	0.07134
0.76178	0.40162	0.07329
0.76178	0.41431	0.07592

34

0.81896	0.00000	0.10925
0.81896	0.01870	0.10925
0.81896	0.03735	0.10925
0.81896	0.05595	0.10925
0.81896	0.07450	0.10925
0.81896	0.07801	0.10925
0.81896	0.07818	0.10925
0.81896	0.07828	0.07884
0.81896	0.08959	0.07862
0.81896	0.10727	0.07815
0.81896	0.12483	0.07762
0.81896	0.14225	0.07694
0.81896	0.15952	0.07620
0.81896	0.17663	0.07542
0.81896	0.19356	0.07463
0.81896	0.21029	0.07382
0.81896	0.22681	0.07305
0.81896	0.24310	0.07235
0.81896	0.25914	0.07169
0.81896	0.27494	0.07119
0.81896	0.28884	0.07087
0.81896	0.29049	0.07088
0.81896	0.30574	0.07073
0.81896	0.32070	0.07079
0.81896	0.33535	0.07111
0.81896	0.34972	0.07177
0.81896	0.35778	0.07224
0.81896	0.36374	0.07270
0.81896	0.37744	0.07400
0.81896	0.39081	0.07568
0.81896	0.39248	0.07591
0.81896	0.40385	0.07778
0.81896	0.41655	0.08030
0.81896	0.42889	0.08323

35

0.84998	0.00000	0.10925
0.84998	0.01870	0.10925
0.84998	0.03735	0.10925

0.84998	0.04887	0.00262
0.84998	0.06515	0.00362
0.84998	0.06824	0.00382
0.84998	0.06839	0.00383
0.84998	0.06854	0.00384
0.84998	0.08143	0.00470
0.84998	0.09770	0.00582
0.84998	0.11397	0.00711
0.84998	0.13022	0.00848
0.84998	0.14647	0.01000
0.84998	0.16269	0.01165
0.84998	0.17890	0.01350
0.84998	0.19509	0.01553
0.84998	0.21125	0.01777
0.84998	0.22737	0.02024
0.84998	0.24345	0.02297
0.84998	0.25948	0.02598
0.84998	0.27377	0.02893
0.84998	0.27546	0.02930
0.84998	0.29135	0.03291
0.84998	0.30717	0.03690
0.84998	0.32290	0.04125
0.84998	0.33851	0.04599
0.84998	0.34740	0.04888
0.84998	0.35399	0.05110
0.84998	0.36934	0.05667
0.84998	0.38451	0.06264
0.84998	0.38643	0.06344
0.84998	0.39950	0.06904
0.84998	0.41431	0.07593
0.84998	0.42889	0.08323
0.84998	0.43654	0.08728

0.84998	0.05595	0.10925
0.84998	0.07450	0.10925
0.84998	0.07801	0.10925
0.84998	0.07818	0.10925
0.84998	0.07828	0.08202
0.84998	0.08995	0.08180
0.84998	0.10769	0.08133
0.84998	0.12530	0.08070
0.84998	0.14279	0.08001
0.84998	0.16013	0.07928
0.84998	0.17729	0.07846
0.84998	0.19429	0.07767
0.84998	0.21106	0.07680
0.84998	0.22764	0.07600
0.84998	0.24398	0.07527
0.84998	0.26008	0.07460
0.84998	0.27592	0.07406
0.84998	0.28986	0.07371
0.84998	0.29150	0.07368
0.84998	0.30679	0.07348
0.84998	0.32179	0.07352
0.84998	0.33648	0.07381
0.84998	0.35085	0.07439
0.84998	0.35895	0.07486
0.84998	0.36491	0.07529
0.84998	0.37863	0.07654
0.84998	0.39202	0.07817
0.84998	0.39369	0.07840
0.84998	0.40506	0.08020
0.84998	0.41776	0.08266
0.84998	0.43012	0.08556
0.84998	0.43654	0.08728

36

0.87780	0.00000	0.00001
0.87780	0.01629	0.00083
0.87780	0.03258	0.00169
0.87780	0.04887	0.00263
0.87780	0.06515	0.00363
0.87780	0.06824	0.00382
0.87780	0.06839	0.00383
0.87780	0.06854	0.00384
0.87780	0.08143	0.00468
0.87780	0.09770	0.00585
0.87780	0.11397	0.00711
0.87780	0.13022	0.00845
0.87780	0.14647	0.00999
0.87780	0.16270	0.01166
0.87780	0.17890	0.01348

36

0.87780	0.00000	0.10925
0.87780	0.01870	0.10925
0.87780	0.03735	0.10925
0.87780	0.05595	0.10925
0.87780	0.07450	0.10925
0.87780	0.07801	0.10925
0.87780	0.07818	0.10925
0.87780	0.07828	0.07371
0.87780	0.08906	0.07377
0.87780	0.10668	0.07368
0.87780	0.12420	0.07350
0.87780	0.14161	0.07327
0.87780	0.15887	0.07292
0.87780	0.17600	0.07253
0.87780	0.19298	0.07221

0.87780	0.19509	0.01553
0.87780	0.21125	0.01778
0.87780	0.22737	0.02025
0.87780	0.24346	0.02298
0.87780	0.25949	0.02599
0.87780	0.27377	0.02894
0.87780	0.27546	0.02931
0.87780	0.29136	0.03294
0.87780	0.30717	0.03691
0.87780	0.32290	0.04126
0.87780	0.33851	0.04598
0.87780	0.34740	0.04889
0.87780	0.35399	0.05112
0.87780	0.36934	0.05668
0.87780	0.38451	0.06265
0.87780	0.38643	0.06344
0.87780	0.39950	0.06904
0.87780	0.41431	0.07593
0.87780	0.42890	0.08323
0.87780	0.43654	0.08729
0.87780	0.44325	0.09098

36

0.93164	0.00000	0.00002
0.93164	0.01629	0.00084
0.93164	0.03258	0.00171
0.93164	0.04887	0.00263
0.93164	0.06515	0.00363
0.93164	0.06824	0.00383
0.93164	0.06839	0.00384
0.93164	0.06854	0.00385
0.93164	0.08143	0.00469
0.93164	0.09770	0.00583
0.93164	0.11397	0.00711
0.93164	0.13022	0.00847
0.93164	0.14647	0.01000
0.93164	0.16269	0.01165
0.93164	0.17890	0.01350
0.93164	0.19509	0.01553
0.93164	0.21125	0.01777
0.93164	0.22737	0.02024
0.93164	0.24345	0.02298
0.93164	0.25949	0.02599
0.93164	0.27377	0.02893
0.93164	0.27546	0.02930
0.93164	0.29136	0.03293
0.93164	0.30718	0.03691
0.93164	0.32291	0.04127
0.93164	0.33852	0.04600

0.87780	0.20974	0.07173
0.87780	0.22633	0.07134
0.87780	0.24271	0.07103
0.87780	0.25886	0.07081
0.87780	0.27478	0.07070
0.87780	0.28880	0.07076
0.87780	0.29044	0.07075
0.87780	0.30584	0.07098
0.87780	0.32095	0.07142
0.87780	0.33573	0.07202
0.87780	0.35028	0.07308
0.87780	0.35844	0.07373
0.87780	0.36448	0.07433
0.87780	0.37837	0.07599
0.87780	0.39188	0.07789
0.87780	0.39356	0.07814
0.87780	0.40606	0.08221
0.87780	0.41863	0.08436
0.87780	0.43089	0.08703
0.87780	0.43728	0.08867
0.87780	0.44325	0.09098

36

0.93164	0.00000	0.10925
0.93164	0.01870	0.10925
0.93164	0.03735	0.10925
0.93164	0.05595	0.10925
0.93164	0.07450	0.10925
0.93164	0.07801	0.10925
0.93164	0.07818	0.10925
0.93164	0.07828	0.05684
0.93164	0.08723	0.05716
0.93164	0.10457	0.05778
0.93164	0.12184	0.05822
0.93164	0.13906	0.05875
0.93164	0.15616	0.05915
0.93164	0.17319	0.05970
0.93164	0.19008	0.06011
0.93164	0.20685	0.06063
0.93164	0.22350	0.06129
0.93164	0.23998	0.06199
0.93164	0.25628	0.06281
0.93164	0.27242	0.06382
0.93164	0.28666	0.06482
0.93164	0.28835	0.06496
0.93164	0.30406	0.06632
0.93164	0.31957	0.06796
0.93164	0.33484	0.06987
0.93164	0.34986	0.07209

0.93164	0.34740	0.04887
0.93164	0.35400	0.05113
0.93164	0.36933	0.05666
0.93164	0.38451	0.06265
0.93164	0.38642	0.06341
0.93164	0.39951	0.06906
0.93164	0.41431	0.07593
0.93164	0.42890	0.08323
0.93164	0.43654	0.08729
0.93164	0.44325	0.09098
0.93816	0.45582	0.09828

38

1.00000	0.00000	0.00001
1.00000	0.01629	0.00083
1.00000	0.03258	0.00170
1.00000	0.04887	0.00263
1.00000	0.06515	0.00362
1.00000	0.06824	0.00381
1.00000	0.06839	0.00382
1.00000	0.06854	0.00383
1.00000	0.08143	0.00468
1.00000	0.09770	0.00584
1.00000	0.11397	0.00710
1.00000	0.13022	0.00847
1.00000	0.14647	0.00999
1.00000	0.16269	0.01165
1.00000	0.17890	0.01349
1.00000	0.19509	0.01552
1.00000	0.21125	0.01777
1.00000	0.22737	0.02024
1.00000	0.24345	0.02298
1.00000	0.25949	0.02599
1.00000	0.27377	0.02894
1.00000	0.27546	0.02930
1.00000	0.29136	0.03294
1.00000	0.30718	0.03692
1.00000	0.32290	0.04127
1.00000	0.33851	0.04600
1.00000	0.34740	0.04889
1.00000	0.35400	0.05113
1.00000	0.36934	0.05668
1.00000	0.38452	0.06265
1.00000	0.38643	0.06344
1.00000	0.39951	0.06907
1.00000	0.41431	0.07593
1.00000	0.42890	0.08323
1.00000	0.43654	0.08729
1.00000	0.44325	0.09099

0.93164	0.35835	0.07352
0.93164	0.36458	0.07456
0.93164	0.37909	0.07753
0.93164	0.39323	0.08068
0.93164	0.39505	0.08121
0.93164	0.40798	0.08607
0.93164	0.42031	0.08764
0.93164	0.43239	0.08988
0.93164	0.43870	0.09135
0.93164	0.44446	0.09322
0.93164	0.45582	0.09828

38

1.00000	0.00000	0.03000
1.00000	0.01694	0.03000
1.00000	0.03384	0.03000
1.00000	0.05069	0.03000
1.00000	0.06749	0.03000
1.00000	0.07067	0.03000
1.00000	0.07116	0.03371
1.00000	0.07132	0.03372
1.00000	0.08473	0.03452
1.00000	0.10164	0.03560
1.00000	0.11854	0.03676
1.00000	0.13542	0.03803
1.00000	0.15227	0.03943
1.00000	0.16910	0.04097
1.00000	0.18590	0.04268
1.00000	0.20266	0.04457
1.00000	0.21938	0.04665
1.00000	0.23605	0.04897
1.00000	0.25265	0.05154
1.00000	0.26920	0.05438
1.00000	0.28392	0.05717
1.00000	0.28566	0.05752
1.00000	0.30203	0.06098
1.00000	0.31830	0.06479
1.00000	0.33445	0.06895
1.00000	0.35047	0.07351
1.00000	0.35959	0.07630
1.00000	0.36634	0.07847
1.00000	0.38205	0.08384
1.00000	0.39757	0.08966
1.00000	0.39952	0.09042
1.00000	0.41045	0.09102
1.00000	0.42245	0.09180
1.00000	0.43429	0.09349
1.00000	0.44052	0.09475
1.00000	0.44599	0.09608

1.00000	0.45736	0.09918
1.00000	0.47120	0.10780

14

1.01500	0.00000	0.01500
1.01500	0.01694	0.01541
1.01500	0.03258	0.01585
1.01500	0.07000	0.01692
1.01500	0.10000	0.02070
1.01500	0.13250	0.02330
1.01500	0.18500	0.02859
1.01500	0.25500	0.03876
1.01500	0.30400	0.04895
1.01500	0.32290	0.05407
1.01500	0.38300	0.07324
1.01500	0.42600	0.08751
1.01500	0.44450	0.09353
1.01500	0.47120	0.10780

1.00000	0.45756	0.09954
1.00000	0.47120	0.10780

14

1.01500	0.00000	0.01500
1.01500	0.01694	0.01541
1.01500	0.03258	0.01585
1.01500	0.07000	0.01692
1.01500	0.10000	0.02070
1.01500	0.13250	0.02330
1.01500	0.18500	0.02859
1.01500	0.25500	0.03876
1.01500	0.30400	0.04895
1.01500	0.32290	0.05407
1.01500	0.38300	0.07324
1.01500	0.42600	0.08751
1.01500	0.44450	0.09353
1.01500	0.47120	0.10780

APPENDIX B. SAMPLE INPUT FILES

Mach 3.0 (Inviscid) Input file, Start

```
$GLOBAL
     CHIMRA= .F.,   NSTEPS=200,   RESTRT= .F.,   NSAVE =10,
     NQT   = 0,
     $END
 $FLOINP
     ALPHA = 0,  FSMACH = 0.3,  REY   = 3.19E6,  TINF  =
520.000,
     $END
 $VARGAM
     $END
 $GRDNAM
     NAME = 'Waverider Half-Body, 42x45x50 grid',
 $END
 $NITERS
     $END
 $METPRM
     IRHS  = 0,   ILHS  = 2,   IDISS  = 2,
     $END
 $TIMACU
     DT    = 0.01, ITIME= 1,  TFOSO = 1.00, CFLMIN=0.0,
     $END
 $SMOACU
     ISPECJ= 2,  DIS2J = 0.0,  DIS4J = 0.2,
     ISPECK= 2,  DIS2K = 0.0,  DIS4K = 0.2,
     ISPECL= 2,  DIS2L = 0.0,  DIS4L = 0.2,
     SMOO  = 1.00,
     EPSE  = 0.35,
     $END
 $VISINP
     VISCJ = .F.,  VISCK = .F.,  VISCL = .F.,
     NTURB =   0,
     ITTYP =   1,
     ITDIR =   3,
     JTLS  =   1,
     JTLE  =  42,
     KTLS  =   1,
     KTLE  =  45,
     LTLS  =   1,
     LTLE  =  50,
     TLPAR1= 0.3,
     $END
```

```
$BCINP
    NBC    =   6,
    IBTYP =     1, 14,   12,   54,   12,  32,
    IBDIR =     3,  2,   -1,   -2,    1,  -3,
    JBCS  =     1,  1,   42,    1,    1,   1,
    JBCE  =    42, 42,   42,   42,    1,  42,
    KBCS  =     1,  1,    1,   45,    1,   1,
    KBCE  =    45,  1,   45,   45,   45,  45,
    LBCS  =     1,  1,    1,    1,    1,  50,
    LBCE  =     1, 49,   50,   50,   50,  50,
    $END
$SCEINP
$END
```

Mach 3.0 (Viscous) Input File, Restart

```
$GLOBAL
     CHIMRA= .F.,   NSTEPS=10000,   RESTRT= .T.,   NSAVE
=100, NQT   = 0,
     $END
 $FLOINP
     ALPHA = 0,  FSMACH = 0.3,  REY   = 3.19E6,  TINF  =
520.000,
     $END
 $VARGAM
     $END
 $GRDNAM
     NAME = 'Waverider Half-Body, 42x45x50 grid',
 $END
 $NITERS
     $END
 $METPRM
     IRHS  = 0,   ILHS  = 2,   IDISS  = 2,
     $END
 $TIMACU
     DT    = 0.07, ITIME= 1,  TFOSO = 1.00, CFLMIN=0.01,
     $END
 $SMOACU
     ISPECJ= 2,  DIS2J = 0.0,  DIS4J = 0.2,
     ISPECK= 2,  DIS2K = 0.0,  DIS4K = 0.2,
     ISPECL= 2,  DIS2L = 0.0,  DIS4L = 0.2,
     SMOO  = 1.00,
     EPSE  = 0.35,
     $END
 $VISINP
     VISCJ = .T.,  VISCK = .F.,  VISCL = .T.,
     NTURB =   1,
     ITTYP =   1,
     ITDIR =   3,
     JTLS  =   1,
     JTLE  =  42,
     KTLS  =   1,
     KTLE  =  45,
     LTLS  =   1,
     LTLE  =  50,
     TLPAR1= 0.3,
     $END
 $BCINP
     NBC   =   6,
```

```
    IBTYP =     5, 14,   12,   54,   12,  32,
    IBDIR =     3,  2,   -1,   -2,    1,  -3,
    JBCS  =     1,  1,   42,    1,    1,   1,
    JBCE  =    42, 42,   42,   42,    1,  42,
    KBCS  =     1,  1,    1,   45,    1,   1,
    KBCE  =    45,  1,   45,   45,   45,  45,
    LBCS  =     1,  1,    1,    1,    1,  50,
    LBCE  =     1, 49,   50,   50,   50,  50,
    $END
$SCEINP
$END
```

Mach 6.0 (Inviscid) Input file, Start

```
$GLOBAL
     CHIMRA= .F.,   NSTEPS=100,   RESTRT= .F.,   NSAVE =10,
     NQT    = 0,
     $END
 $FLOINP
     ALPHA = 0,  FSMACH = 6.0,  REY    = 6.39E7,  TINF   =
520.000,
     $END
 $VARGAM
     $END
 $GRDNAM
     NAME = 'Waverider Half-Body, 42x45x50 grid',
 $END
 $NITERS
     $END
 $METPRM
     IRHS   = 0,   ILHS   = 2,   IDISS   = 2,
     $END
 $TIMACU
     DT     = 0.001, ITIME= 1,  TFOSO = 1.00, CFLMIN=0.0,
     $END
 $SMOACU
     ISPECJ= 2,  DIS2J = 2.0,  DIS4J = 0.2,
     ISPECK= 2,  DIS2K = 2.0,  DIS4K = 0.2,
     ISPECL= 2,  DIS2L = 2.0,  DIS4L = 0.2,
     SMOO   = 1.00,
     EPSE   = 0.35,
     $END
 $VISINP
     VISCJ = .F.,  VISCK = .F.,  VISCL = .F.,
     NTURB =   0,
     ITTYP =   1,
     ITDIR =   3,
     JTLS  =   1,
     JTLE  =  42,
     KTLS  =   1,
     KTLE  =  45,
     LTLS  =   1,
     LTLE  =  50,
     TLPAR1= 0.3,
     $END
 $BCINP
     NBC    =   6,
     IBTYP =     1, 14,   12,   54,   12,  32,
```

```
    IBDIR =     3,  2,   -1,   -2,    1,  -3,
    JBCS  =     1,  1,   42,    1,    1,   1,
    JBCE  =    42, 42,   42,   42,    1,  42,
    KBCS  =     1,  1,    1,   45,    1,   1,
    KBCE  =    45,  1,   45,   45,   45,  45,
    LBCS  =     1,  1,    1,    1,    1,  50,
    LBCE  =     1, 50,   50,   50,   50,  50,
    $END
$SCEINP
$END
```

Mach 6.0 (Viscous) File input, Restart

```
$GLOBAL
     CHIMRA= .F.,   NSTEPS=4000,   RESTRT= .T.,   NSAVE
=100,
     NQT   = 0,
     $END
 $FLOINP
     ALPHA = 0,  FSMACH = 6.0,  REY   = 6.39E7,  TINF  =
520.000,
     $END
 $VARGAM
     $END
 $GRDNAM
     NAME = 'Waverider Half-Body, 42x45x50 grid',
 $END
 $NITERS
     $END
 $METPRM
     IRHS  = 0,   ILHS  = 2,   IDISS  = 2,
     $END
 $TIMACU
     DT    = 0.005, ITIME= 1,  TFOSO = 1.00, CFLMIN=0.01,
     $END
 $SMOACU
     ISPECJ= 2,  DIS2J = 2.0,  DIS4J = 0.2,
     ISPECK= 2,  DIS2K = 2.0,  DIS4K = 0.2,
     ISPECL= 2,  DIS2L = 2.0,  DIS4L = 0.2,
     SMOO  = 1.00,
     EPSE  = 0.35,
     $END
 $VISINP
     VISCJ = .T.,  VISCK = .F.,  VISCL = .T.,
     NTURB =   1,
     ITTYP =   1,
     ITDIR =   3,
     JTLS  =   1,
     JTLE  =  42,
     KTLS  =   1,
     KTLE  =  45,
     LTLS  =   1,
     LTLE  =  50,
     TLPAR1= 0.3,
     $END
```

```
$BCINP
    NBC    =   6,
    IBTYP =     5, 14,   12,   54,   12,  32,
    IBDIR =     3,  2,   -1,   -2,    1,  -3,
    JBCS  =     1,  1,   42,    1,    1,   1,
    JBCE  =    42, 42,   42,   42,    1,  42,
    KBCS  =     1,  1,    1,   45,    1,   1,
    KBCE  =    45,  1,   45,   45,   45,  45,
    LBCS  =     1,  1,    1,    1,    1,  50,
    LBCE  =     1, 50,   50,   50,   50,  50,
    $END
$SCEINP
$END
```

Mach 6.0 (Inviscid) Engine Flow-Through model Input file, Start

```
$GLOBAL
     CHIMRA= .F.,   NSTEPS=100,   RESTRT= .F.,   NSAVE =10,
     NQT   = 0,
     $END
 $FLOINP
     ALPHA = 0,  FSMACH = 6.0,  REY   = 6.39E7,  TINF  =
520.000,
     $END
 $VARGAM
     $END
 $GRDNAM
     NAME = 'Waverider Half-Body, 42x45x50 grid',
 $END
 $NITERS
     $END
 $METPRM
     IRHS  = 0,   ILHS  = 2,   IDISS  = 2,
     $END
 $TIMACU
     DT    = 0.001, ITIME= 1,  TFOSO = 1.00, CFLMIN=0.0,
     $END
 $SMOACU
     ISPECJ= 2,  DIS2J = 2.0,  DIS4J = 0.2,
     ISPECK= 2,  DIS2K = 2.0,  DIS4K = 0.2,
     ISPECL= 2,  DIS2L = 2.0,  DIS4L = 0.2,
     SMOO  = 1.00,
     EPSE  = 0.35,
     $END
 $VISINP
     VISCJ = .F.,  VISCK = .F.,  VISCL = .F.,
     NTURB =   0,
     ITTYP =   1,
     ITDIR =   3,
     JTLS  =   1,
     JTLE  =  42,
     KTLS  =   1,
     KTLE  =  45,
     LTLS  =   1,
     LTLE  =  50,
     TLPAR1= 0.3,
     $END
 $BCINP
```

```
    NBC    =   8,
    IBTYP =     1, 14,   12,   54,   12,  32,  30,  40,
    IBDIR =     3,  2,   -1,   -2,    1,  -3,   3,   3,
    JBCS  =     1,  1,   42,    1,    1,   1,  38,  38,
    JBCE  =    42, 42,   42,   42,    1,  42,  42,  42,
    KBCS  =     1,  1,    1,   45,    1,   1,  21,  37,
    KBCE  =    45,  1,   45,   45,   45,  45,  26,  40,
    LBCS  =     1,  1,    1,    1,    1,  50,   1,   1,
    LBCE  =     1, 50,   50,   50,   50,  50,   1,   1,
    $END
$SCEINP
$END
```

APPENDIX C. FLOW SOLUTIONS

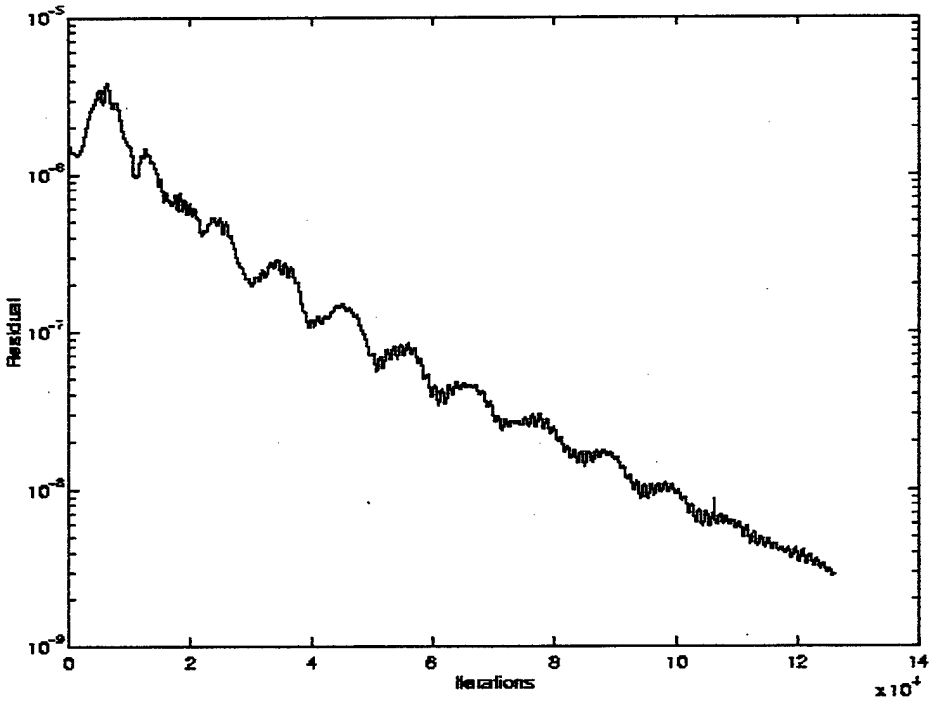

Figure C-1. Mach 0.3 Inviscid Convergence History

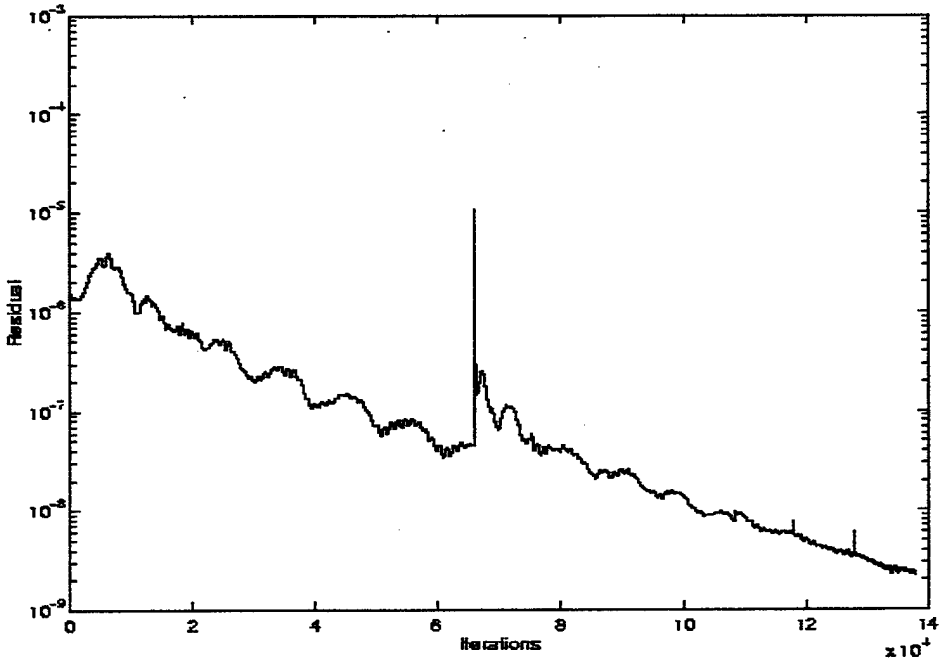

Figure C-2. Mach 0.3 Viscous Convergence History

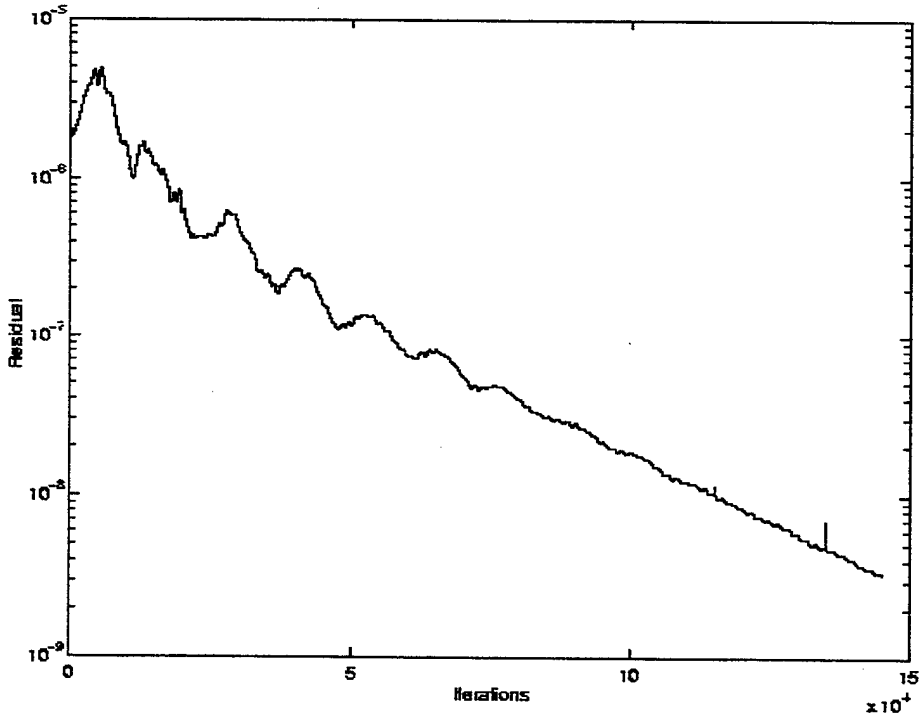

Figure C-3. Mach 0.4 Inviscid Convergence History

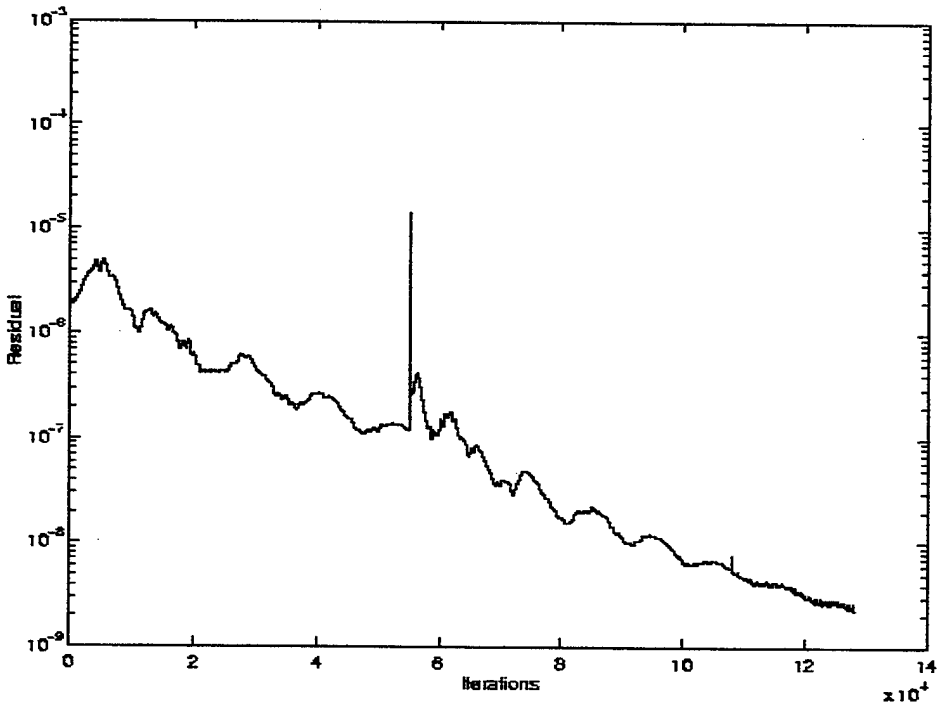

Figure C-4. Mach 0.4 Viscous Convergence History

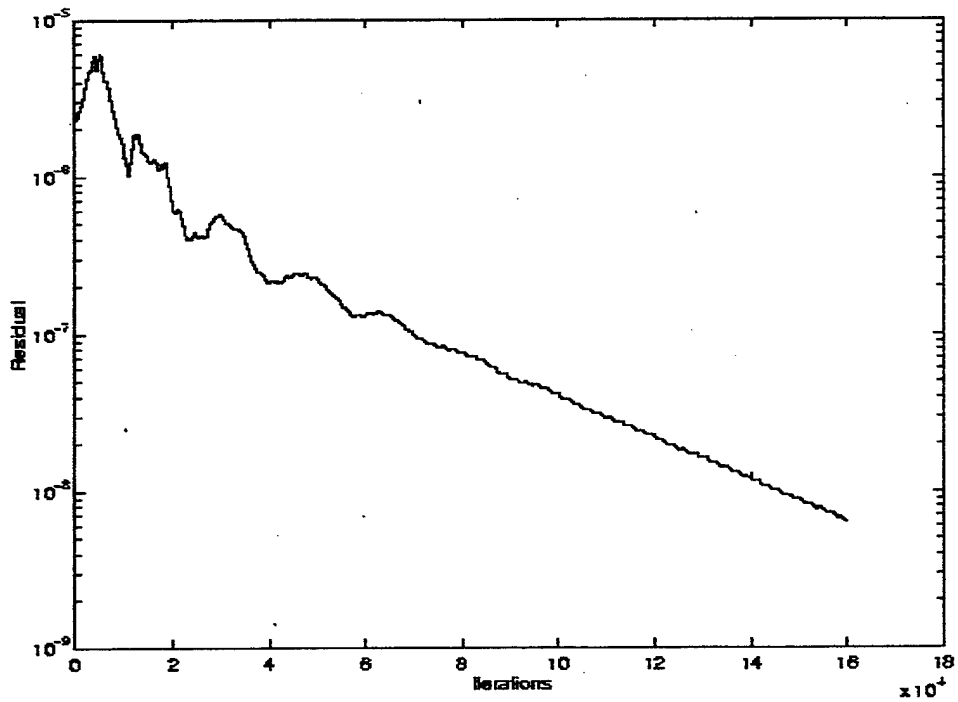

Figure C-5. Mach 0.5 Inviscid Convergence History

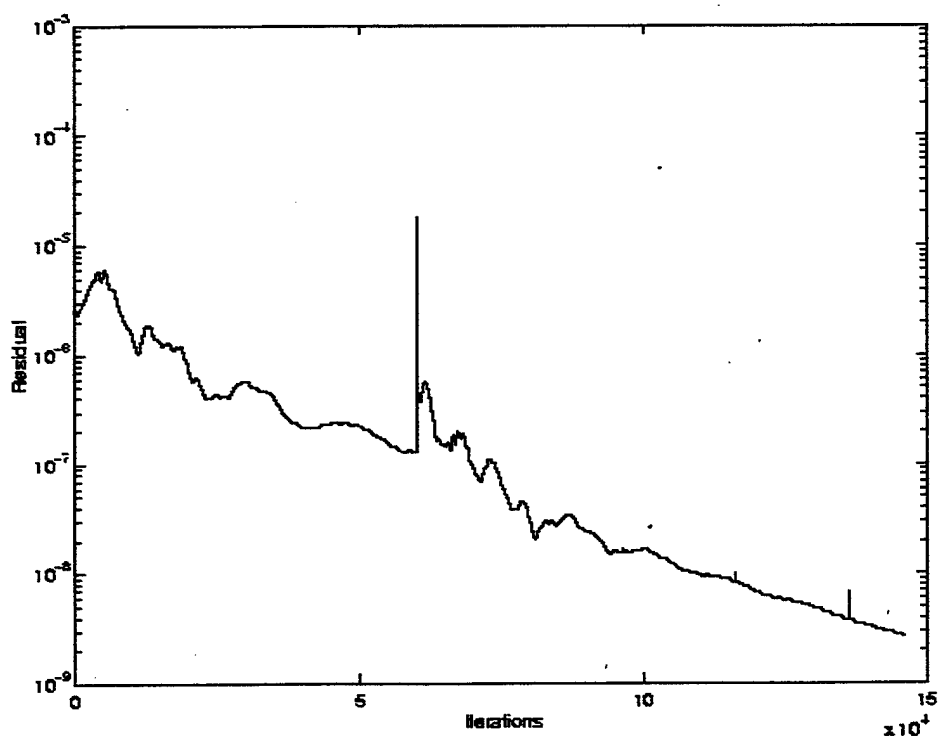

Figure C-6. Mach 0.5 Viscous Convergence History

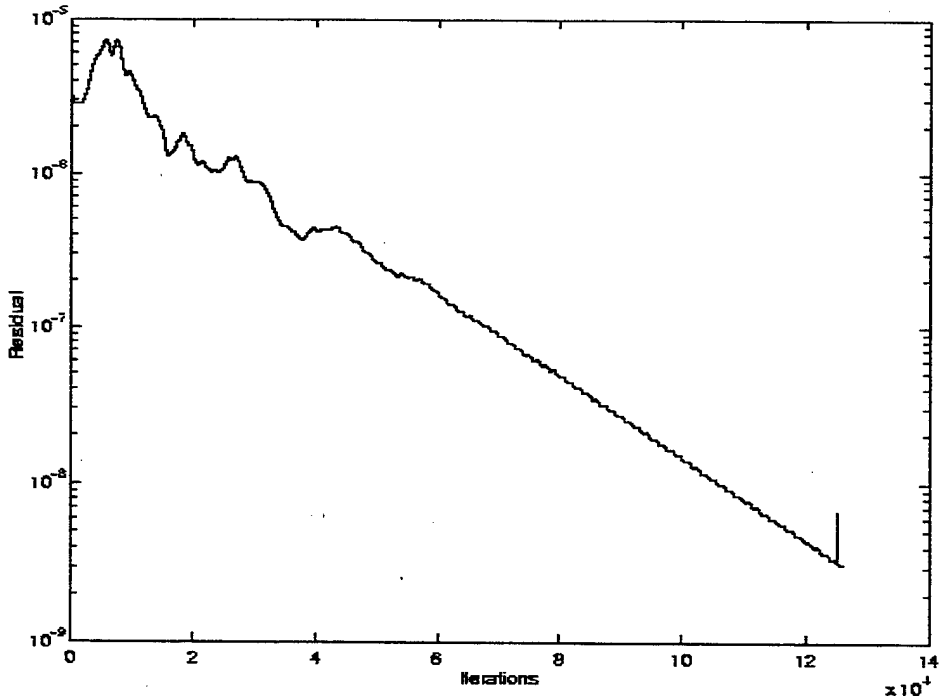

Figure C-7. Mach 0.6 Inviscid Convergence History

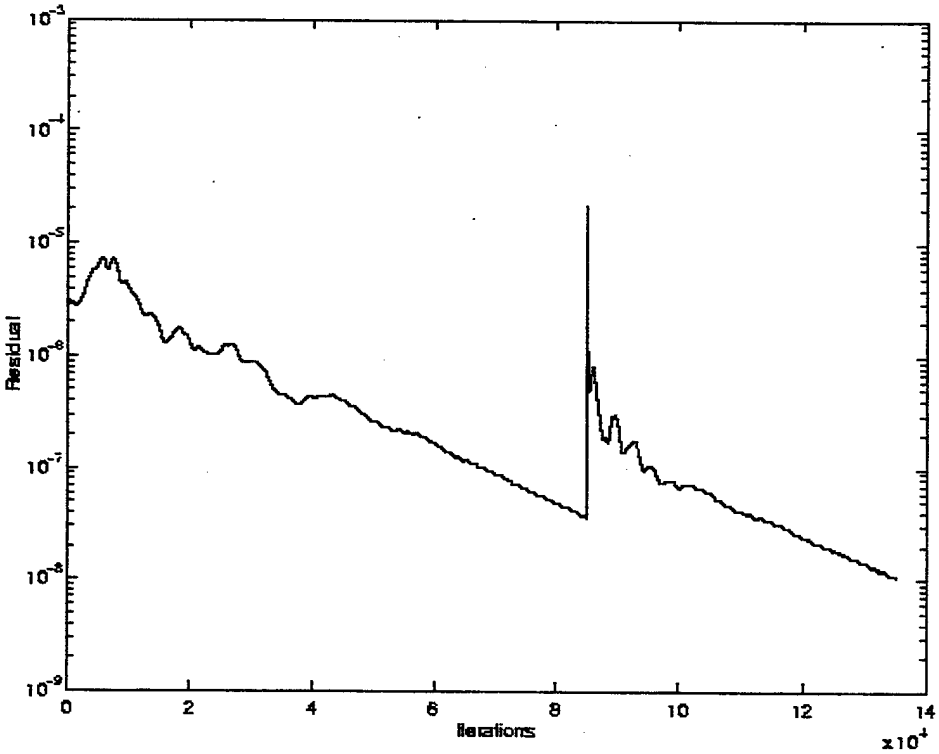

Figure C-8. Mach 0.6 Viscous Convergence History

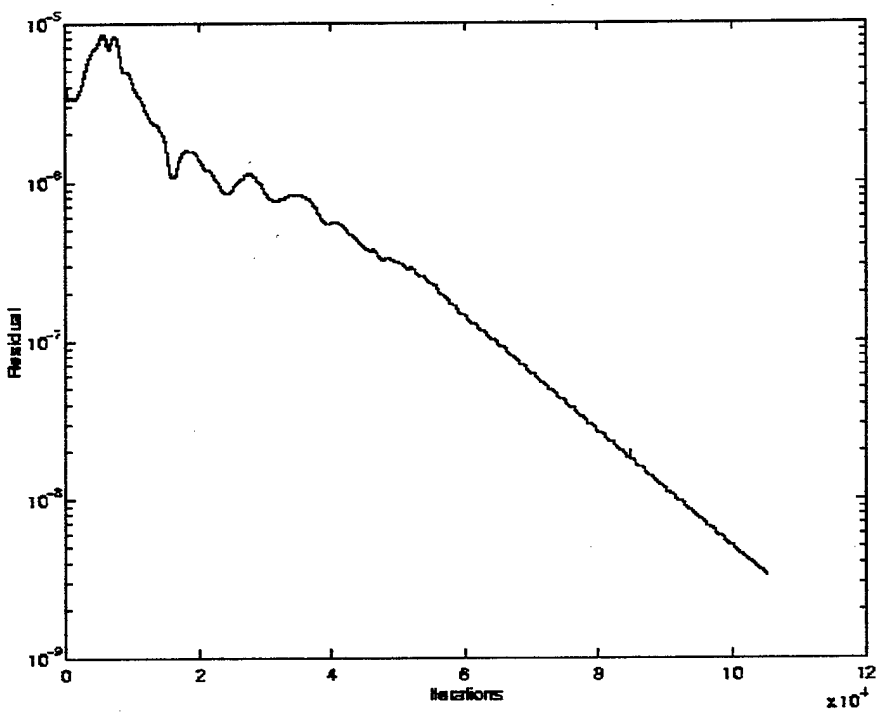

Figure C-9. Mach 0.7 Inviscid Convergence History

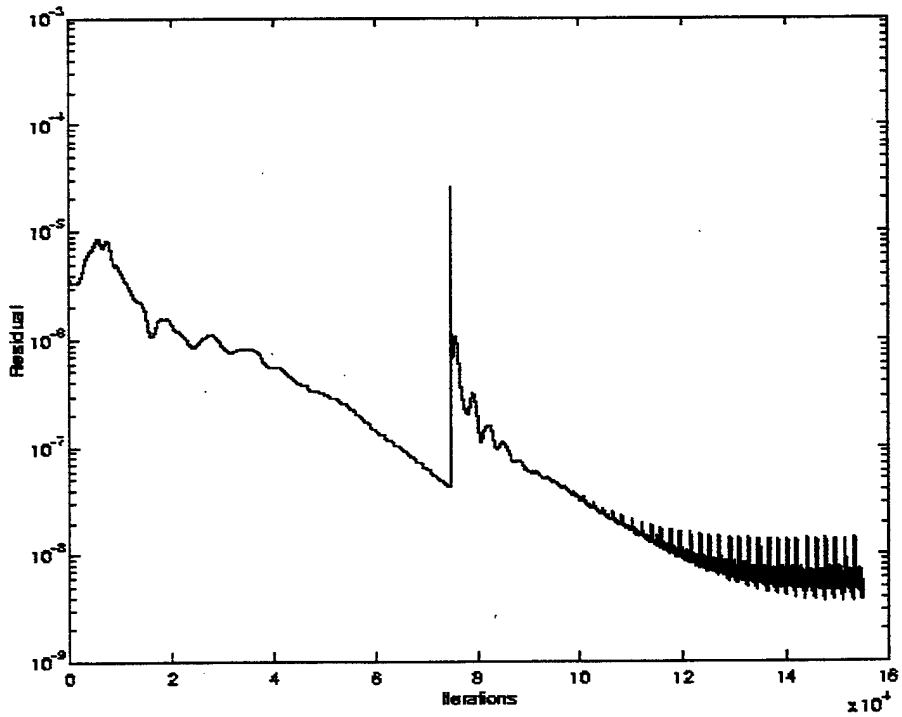

Figure C-10. Mach 0.7 Viscous Convergence History

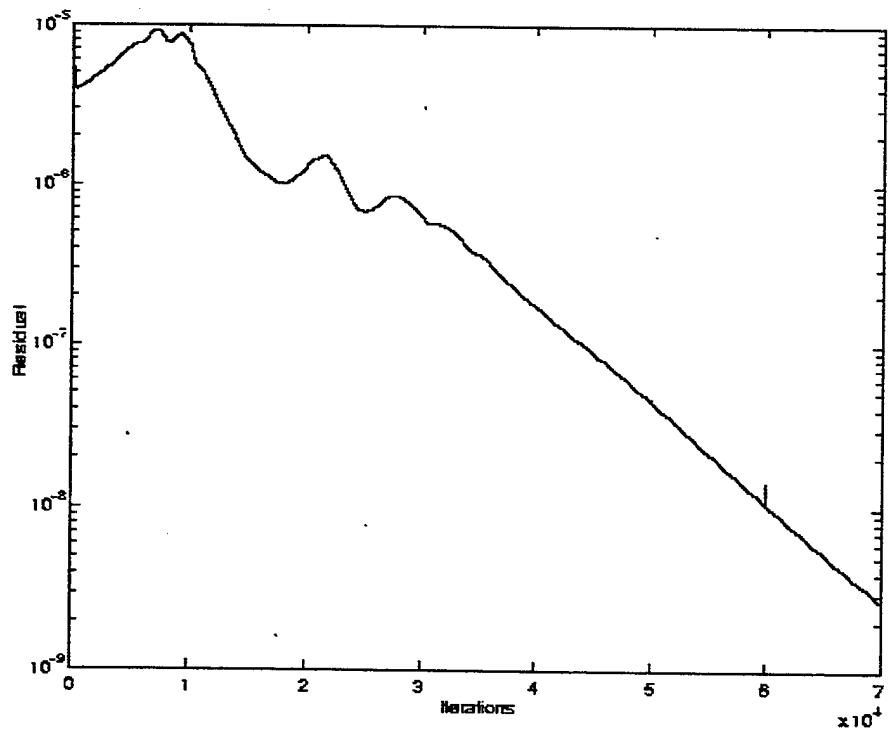

Figure C-11. Mach 0.8 Inviscid Convergence History

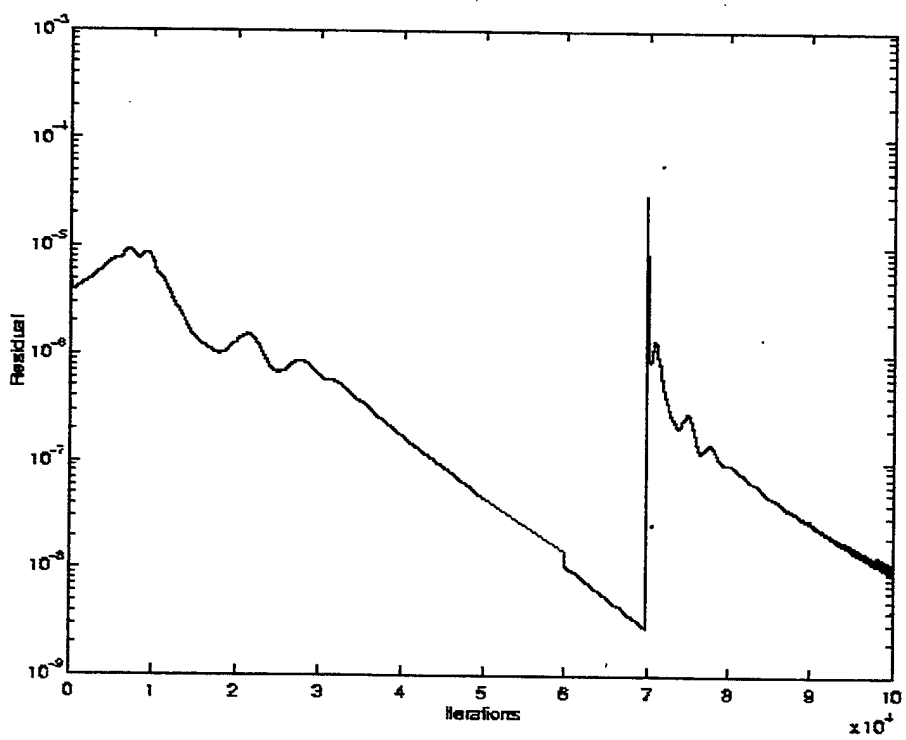

Figure C-12. Mach 0.8 Viscous Convergence History

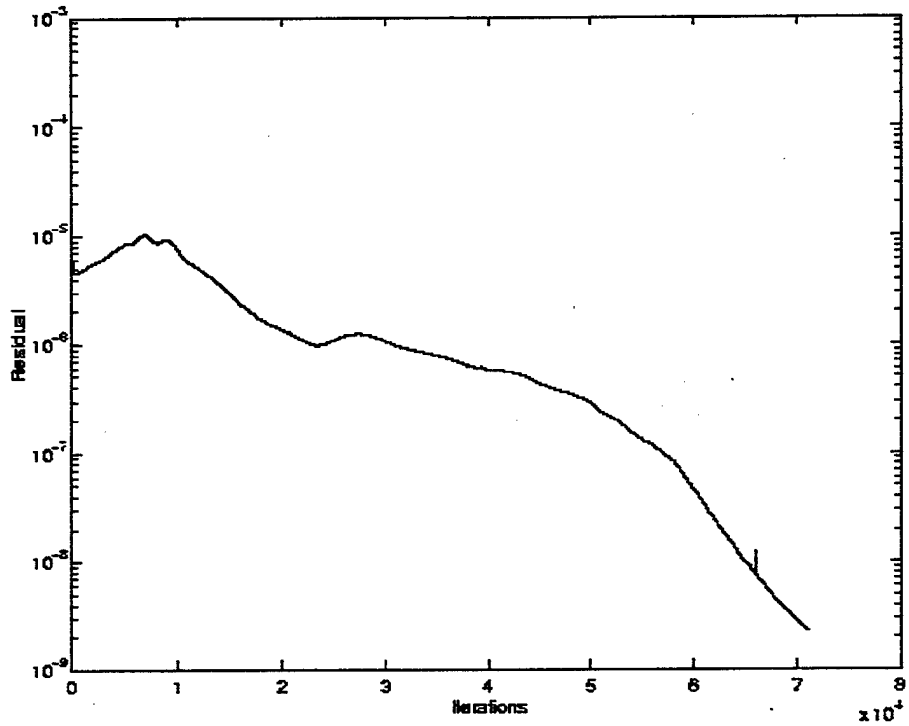

Figure C-13. Mach 0.9 Inviscid Convergence History

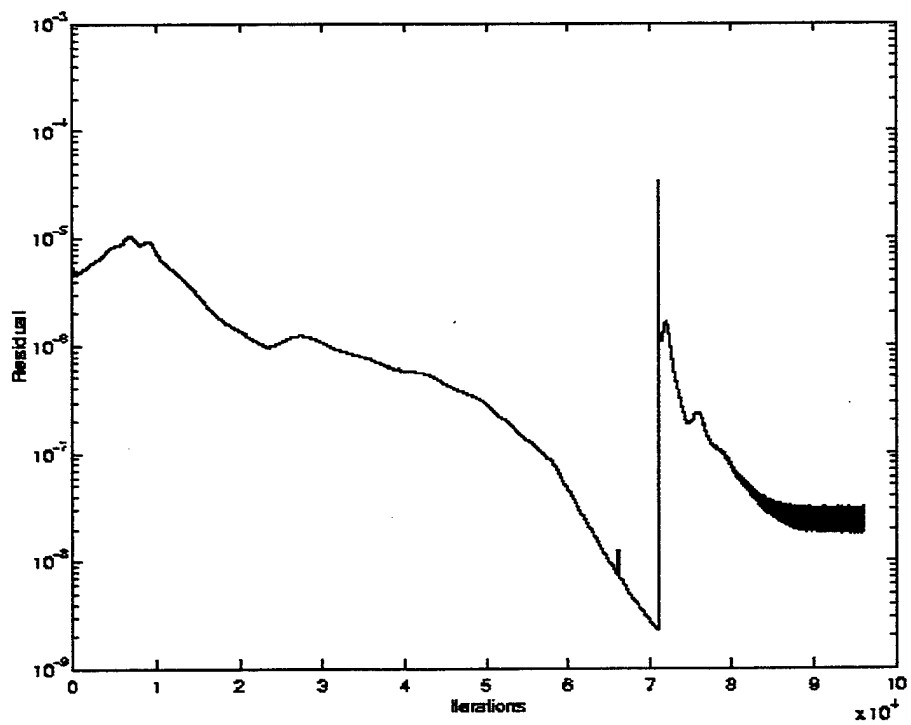

Figure C-14. Mach 0.9 Viscous Convergence History

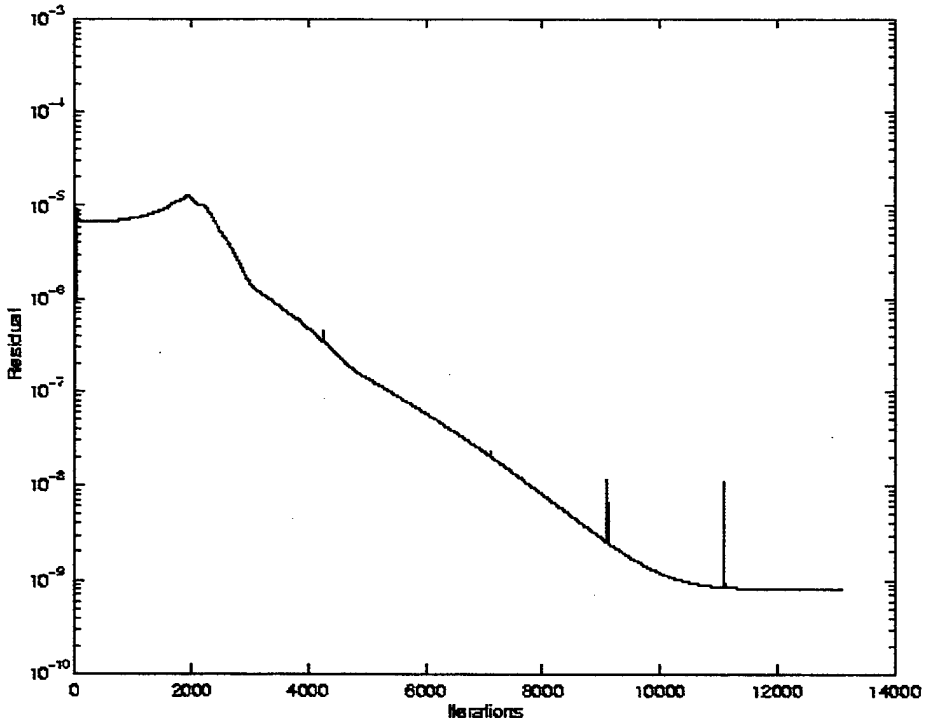

Figure C-15. Mach 1.2 Inviscid Convergence History

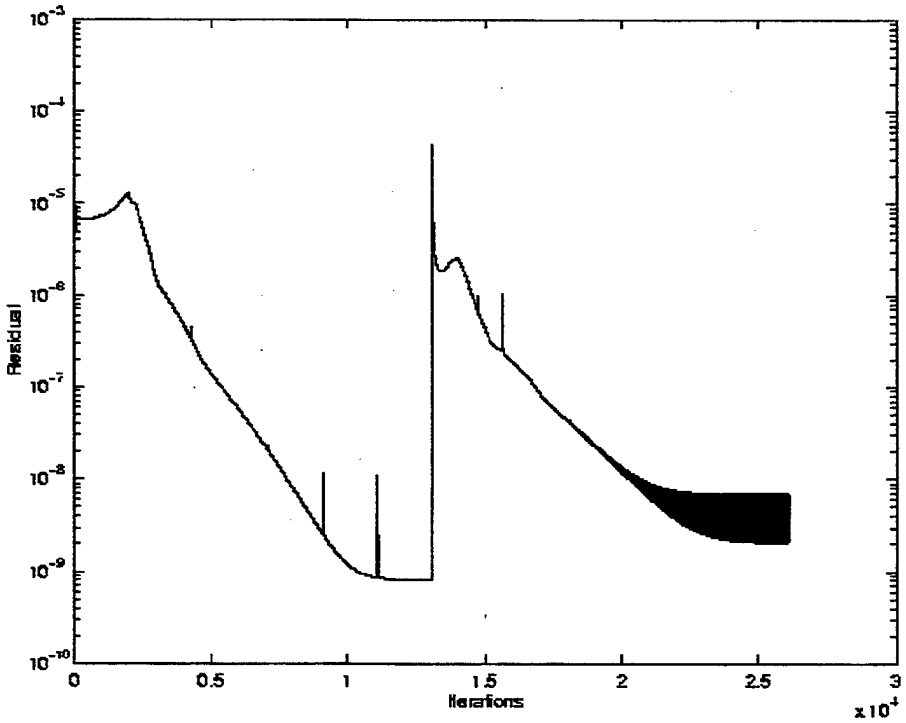

Figure C-16. Mach 1.2 Viscous Convergence History

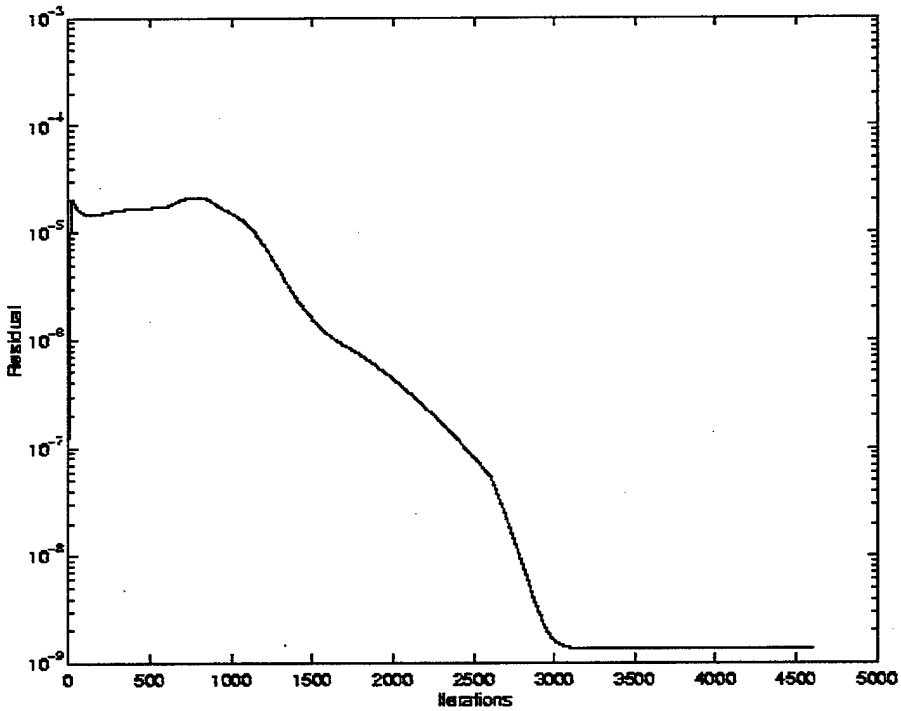

Figure C-17. Mach 2.0 Inviscid Convergence History

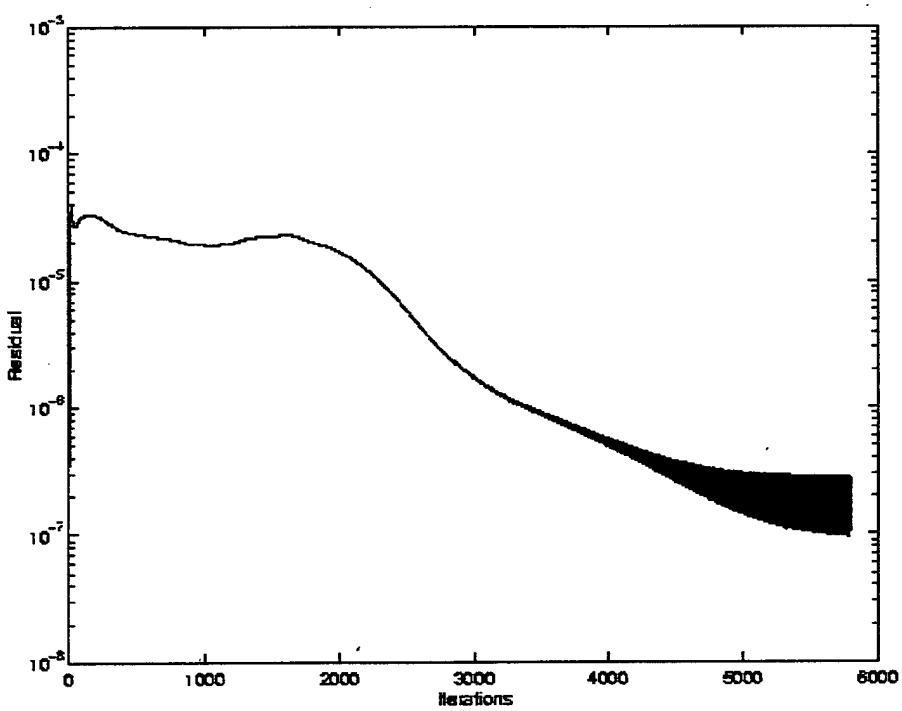

Figure C-18. Mach 2.0 Viscous Convergence History

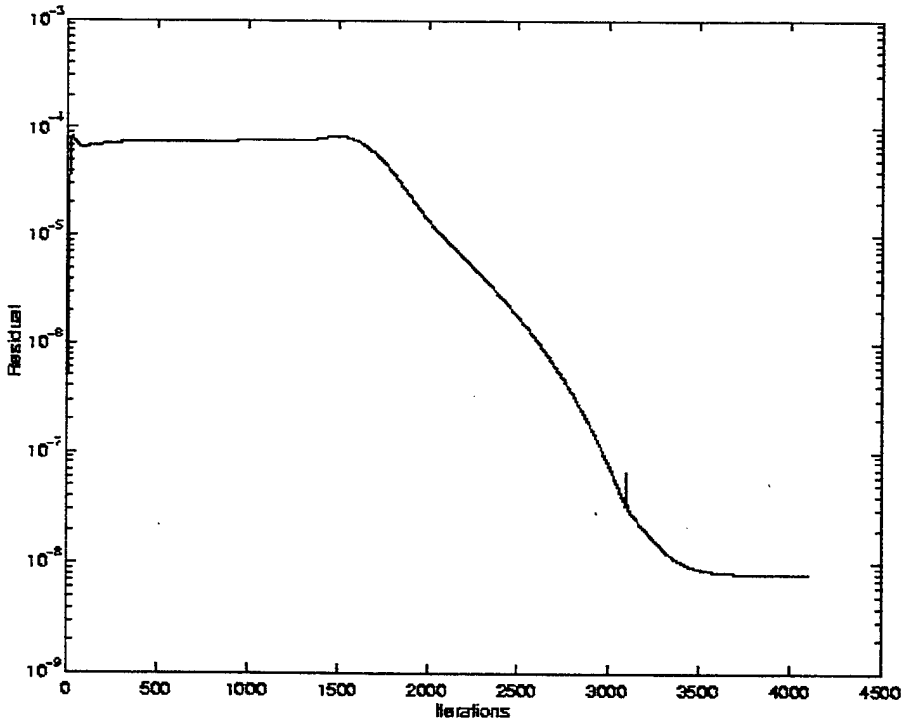

Figure C-19. Mach 4.0 Inviscid Convergence History

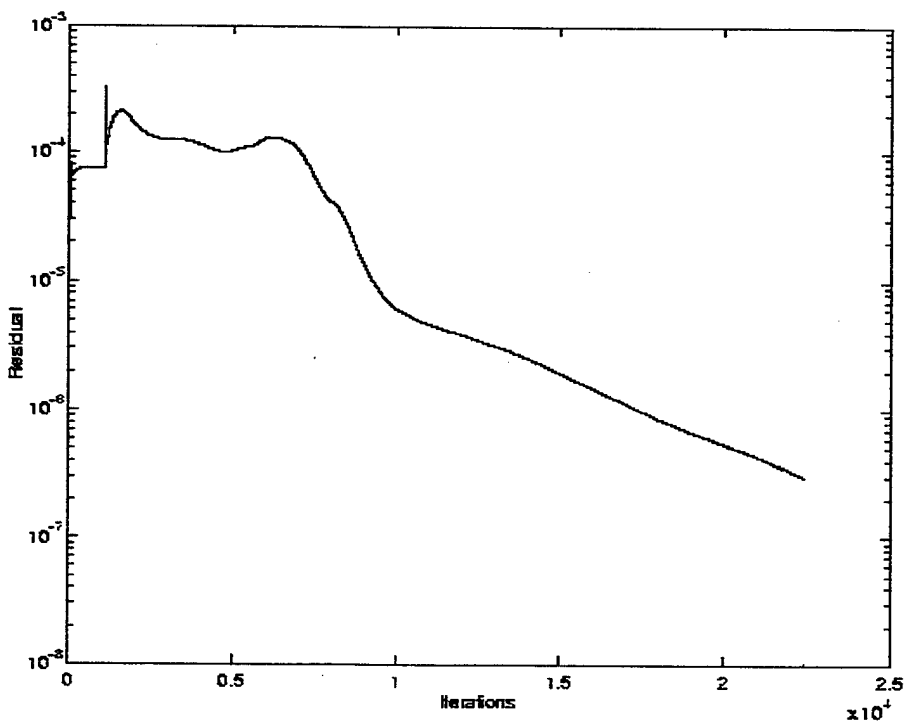

Figure C-20. Mach 4.0 Viscous Convergence History

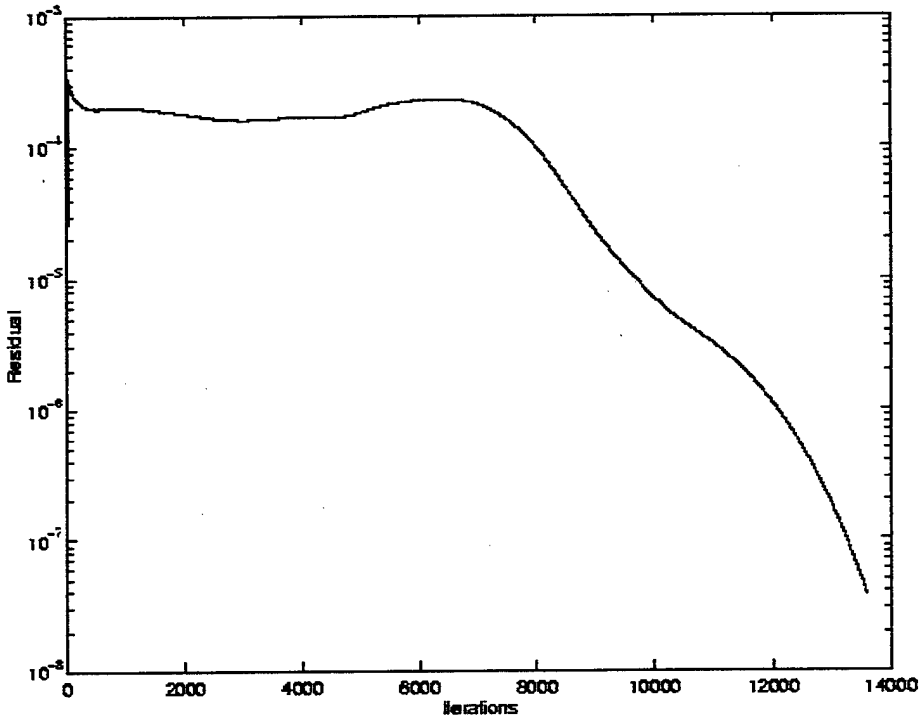

Figure C-21. Mach 6.0 Inviscid Convergence History

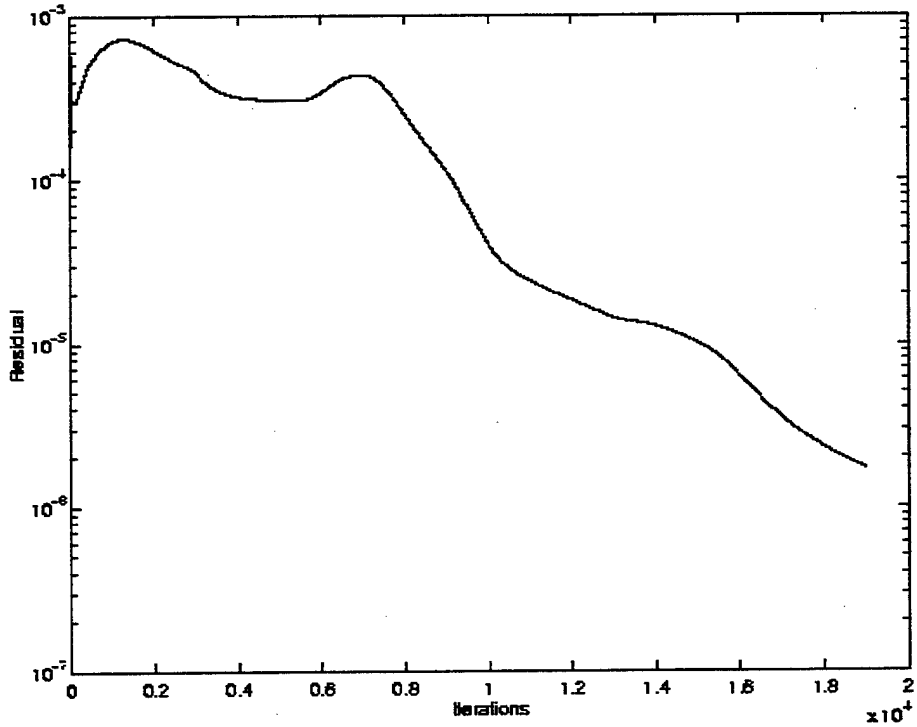

Figure C-22. Mach 6.0 Viscous Convergence History

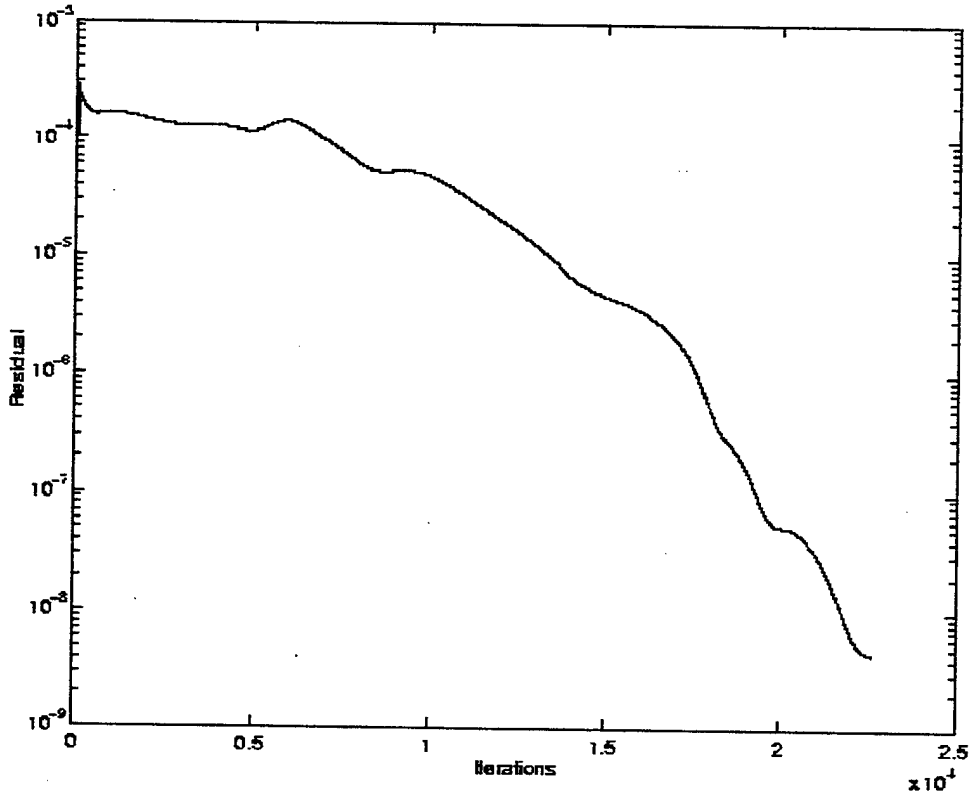

Figure C-23. Mach 6.0 Inviscid Engine Flow-Through Convergence History

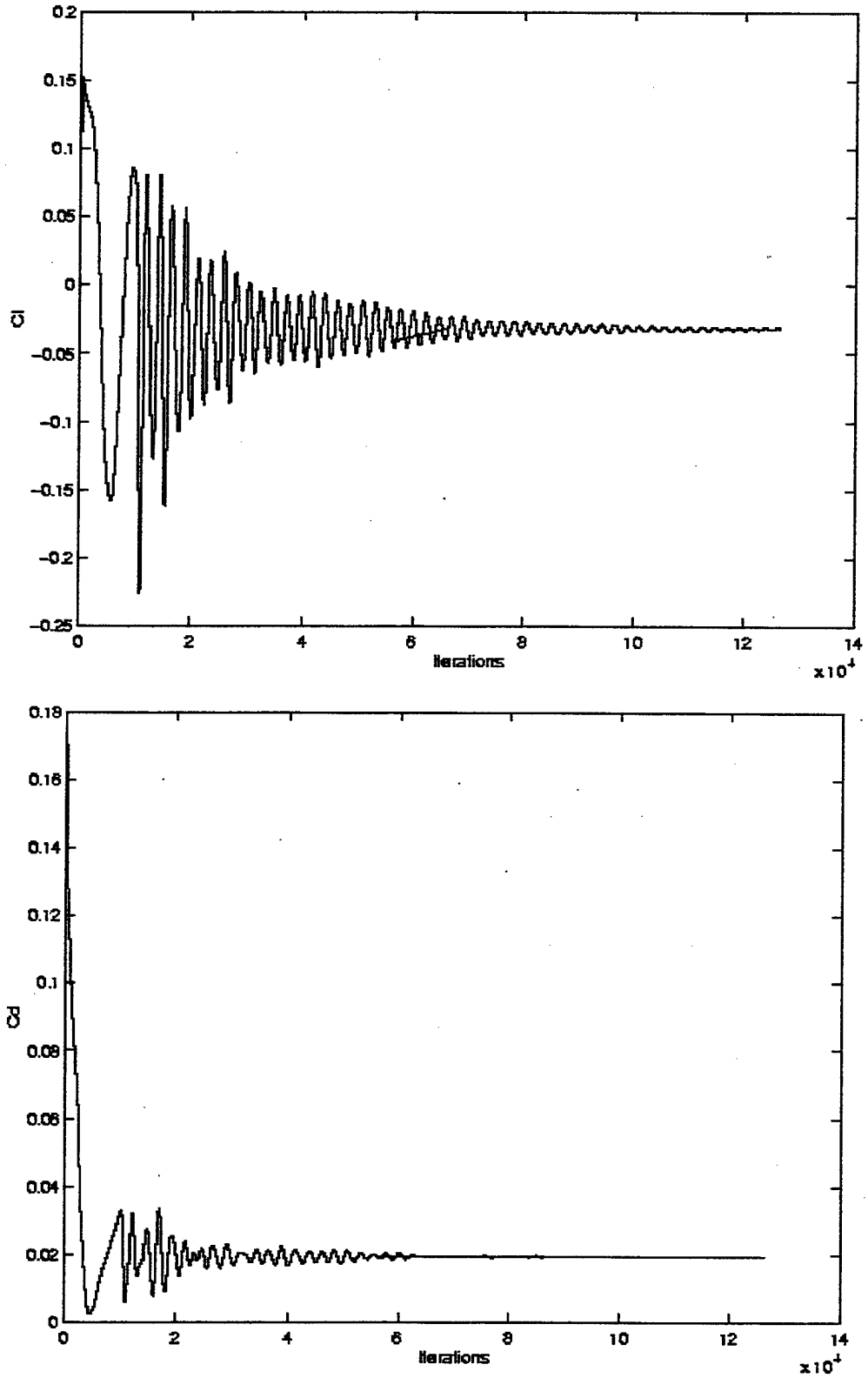

Figure C-24. Force Coefficients vs. Iterations Mach 0.3 Inviscid

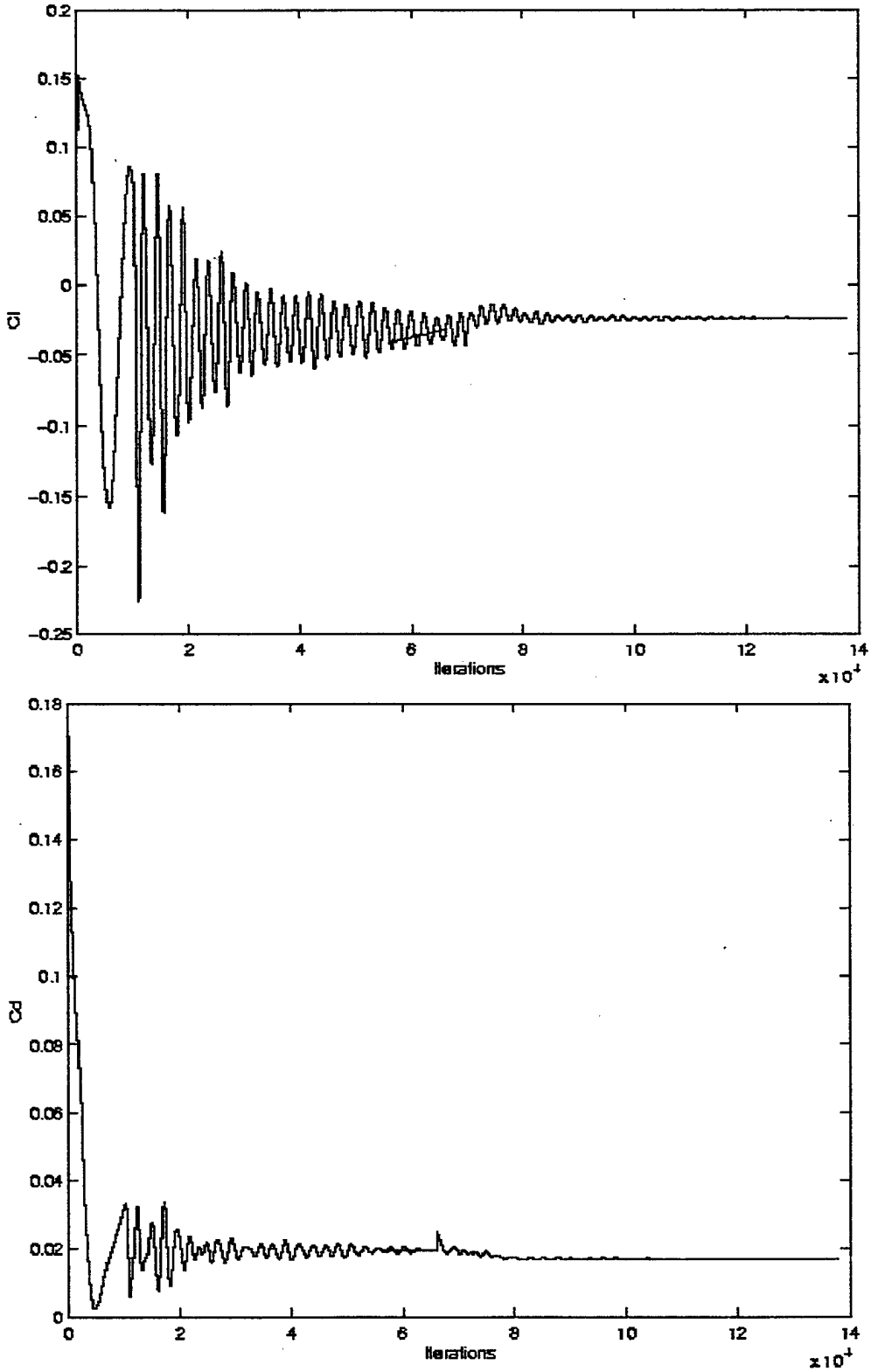

Figure C-25. Force Coefficients vs. Iterations Mach 0.3 Viscous

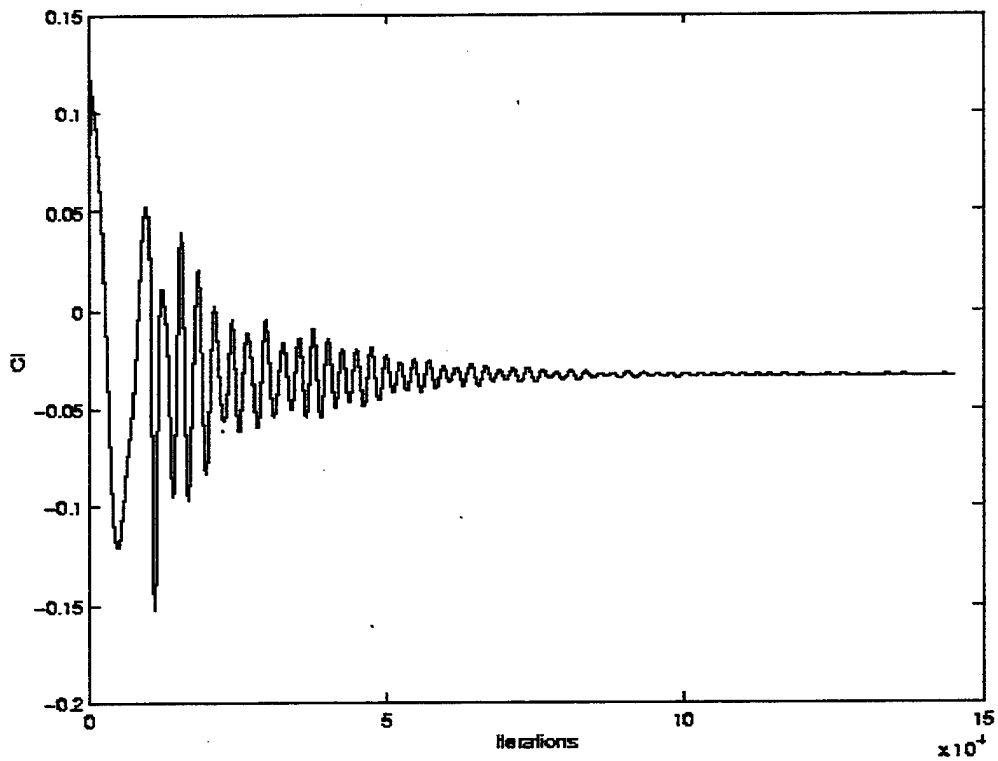

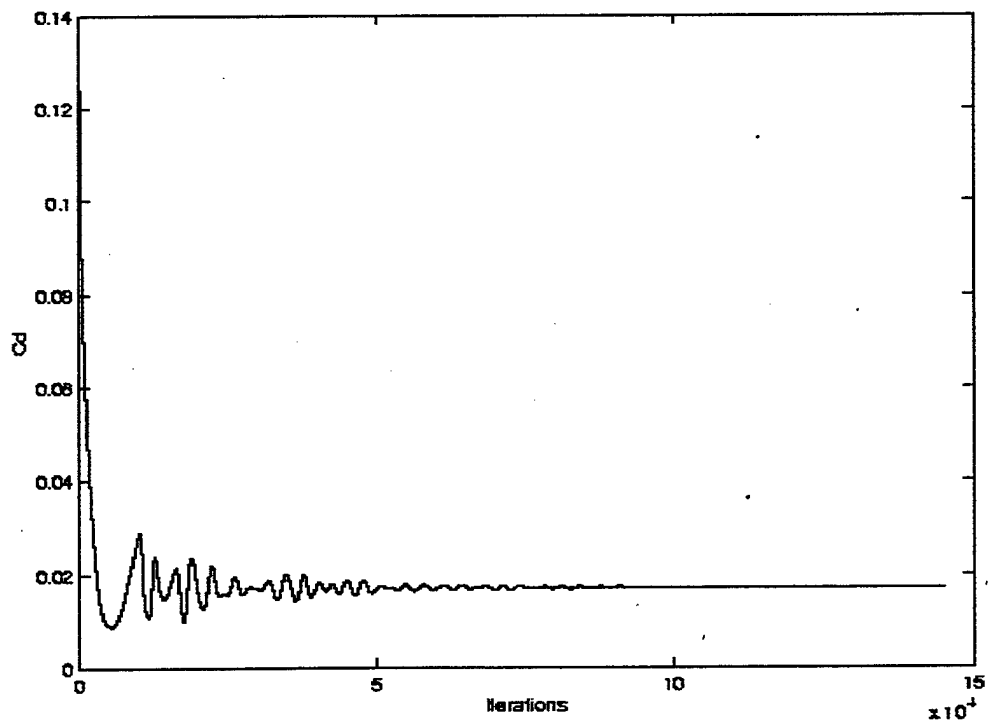

Figure C-26. Force Coefficients vs. Iterations Mach 0.4 Inviscid

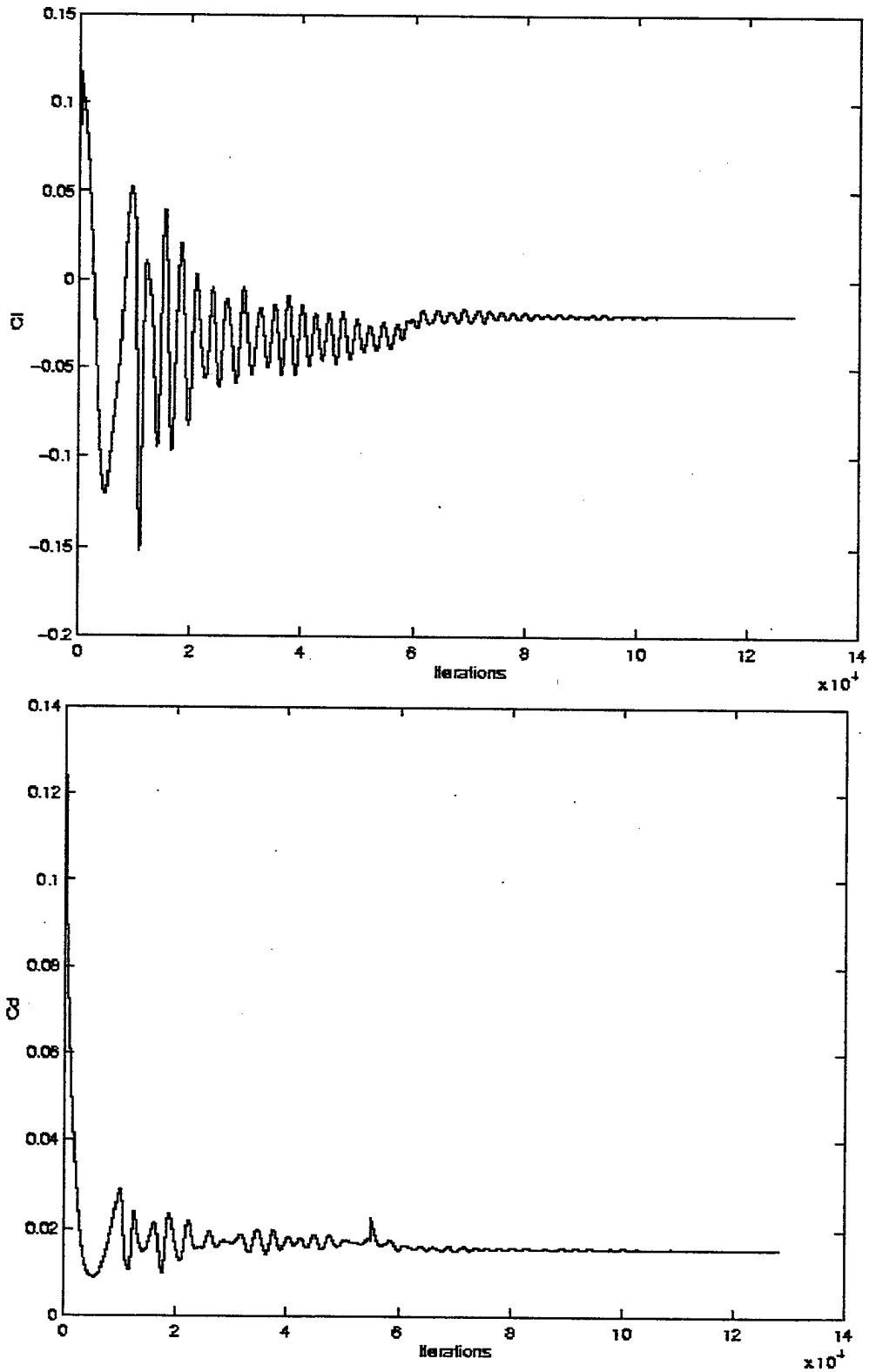

Figure C-27. Force Coefficients vs. Iterations Mach 0.4 Viscous

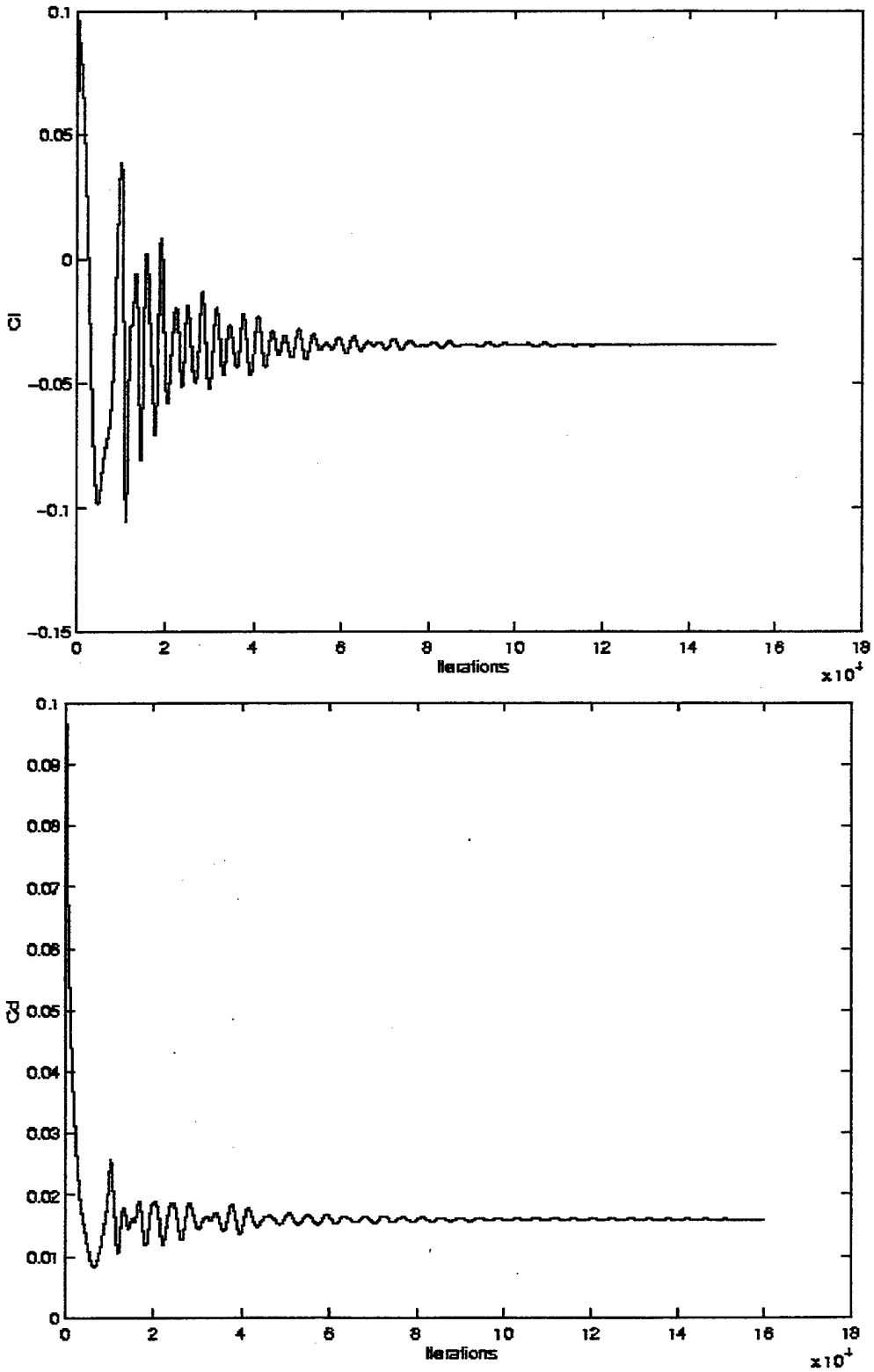

Figure C-28. Force Coefficients vs. Iterations Mach 0.5 Inviscid

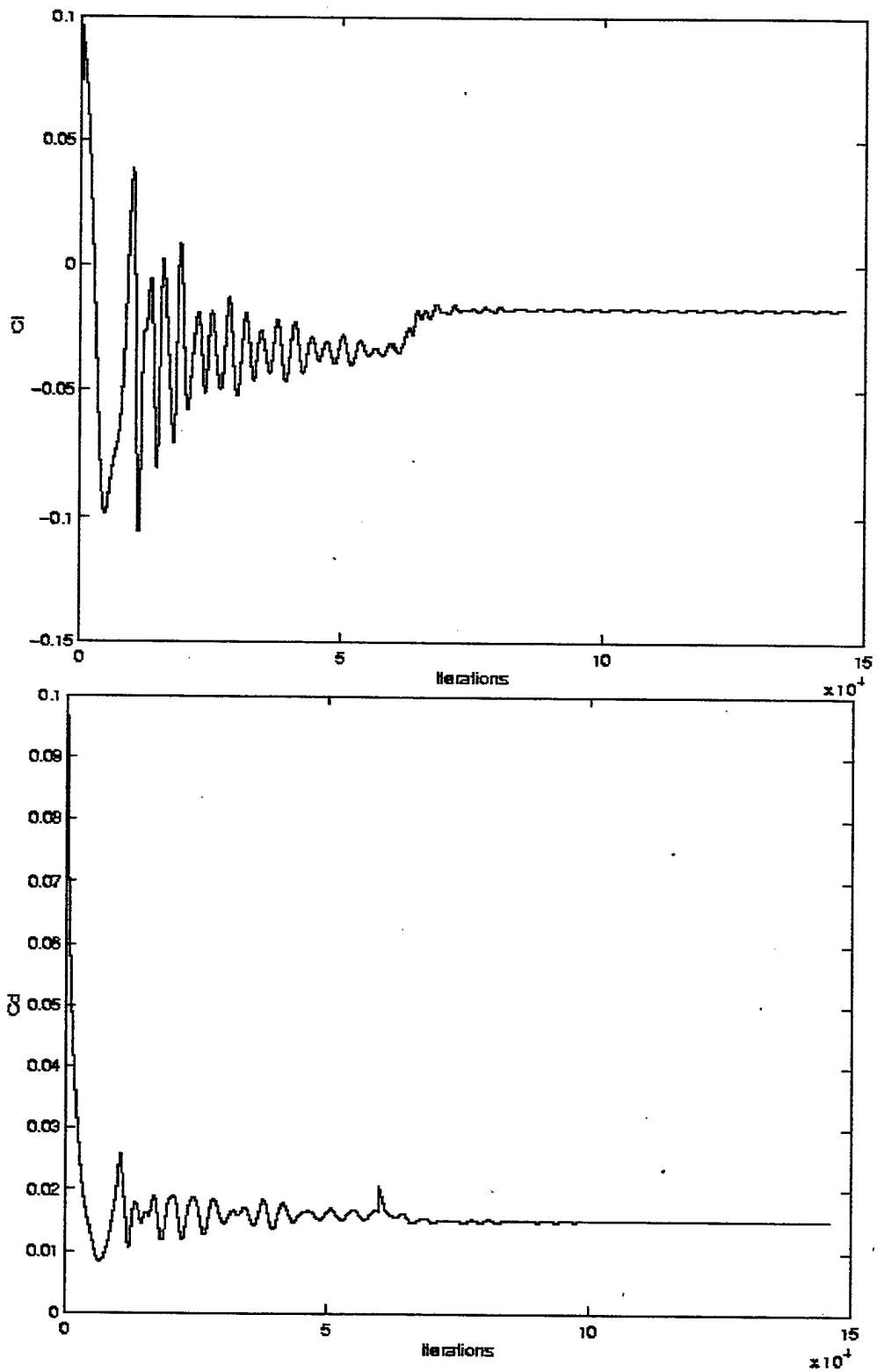

Figure C-29. Force Coefficients vs. Iterations Mach 0.5 Viscous

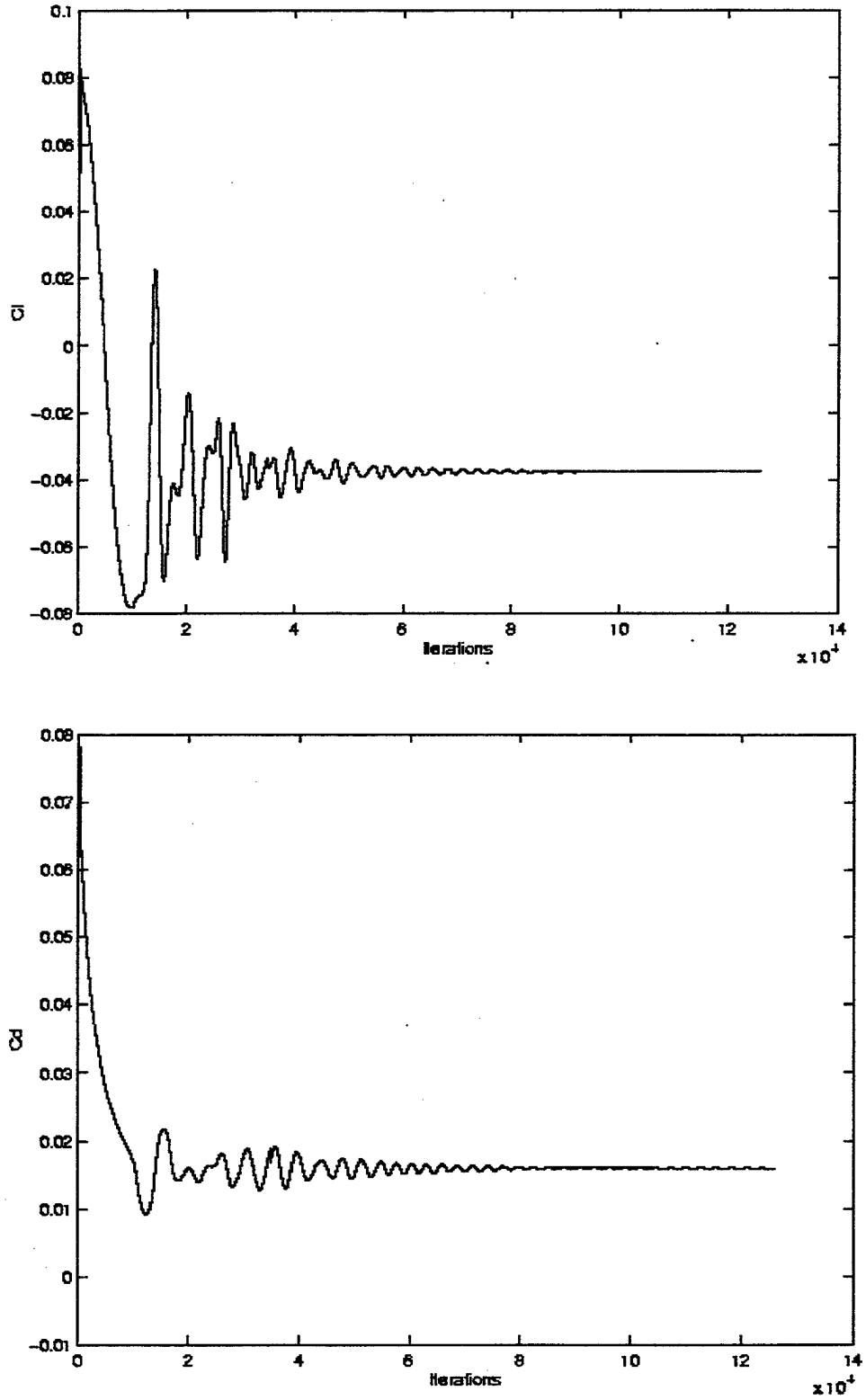

Figure C-30. Force Coefficients vs. Iterations Mach 0.6 Inviscid

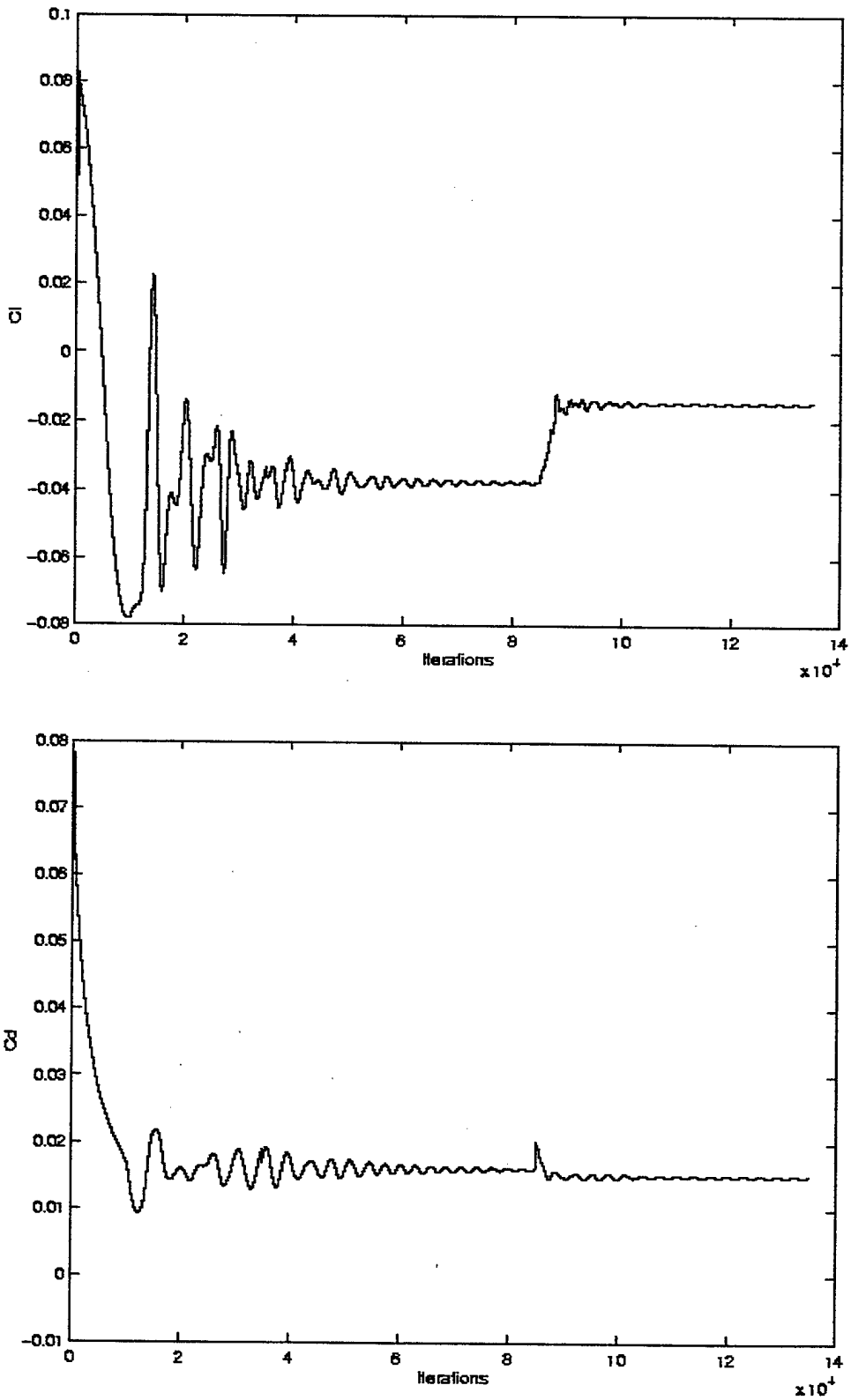

Figure C-31. Force Coefficients vs. Iterations Mach 0.6 Viscous

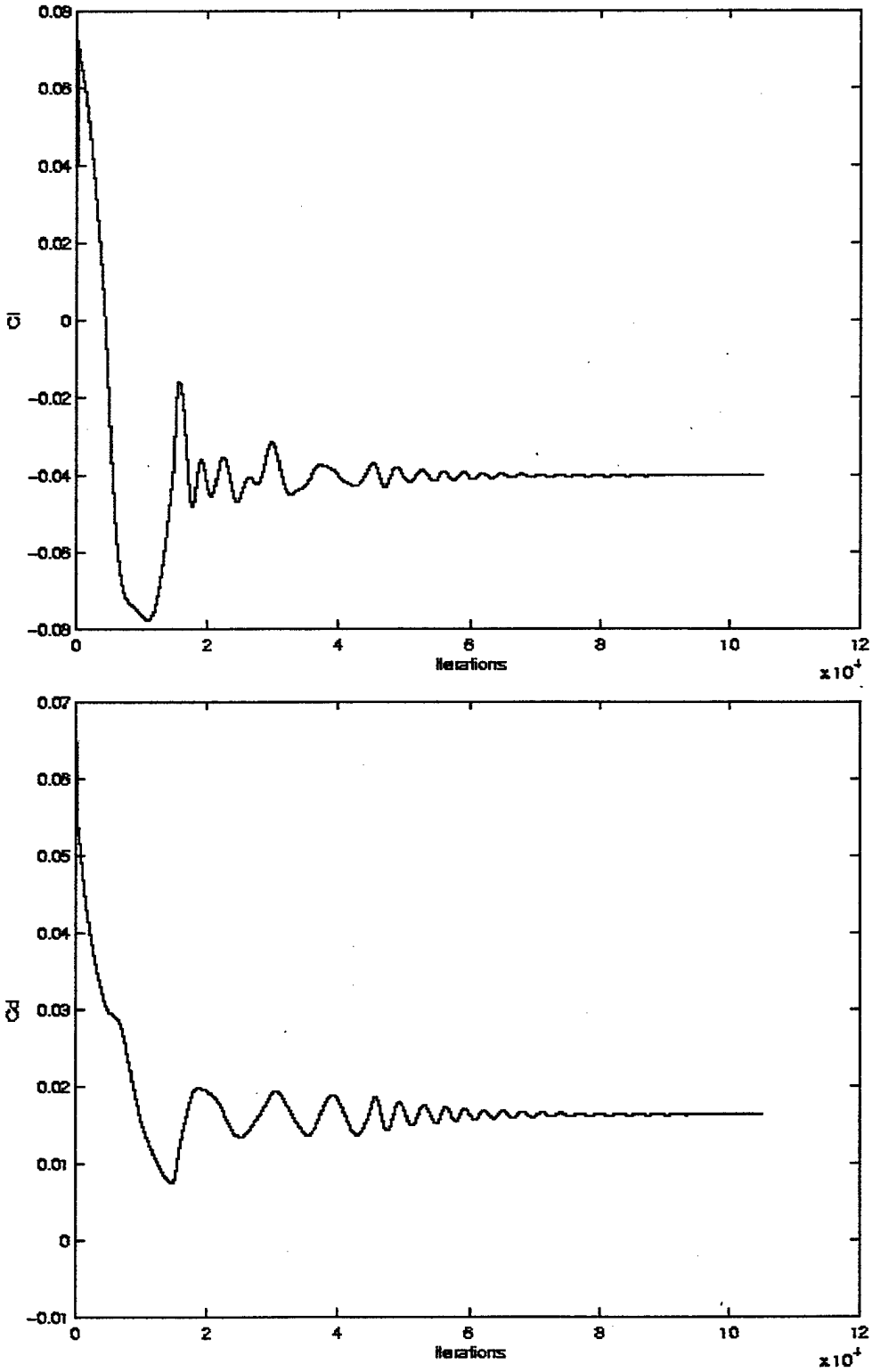

Figure C-32. Force Coefficients vs. Iterations Mach 0.7 Inviscid

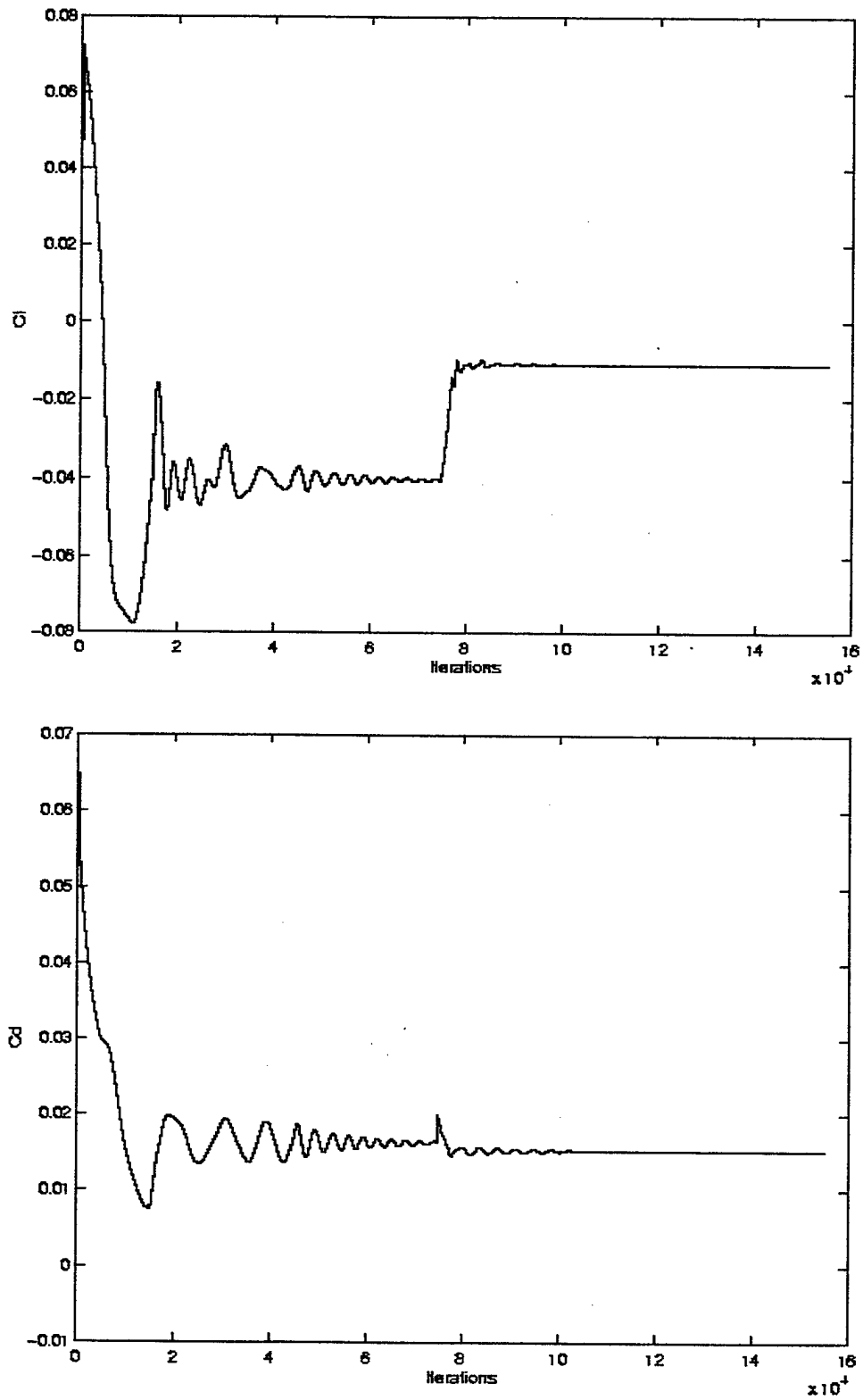

Figure C-33. Force Coefficients vs. Iterations Mach 0.7 Viscous

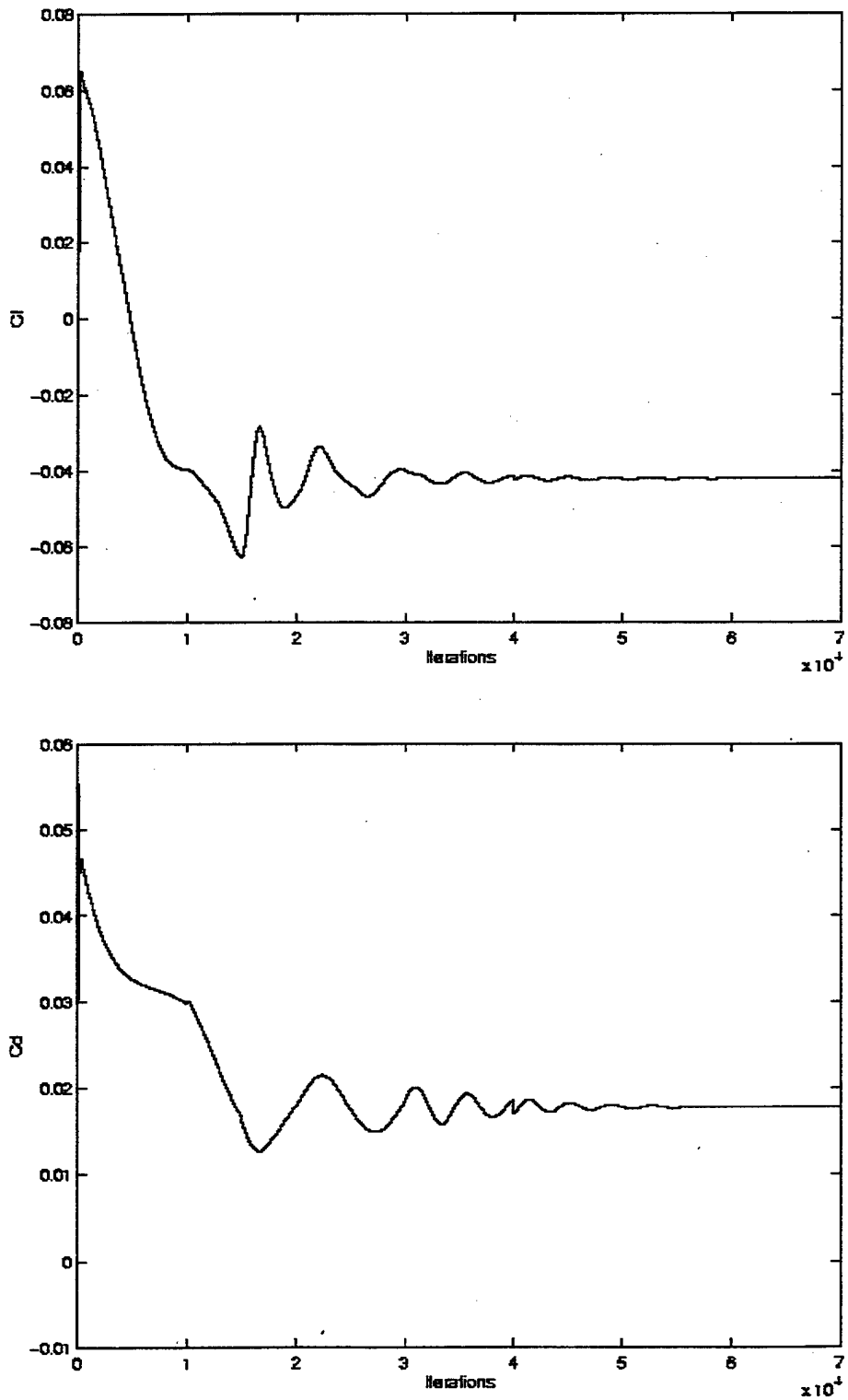

Figure C-34. Force Coefficients vs. Iterations Mach 0.8 Inviscid

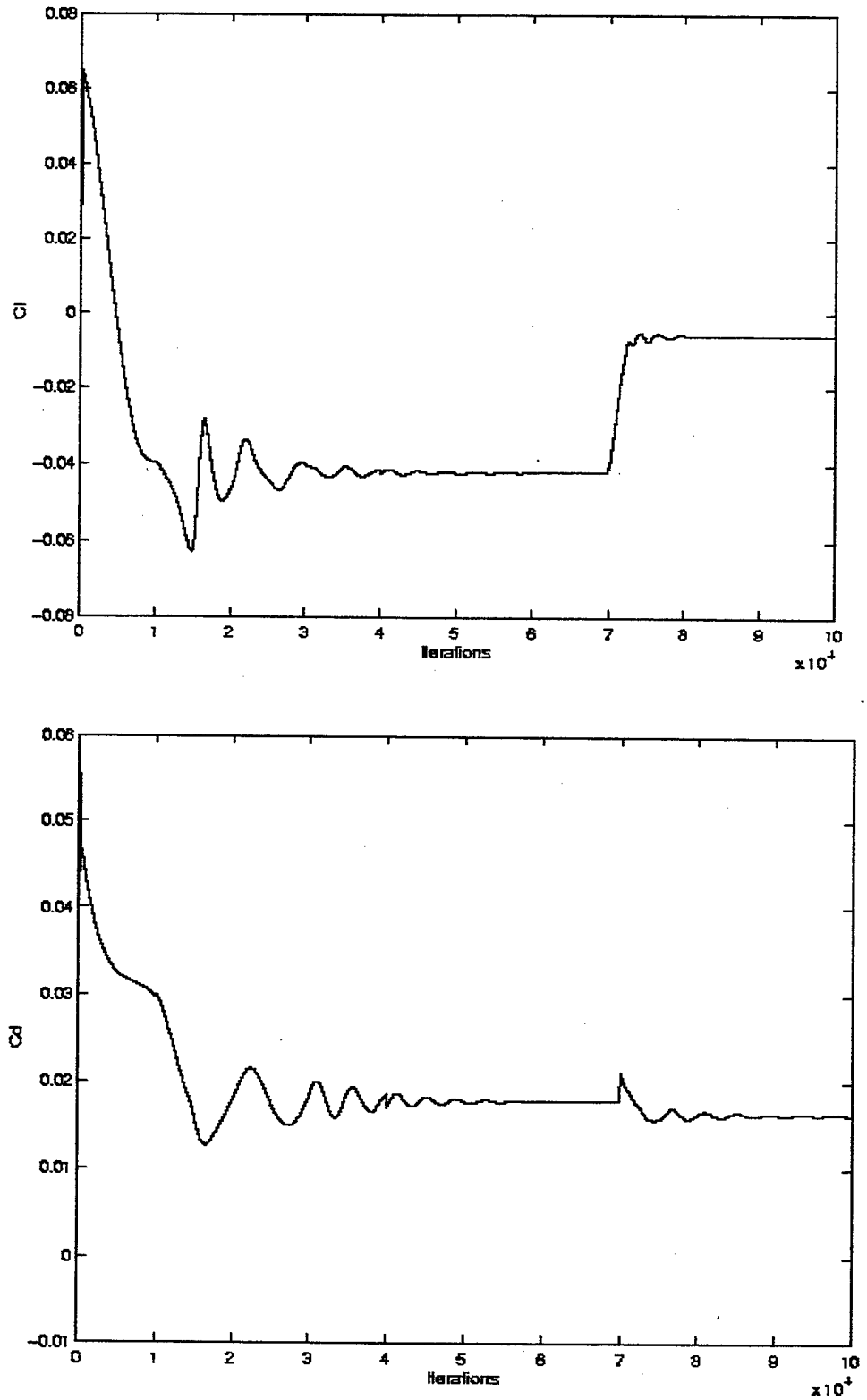

Figure C-35. Force Coefficients vs. Iterations Mach 0.8 Viscous

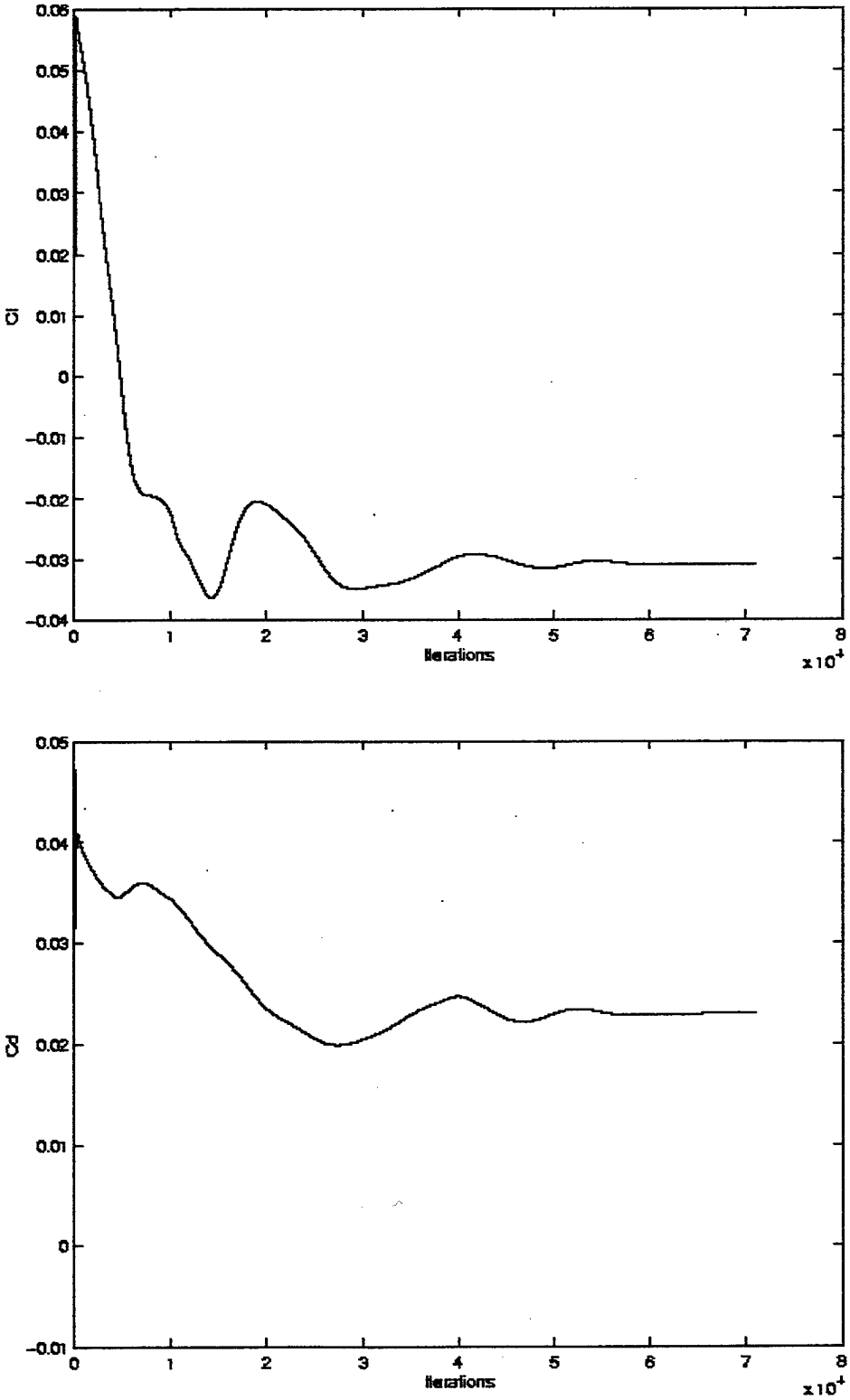

Figure C-36. Force Coefficients vs. Iterations Mach 0.9 Inviscid

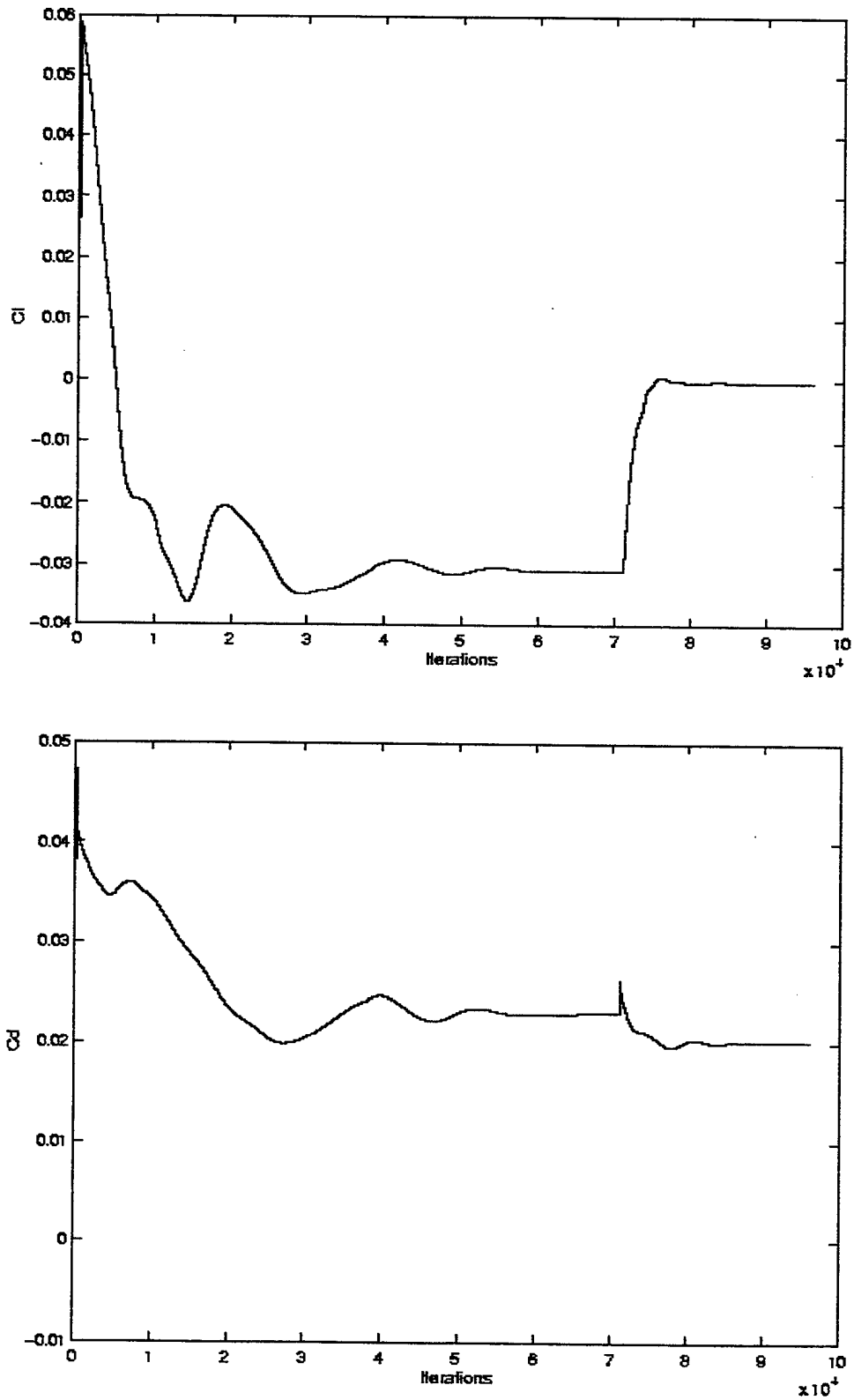

Figure C-37. Force Coefficients vs. Iterations Mach 0.9 Viscous

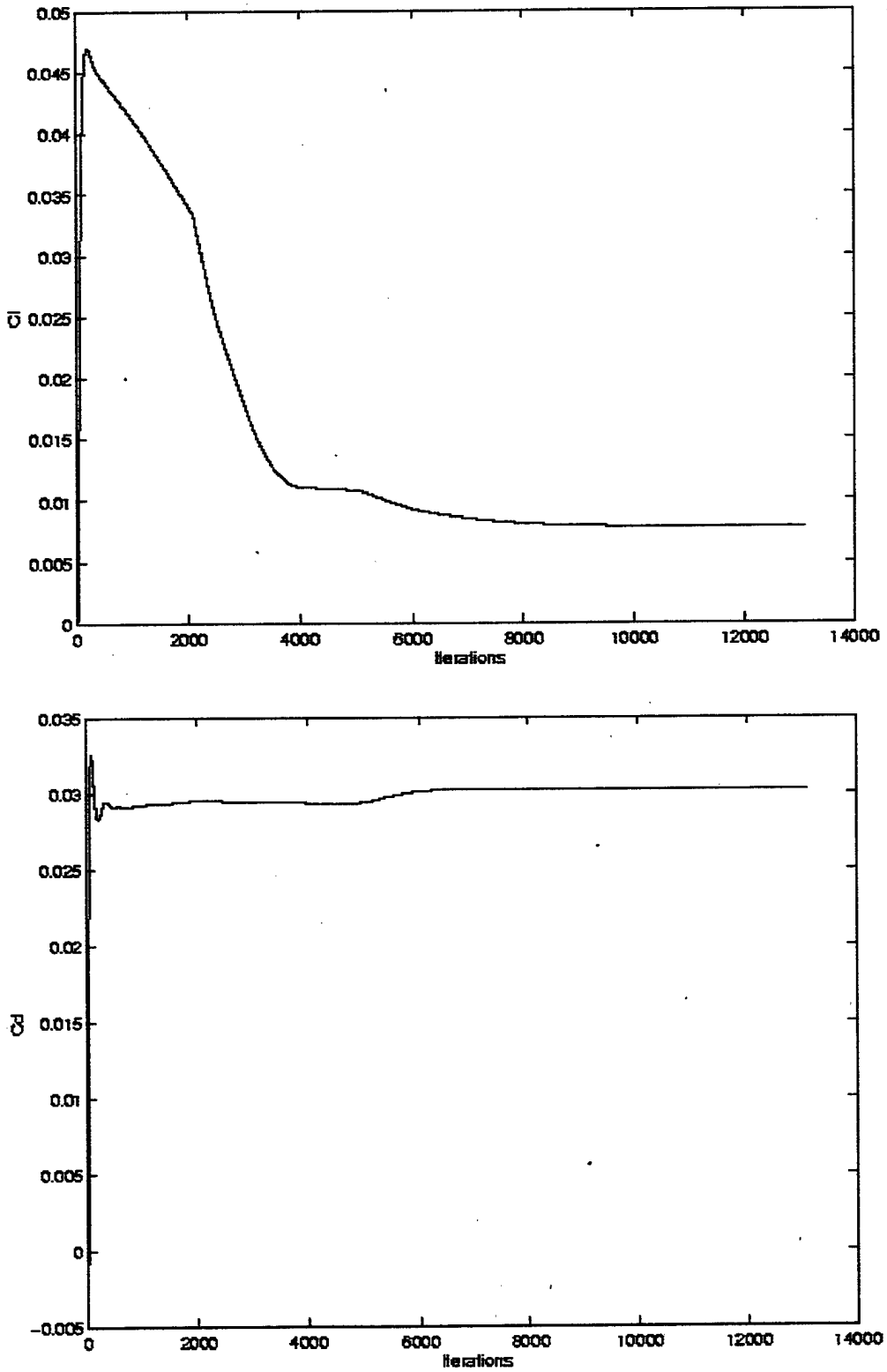

Figure C-38. Force Coefficients vs. Iterations Mach 1.2 Inviscid

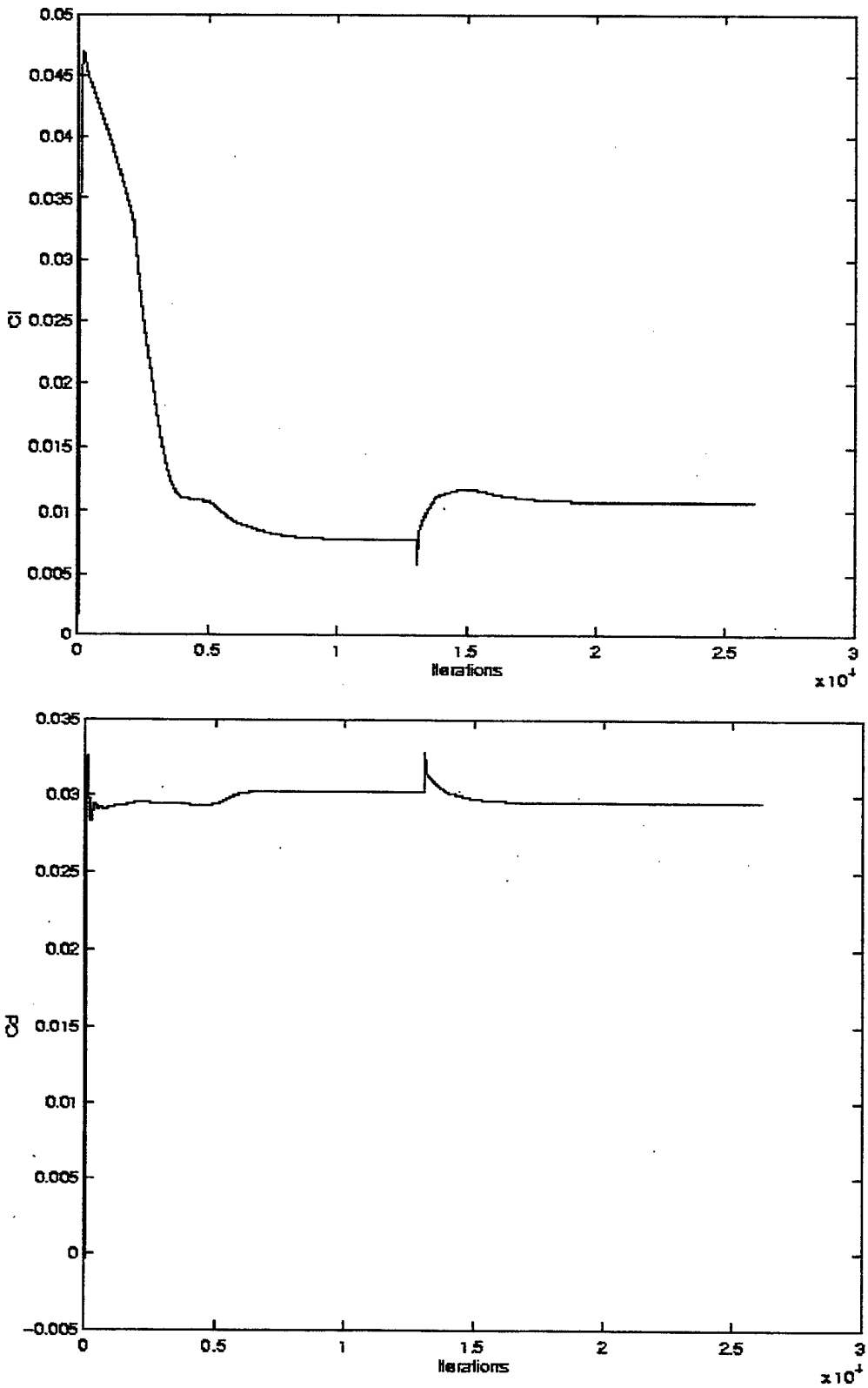

Figure C-39. Force Coefficients vs. Iterations Mach 1.2 Viscous

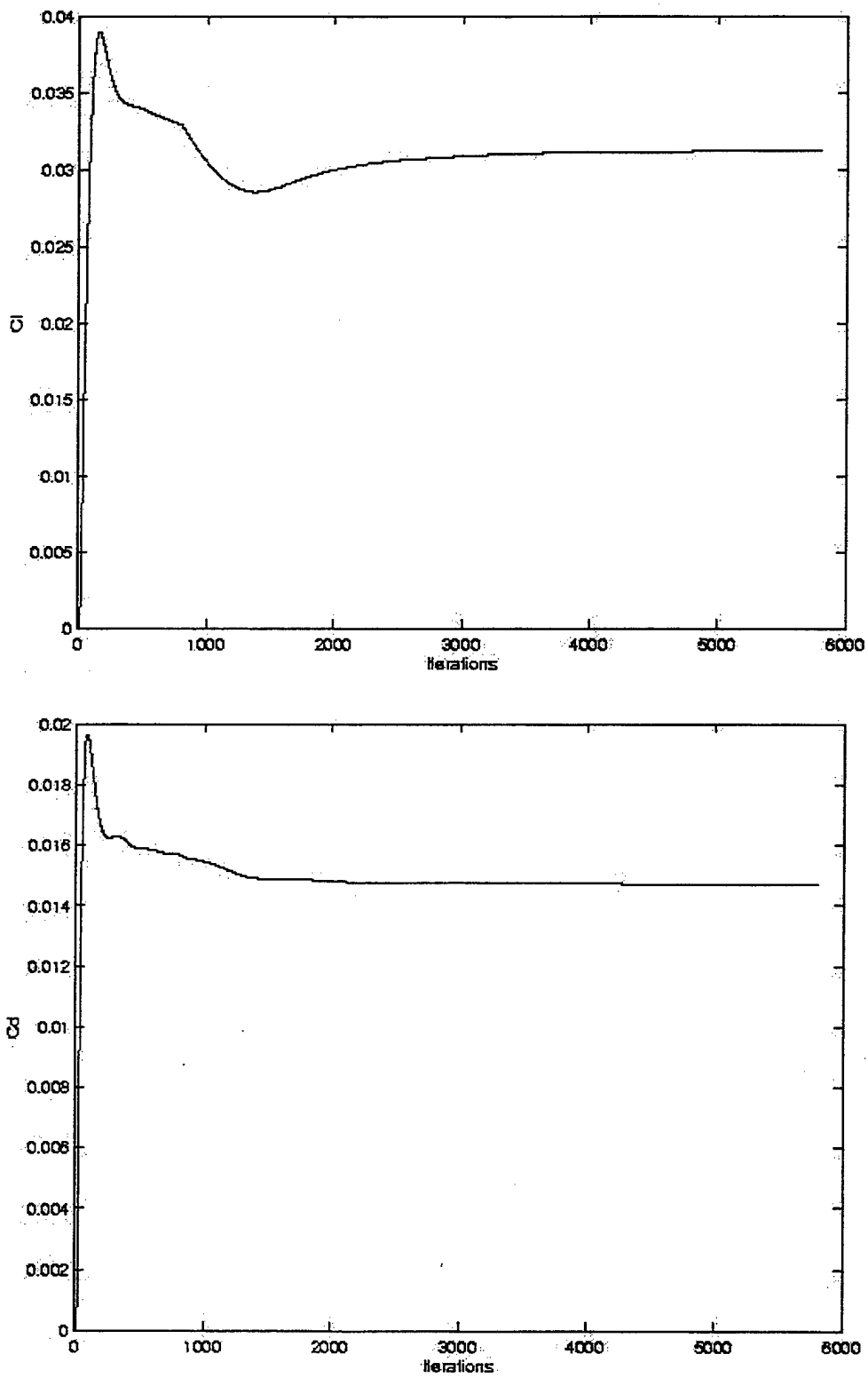

Figure C-41. Force Coefficients vs. Iterations mach 2.0 Viscous

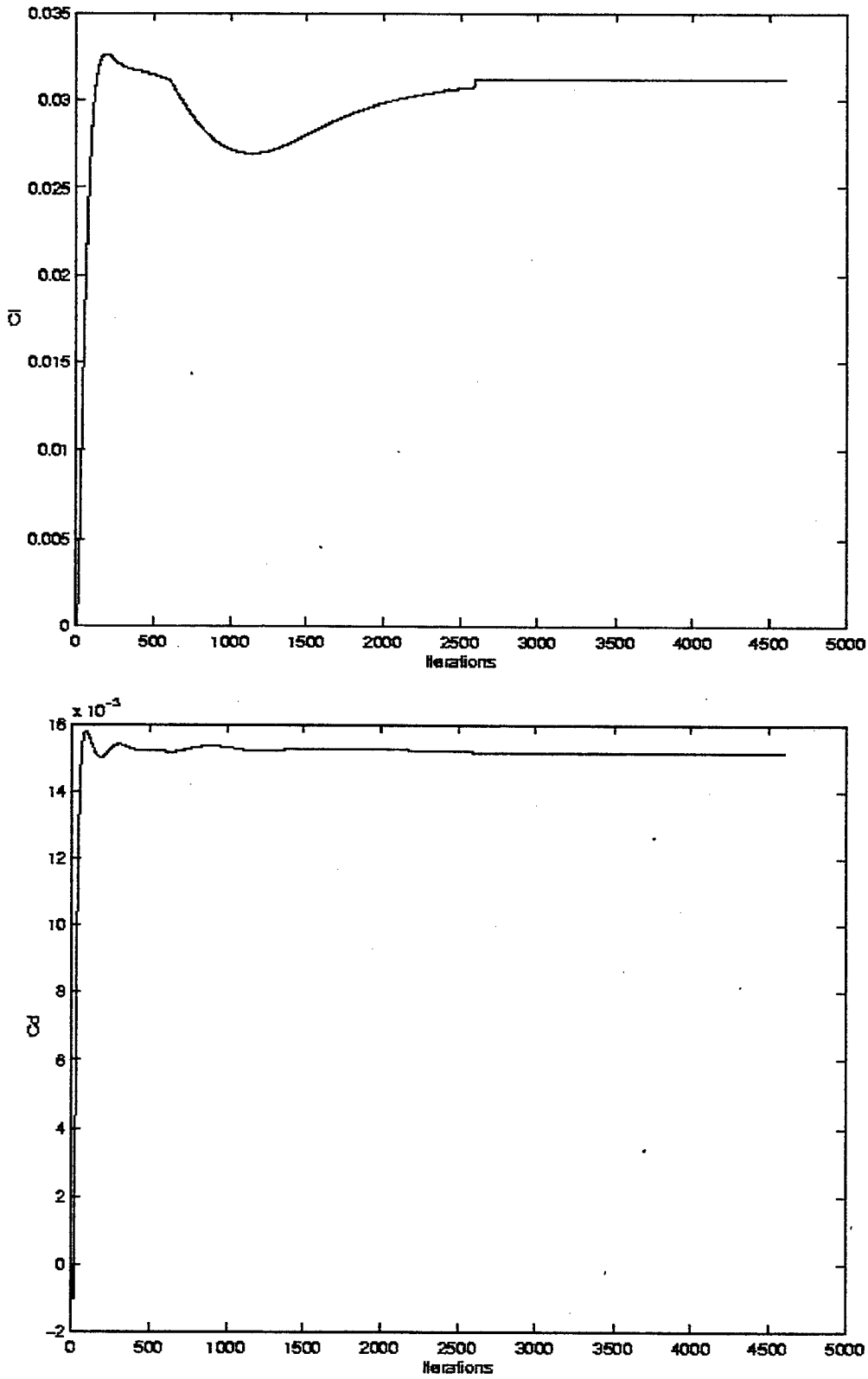

Figure C-40. Force Coefficients vs. Iterations Mach 2.0 Inviscid

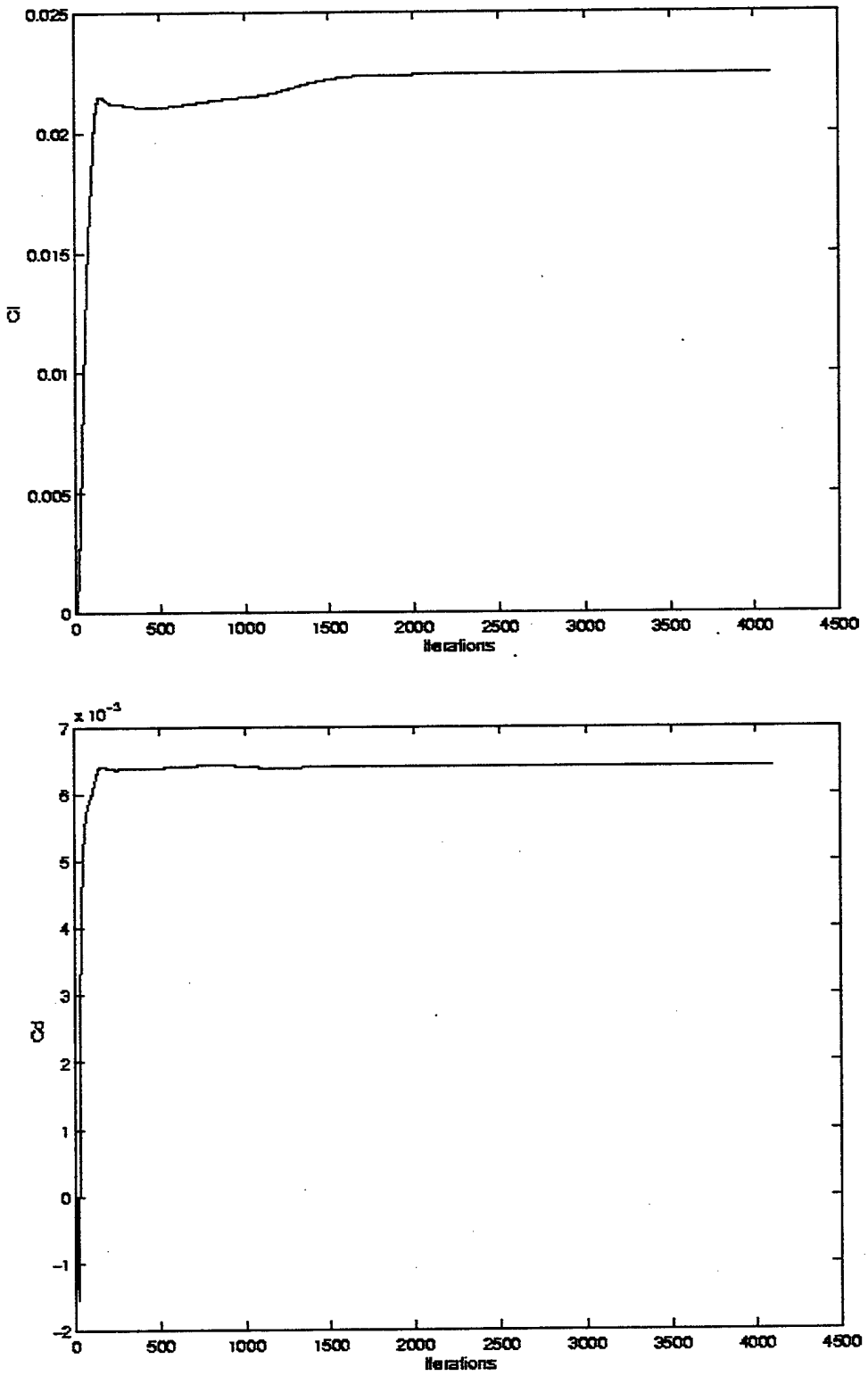

Figure C-42. Force Coefficients vs. Iterations Mach 4.0 Inviscid

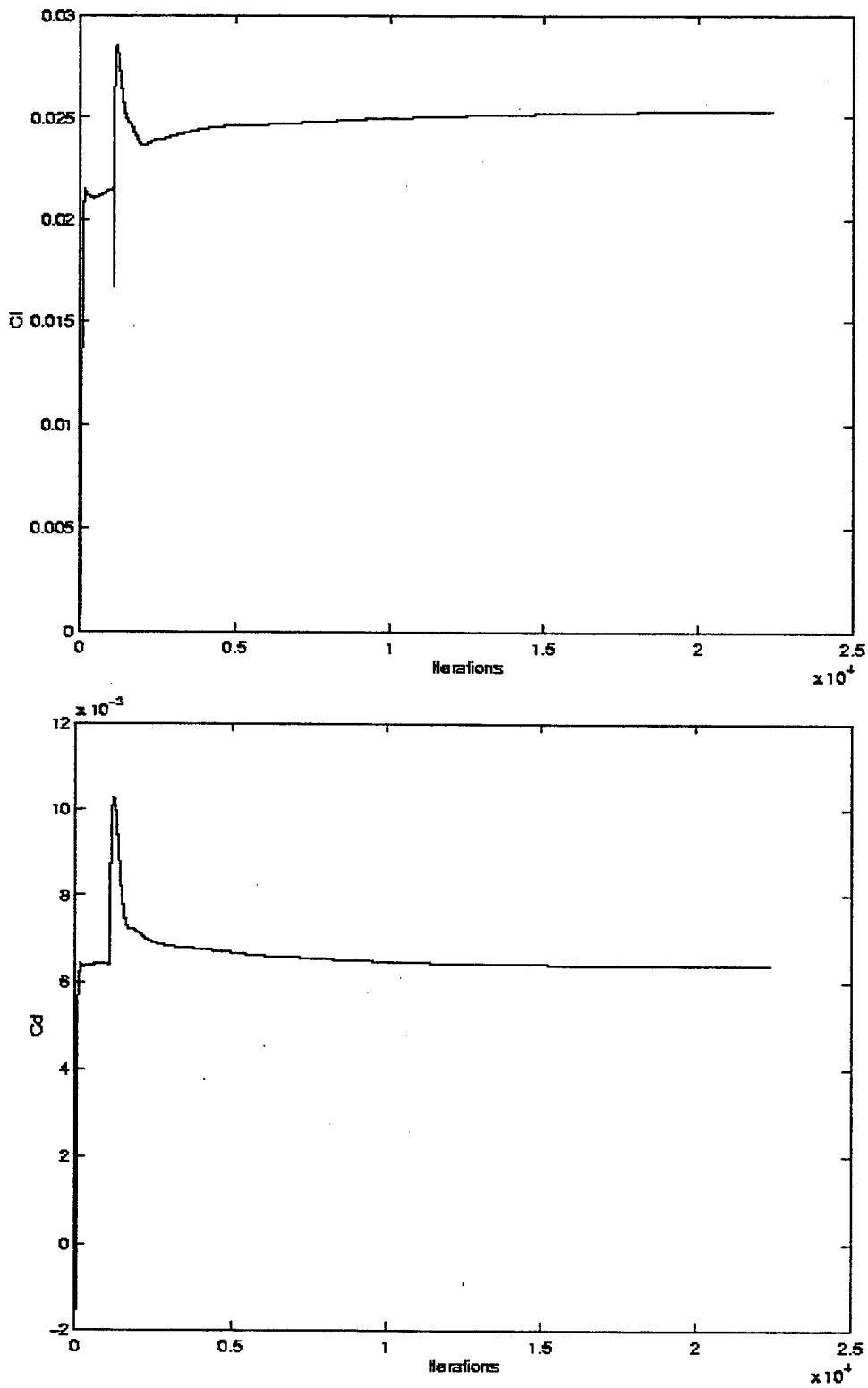

Figure C-43. Force Coefficients vs. Iterations Mach 4.0 Viscous

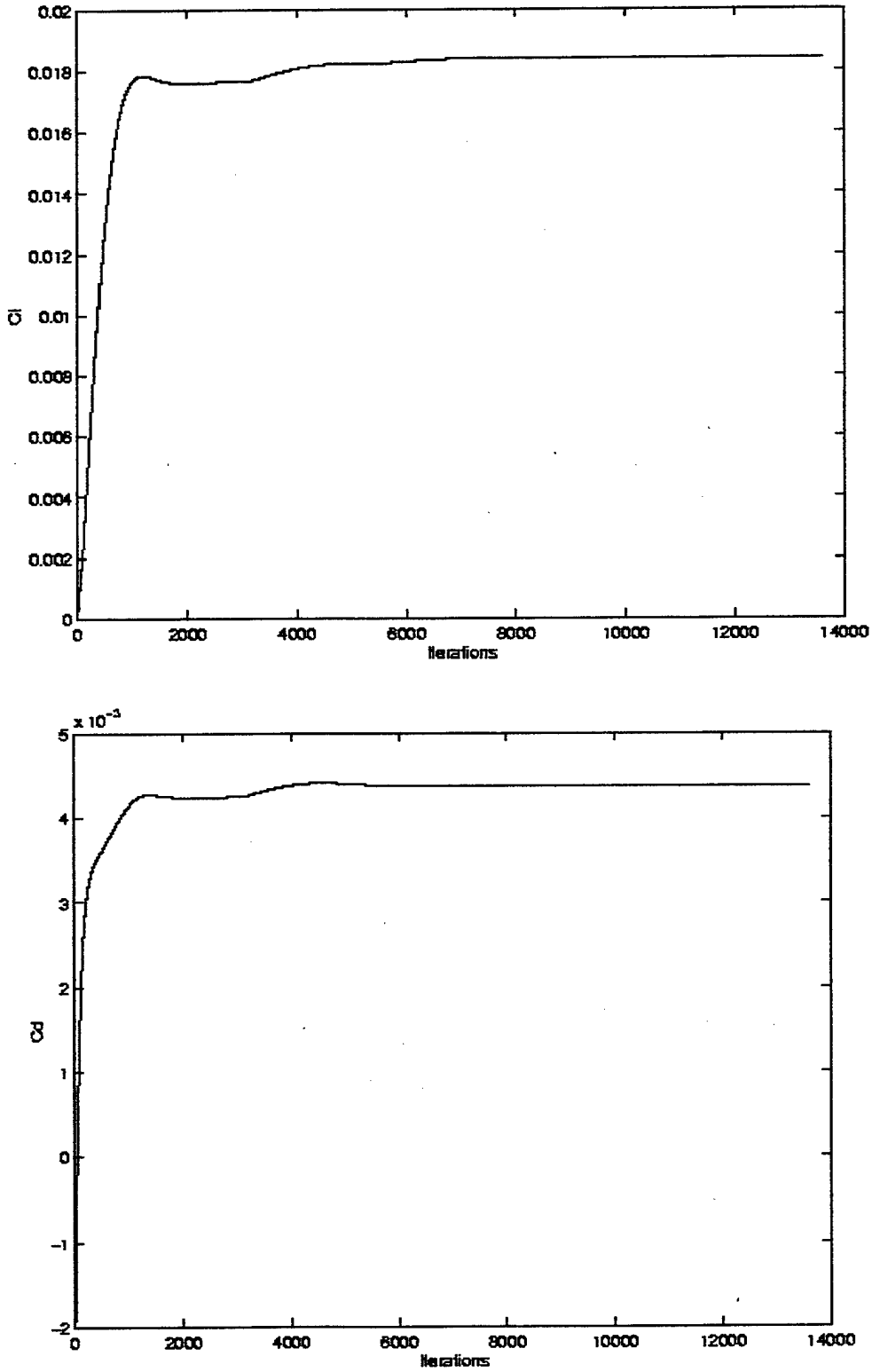

Figure C-44. Force Coefficients vs. Iterations Mach 6.0 Inviscid

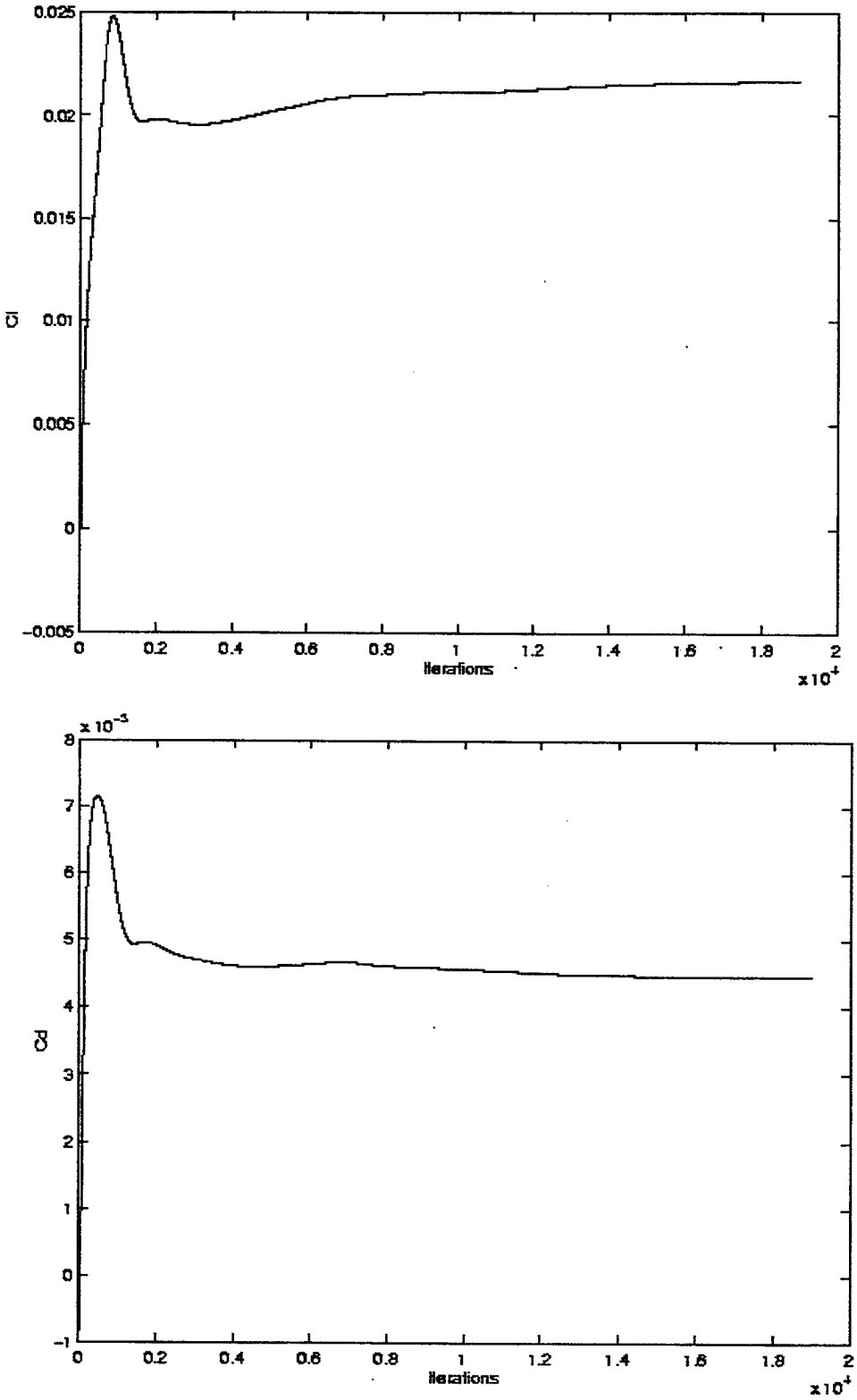

Figure C-45. Force Coefficients vs. Iterations Mach 6.0 Viscous

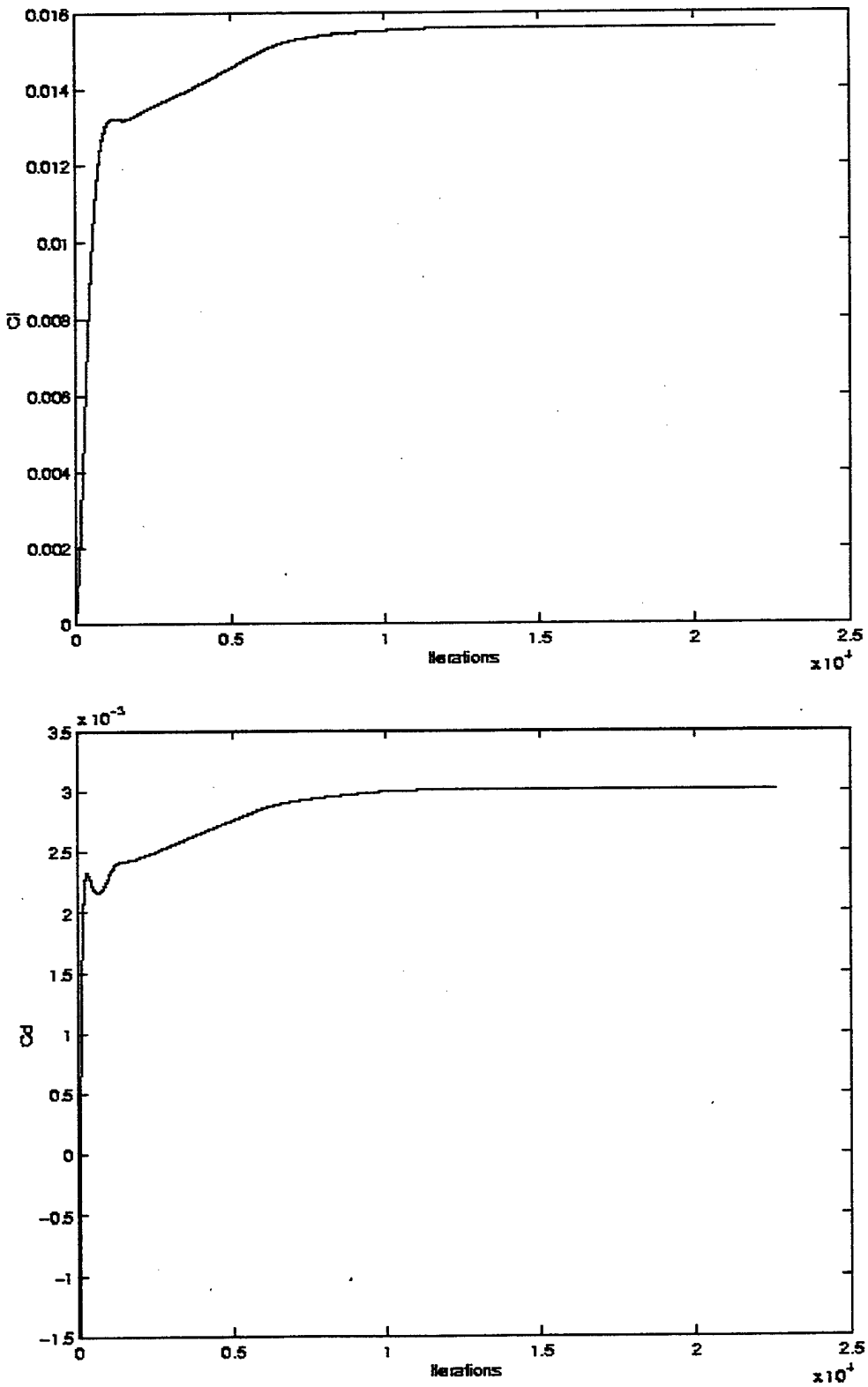

Figure C-46. Force Coefficients vs. Iterations Mach 6.0 Engine Flow-Through

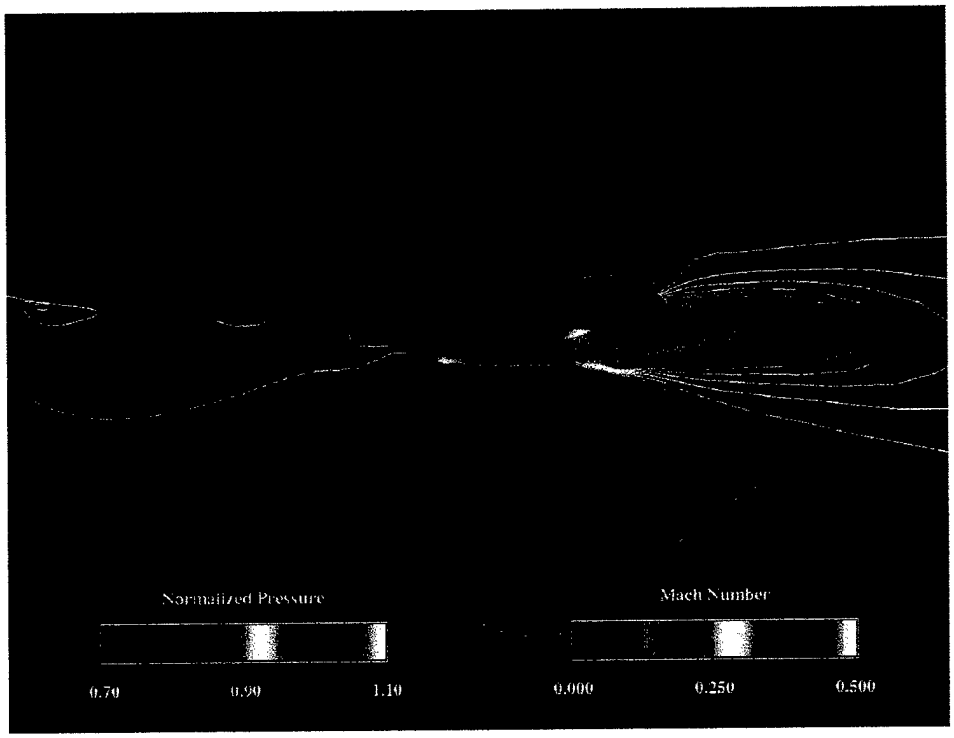

Figure C-47. Mach 0.3 Inviscid Normalized Surface Pressure and Mach Contours

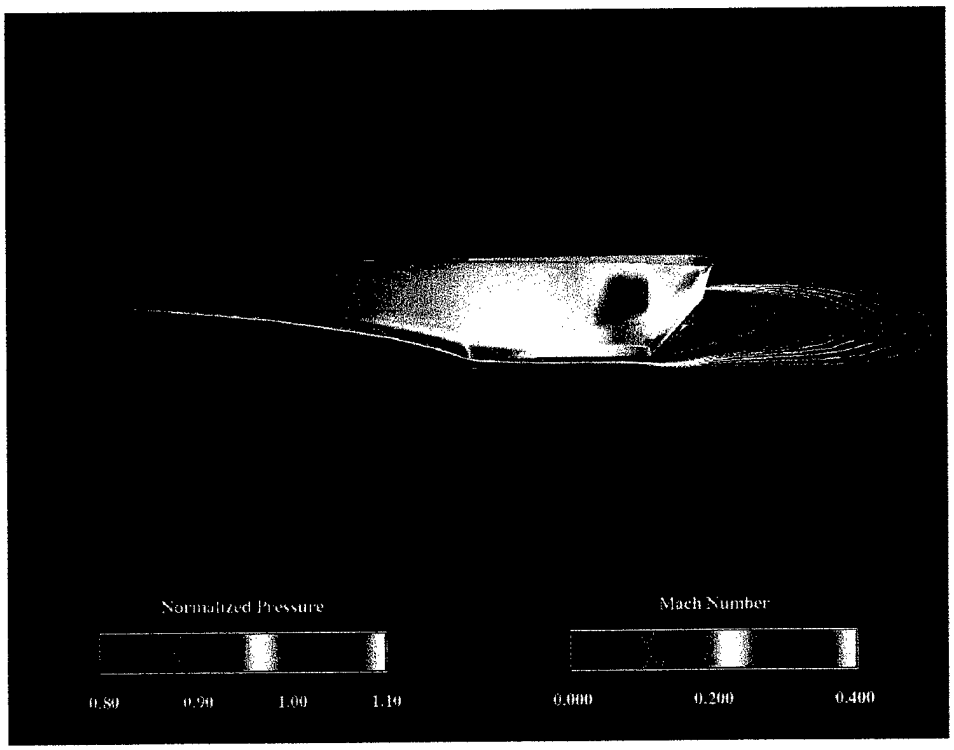

Figure C-48. Mach 0.3 Viscous Normalized Surface Pressure and Mach Contours

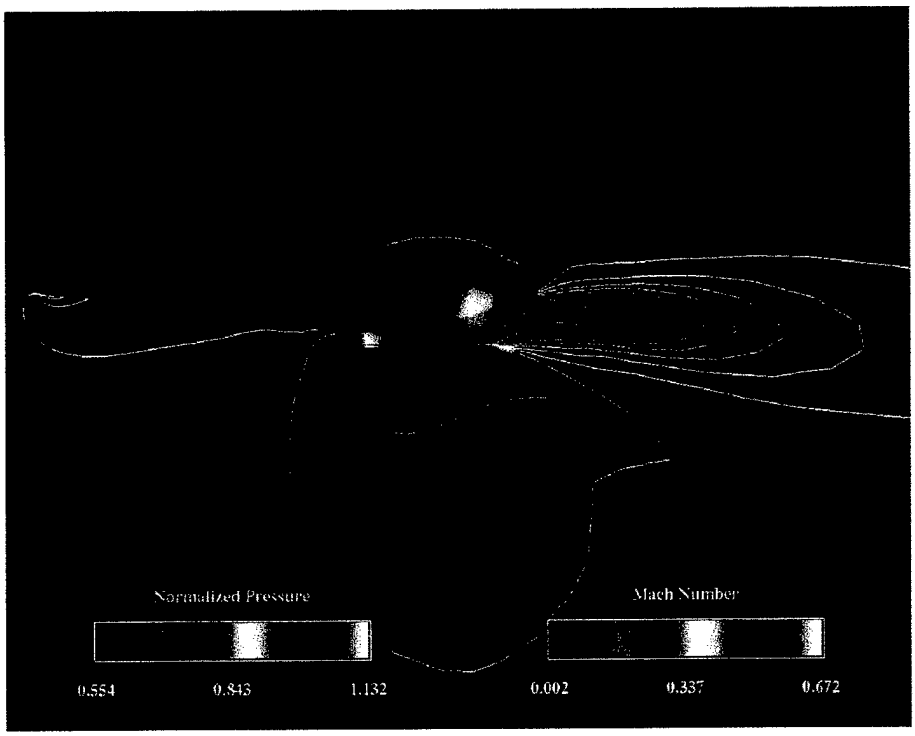

Figure C-49. Mach 0.4 Inviscid Normalized Surface Pressure and Mach Contours

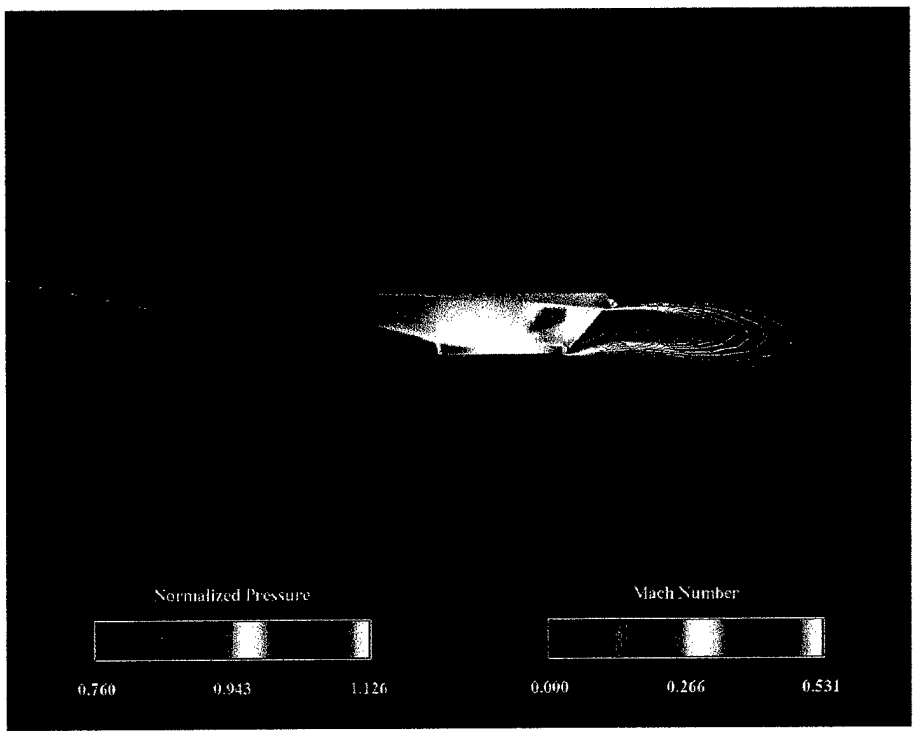

Figure C-50. Mach 0.4 Viscous Normalized Surface Pressure and Mach Contours

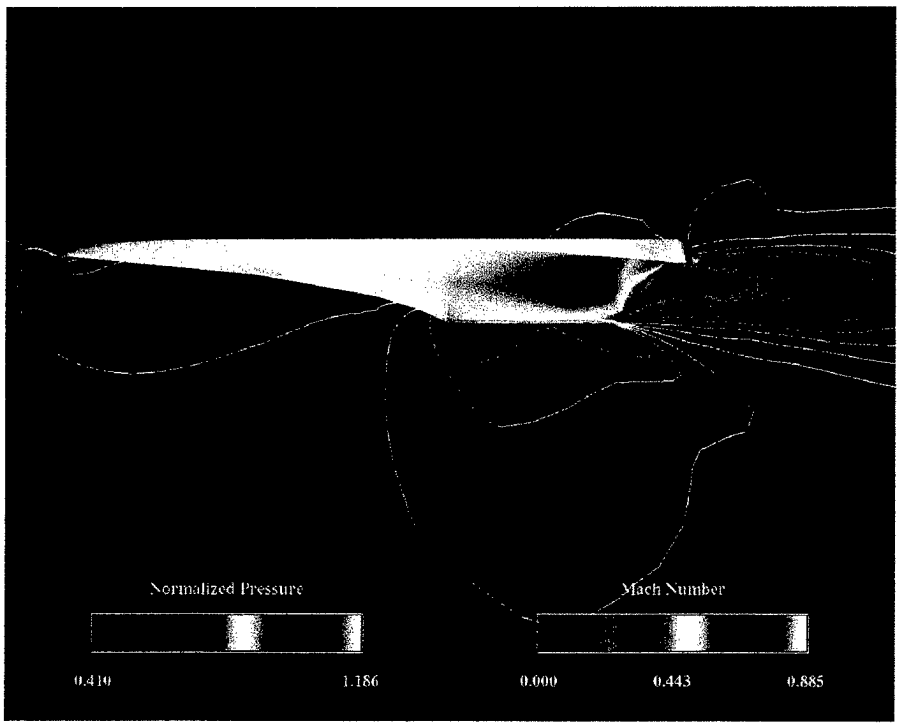

Figure C-51. Mach 0.5 Inviscid Normalized Surface Pressure and Mach Contours

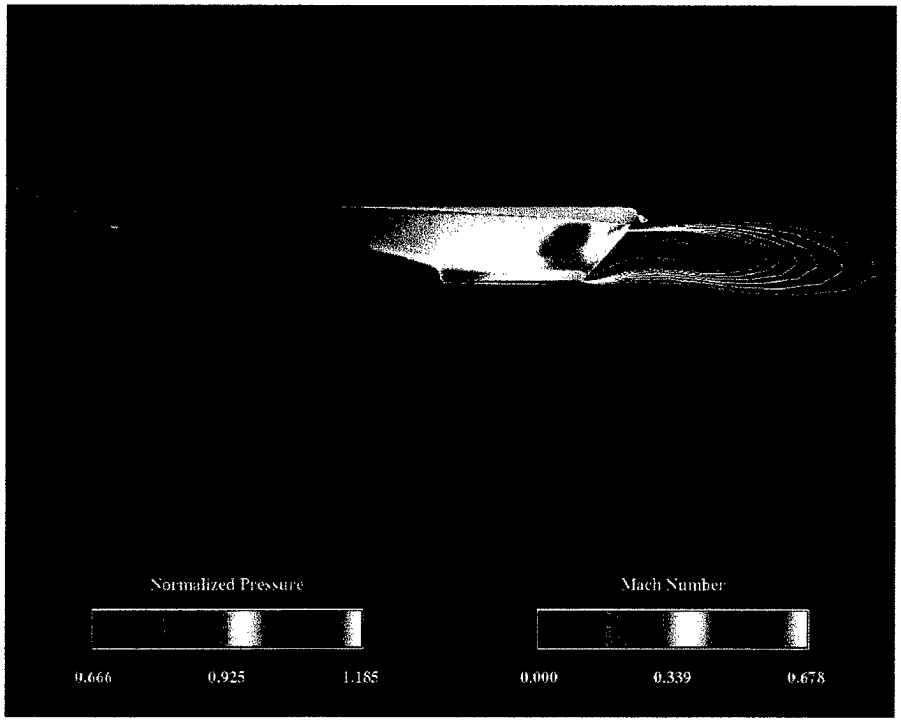

Figure C-52. Mach 0.5 Viscous Normalized Surface Pressure and Mach Contours

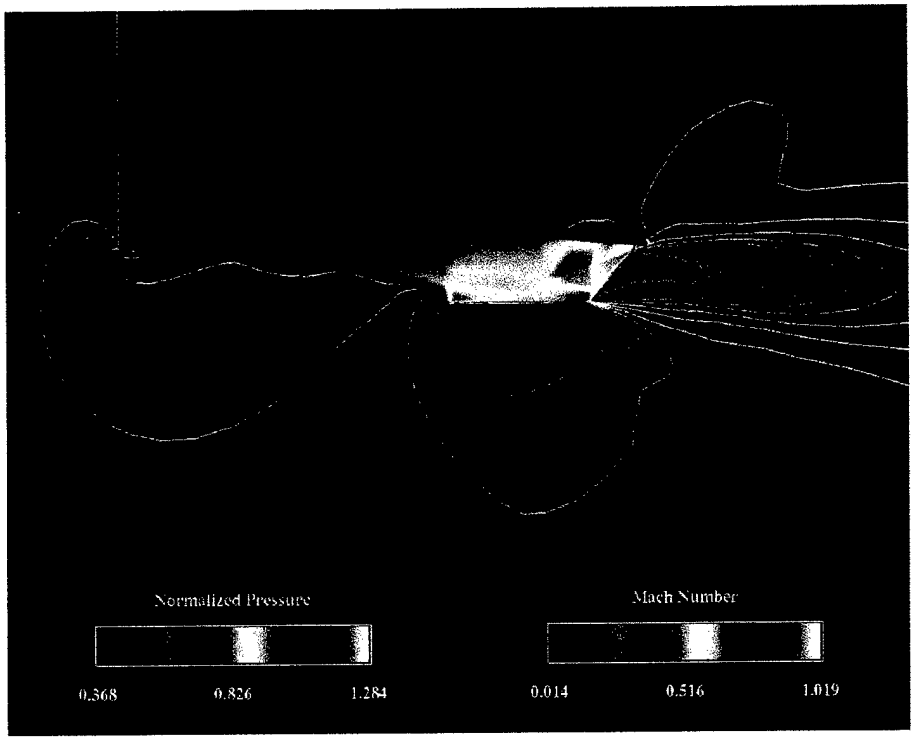

Figure C-53. Mach 0.6 Inviscid Normalized Surface Pressure and Mach Contours

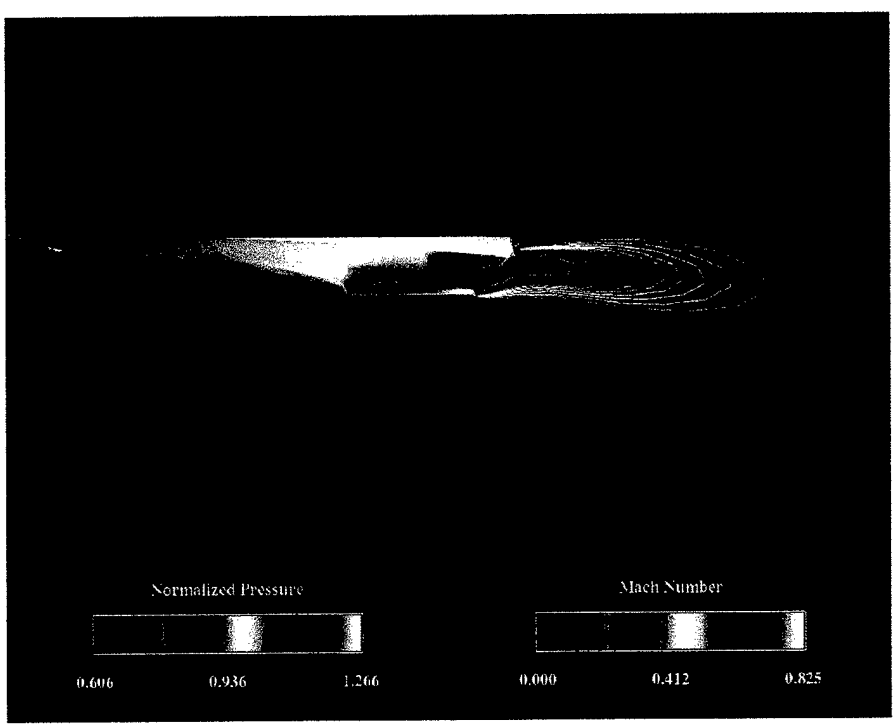

Figure C-54. Mach 0.6 Viscous Normalized Surface Pressure and Mach Contours

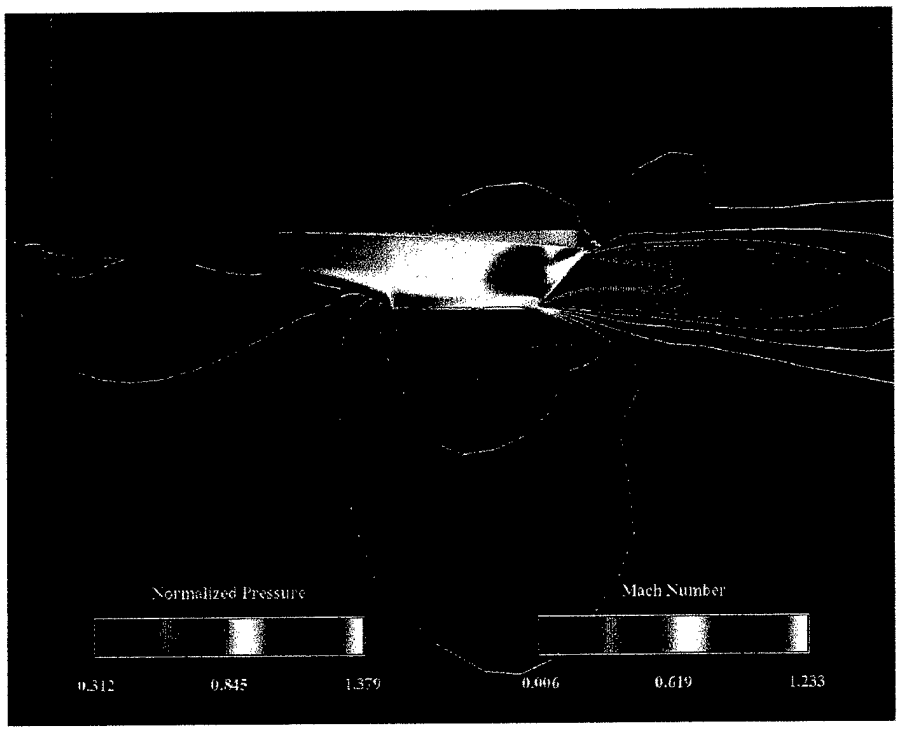

Figure C-55. Mach 0.7 Inviscid Normalized Surface Pressure and Mach Contours

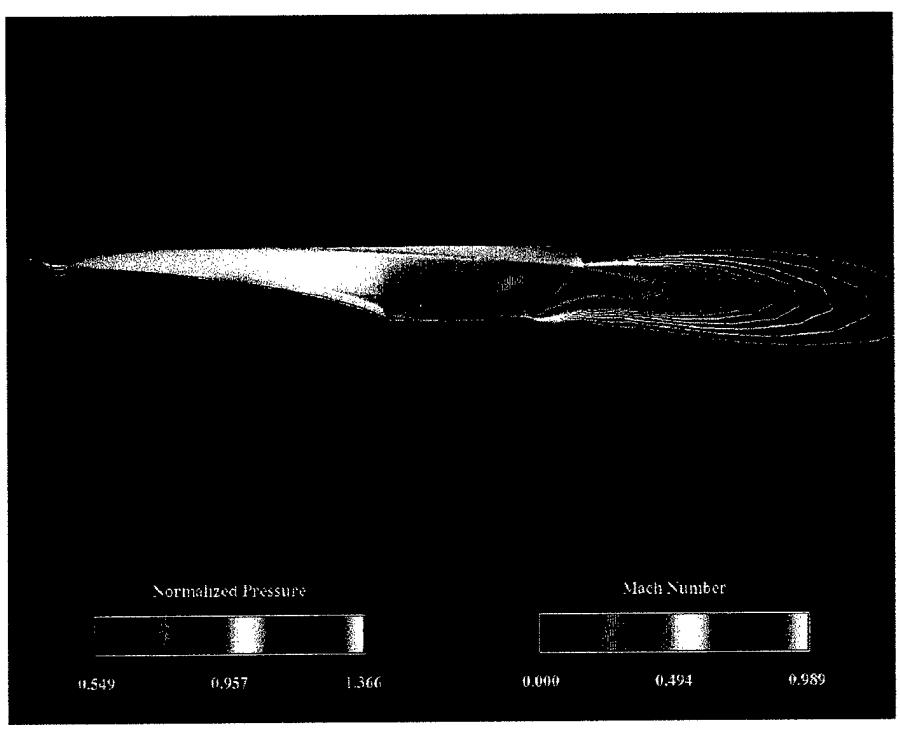

Figure C-56. Mach 0.7 Viscous Normalized Surface Pressure and Mach Contours

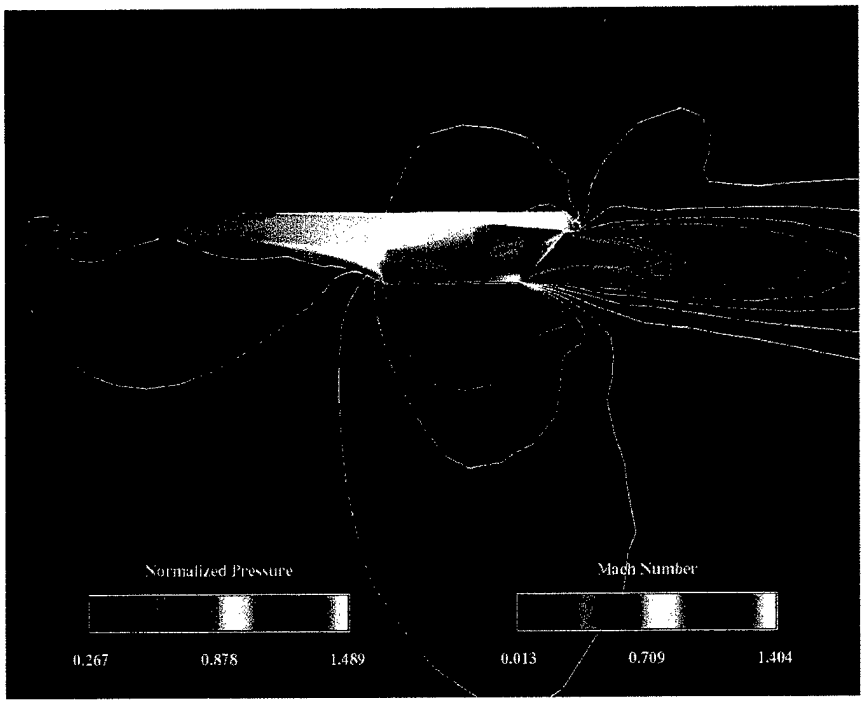

Figure C-57. Mach 0.8 Inviscid Normalized Surface Pressure and Mach Contours

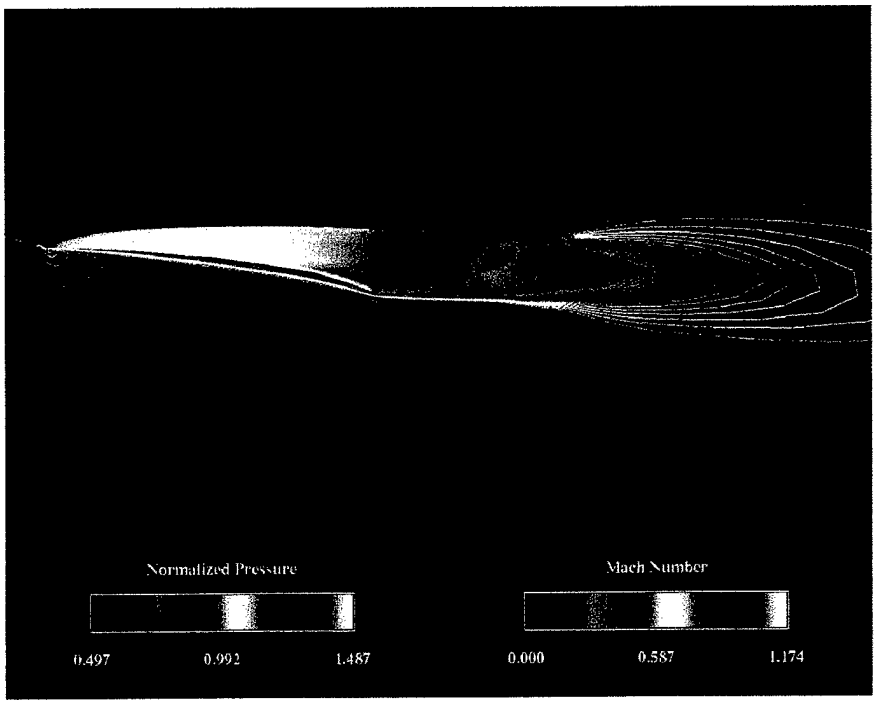

Figure C-58. Mach 0.8 Viscous Normalized Surface Pressure and Mach Contours

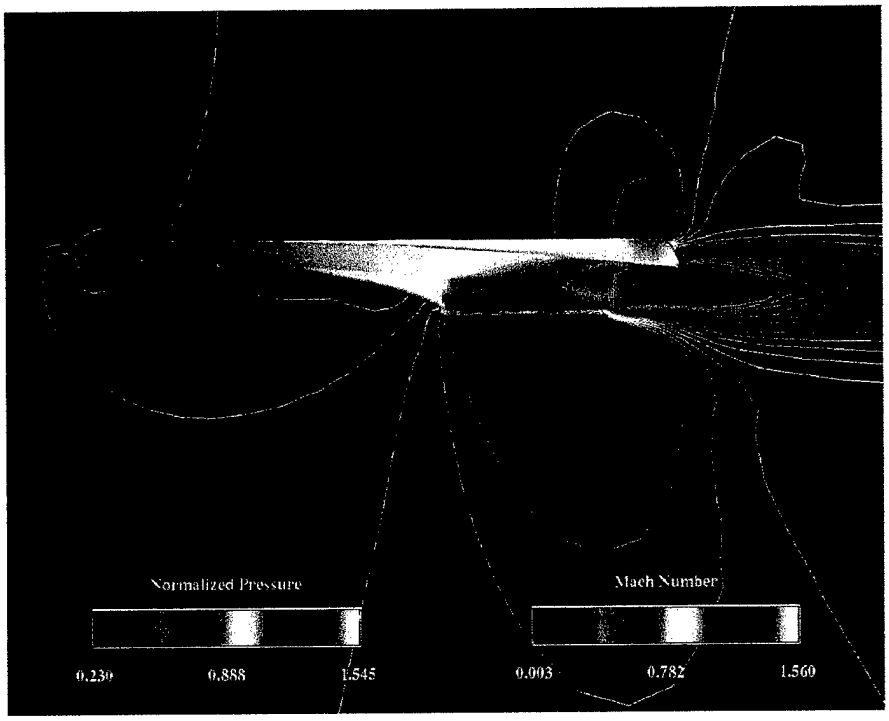

Figure C-59. Mach 0.9 Inviscid Normalized Surface Pressure and Mach Contours

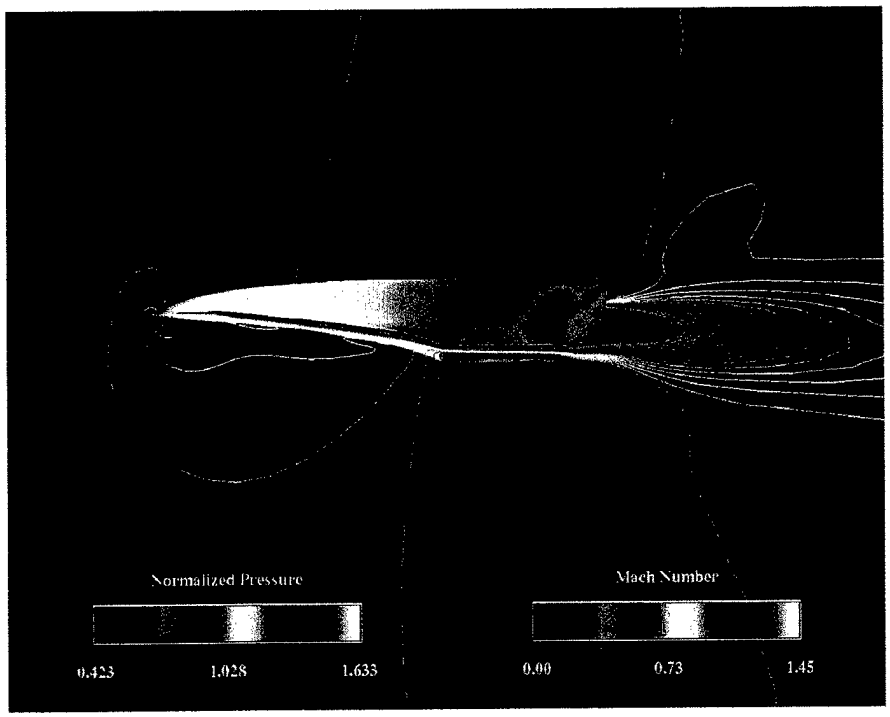

Figure C-60. Mach 0.9 Viscous Normalized Surface Pressure and Mach Contours

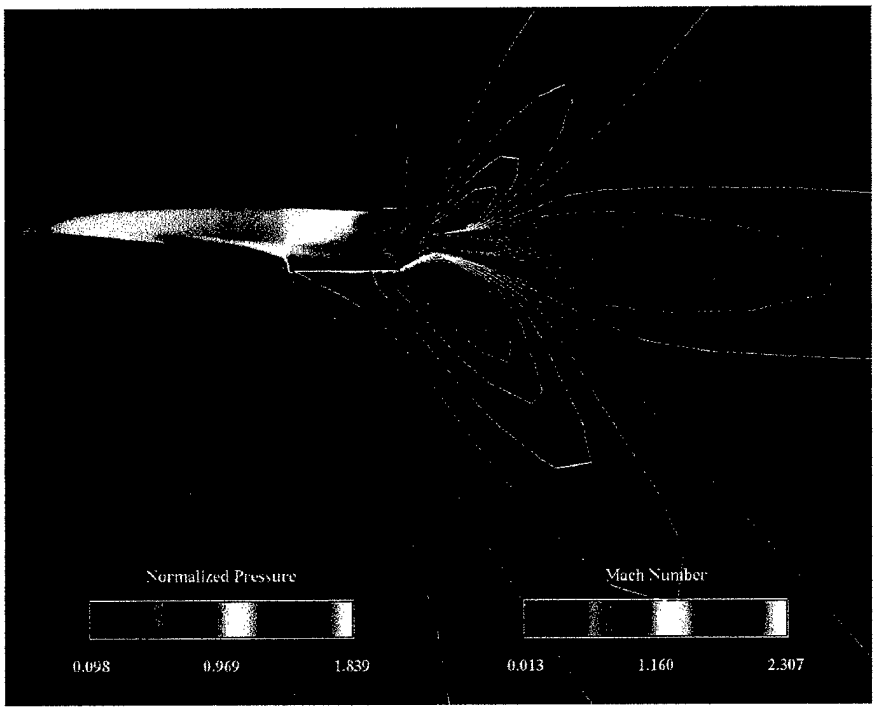

Figure C-61. Mach 1.2 Inviscid Normalized Pressure and Mach Contours

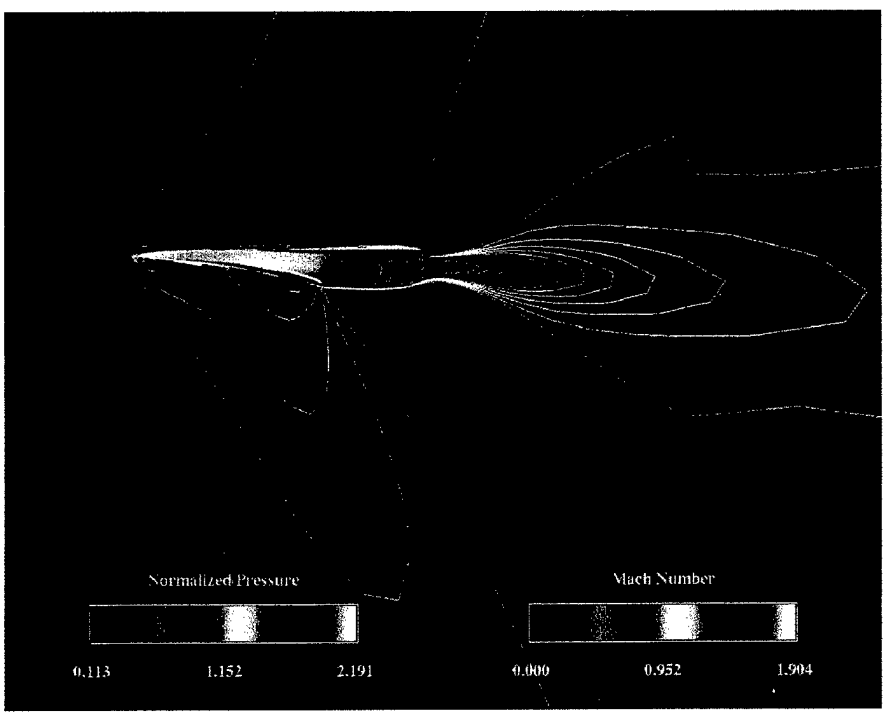

Figure C-62. Mach 1.2 Viscous Normalized Surface Pressure and Mach Contours

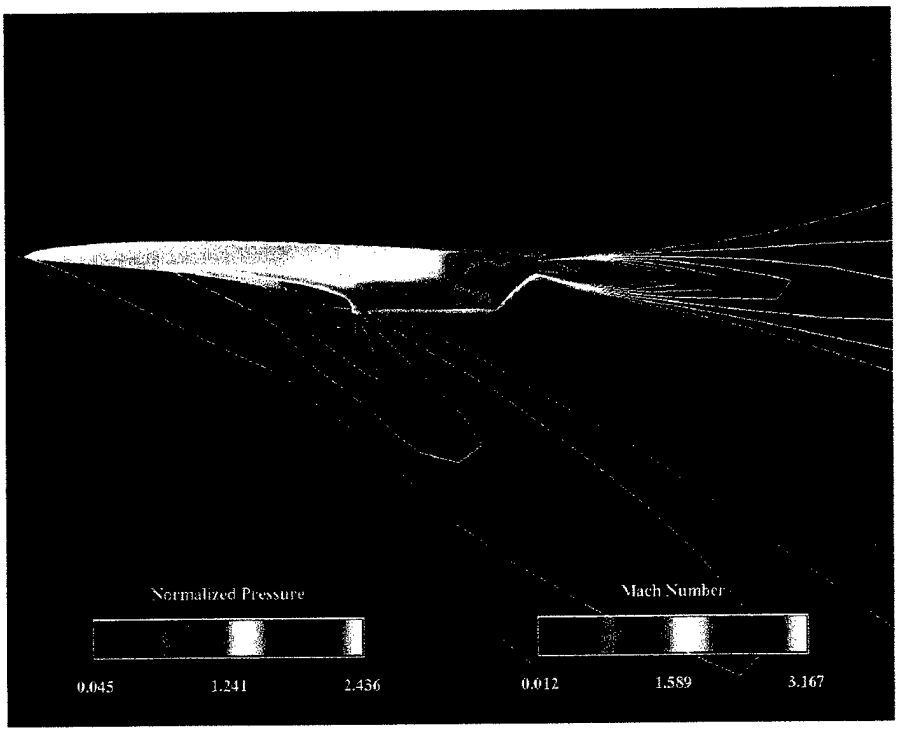

Figure C-63. Mach 2.0 Inviscid Normalized Surface Pressure and Mach Contours

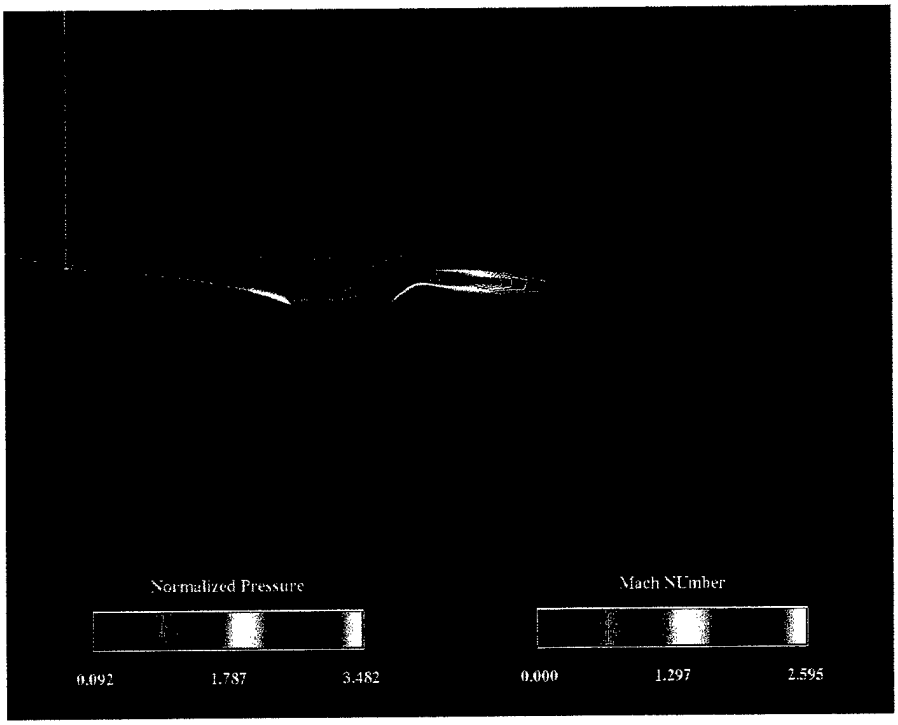

Figure C-64. Mach 2.0 Viscous Normalized Surface Pressure and Mach Contours

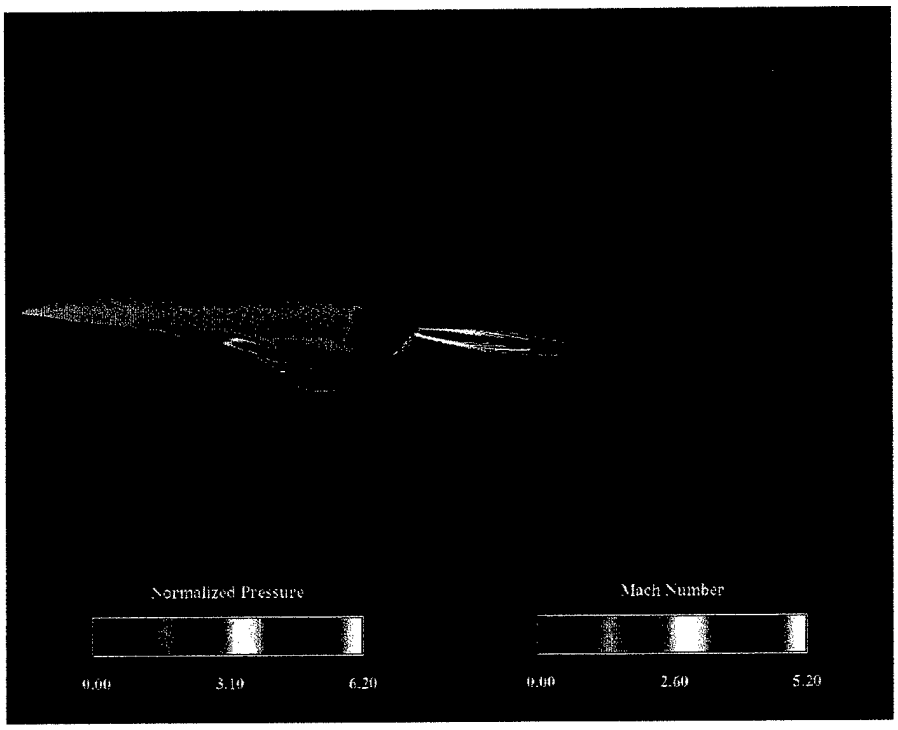

Figure C-65. Mach 4.0 Inviscid Normalized Surface Pressure and Mach Contours

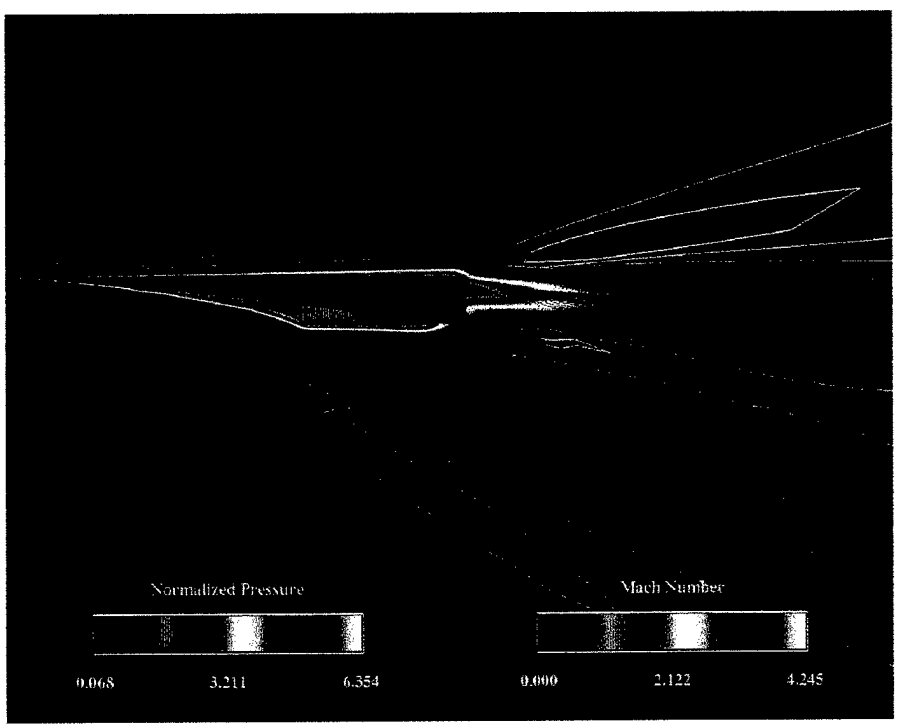

Figure C-66. Mach 4.0 Viscous Normalized Surface Pressure and Mach Contours

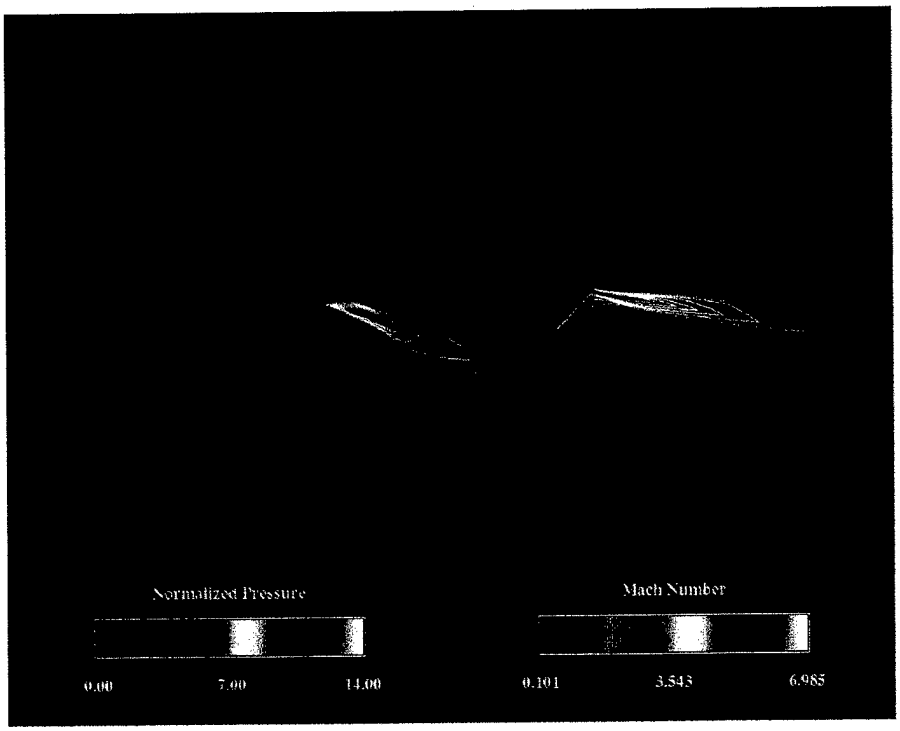

Figure C-67. Mach 6.0 Inviscid Normalized Surface Pressure and Mach Contours

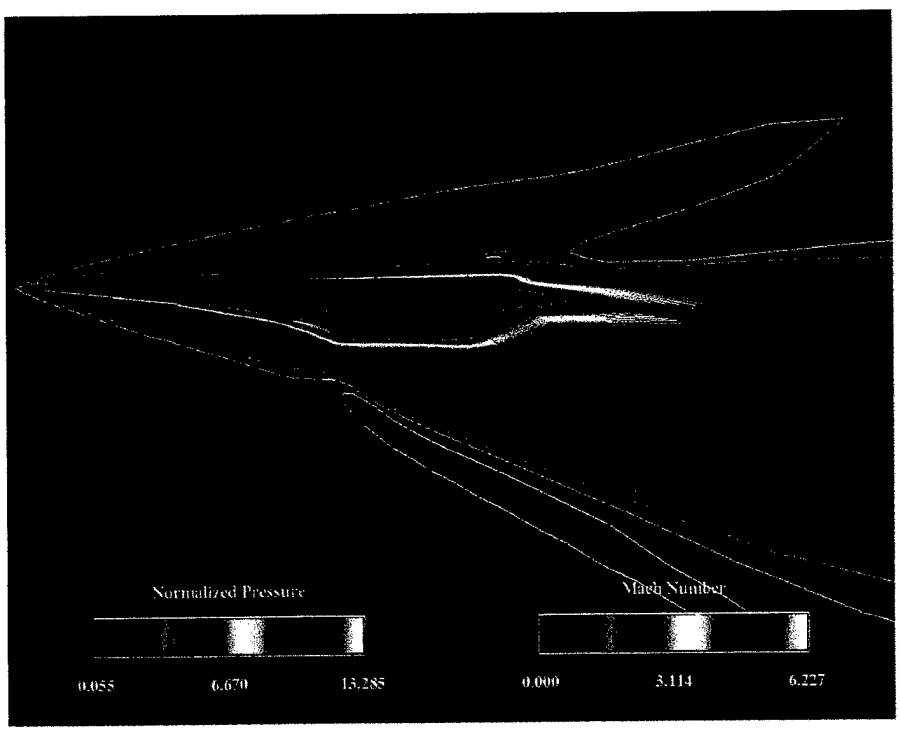

Figure C-68. Mach 6.0 Viscous Normalized Surface Pressure and Mach Contours

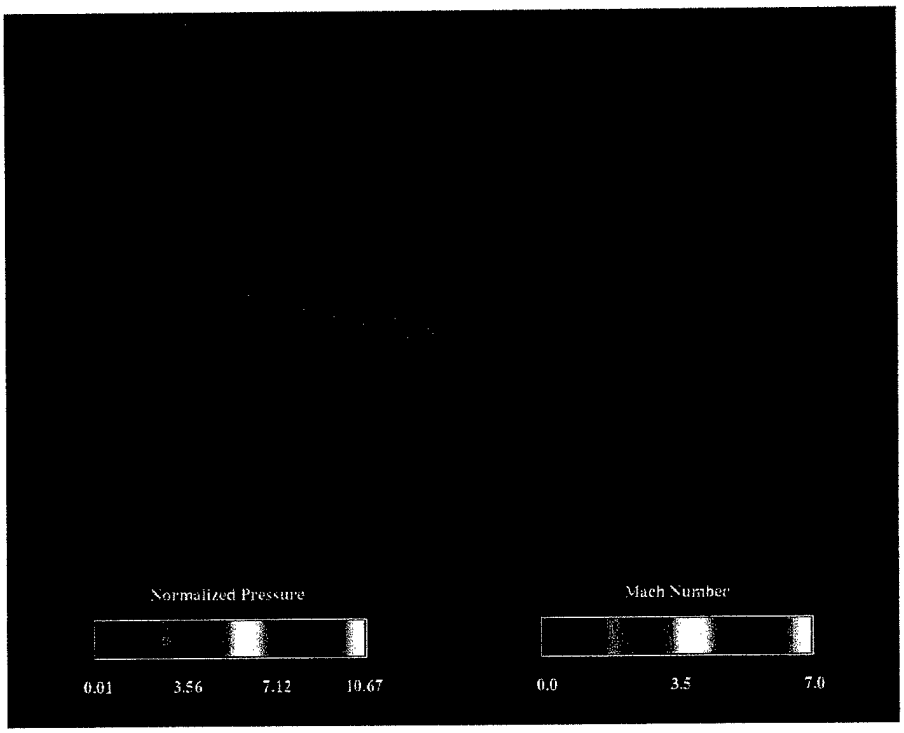

Figure C-69. Mach 6.0 Engine Flow-Through Normalized Surface Pressure and Mach Contours

THIS PAGE INTENTIONALLY LEFT BLANK

INITIAL DISTRIBUTION LIST

1. Defense Technical Information Center 2
   8725 John J. Kingman Rd., Suite 0944
   Ft. Belvoir, VA 22060-6218

2. Dudley Knox Library 2
   Naval Postgraduate School
   411 Dyer Rd.
   Monterey, CA 93943-5101

3. Prof. Conrad F. Newberry, AA/Ne 3
   Department of Aeronautics and Astronautics
   Naval Postgraduate School
   Monterey, CA 93943-5000

4. Assoc. Prof. Garth V. Hobson , AA/Hg 3
   Department of Aeronautics and Astronautics
   Naval Postgraduate School
   Monterey, CA 93943-5000

5. Prof. Gerald H. Lindsey, AA/Li 1
   Chairman, Department of Aeronautics and Astronautics
   Naval Postgraduate School
   Monterey, CA 93943-5000

6. Mr. Robert Pap 1
   Accurate Automation Corporation
   7001 Shallowford Rd.
   Chattanooga, TN 37421

7. Dr. Mark J. Lewis 1
   Professor
   Director, Center for Hypersonic Education and Research
   Department of Aerospace Engineering
   University of Maryland
   College Park, MD 20742-3015

8. Mr. Jeffrey V. Bowles 1
   Aerospace Engineer
   National Aerospace and Space Administration
   Ames Research Center
   MS 237-11
   Moffett Field, CA 94305

9. Dr. Isaiah M. Blankson 1
National Aerospace and Space Administration
Lewis Research Center
MS 5-9, ORG-5000
21000 Brookpark Road
Cleveland, OH 44135

10. Dr. Pieter G. Buning 1
Configuration Aerodynamics Branch
Mail Stop 499
NASA Langley Research Center
Hampton, VA 23681-2199

11. LT Raymond E. O'Hare 1
Department of Aeronautics and Astronautics
Naval Postgraduate School
Monterey, CA 93943-5000

12. LCDR Ellen Coyne 1
13404 Stowaway Dr.
Solomons, MD 20688